Computational Methods for High-Density Surface EMG: Decomposition, Localization, and Modelling

Lundsberg, Jonathan

2025

Computational Methods for High-Density Surface EMG Analysis: Decomposition, Localization, and Modelling

Jonathan Lundsberg

LUND
UNIVERSITY

DOCTORAL DISSERTATION

by due permission of the Faculty of Engineering, Lund University, Sweden.
To be defended in E:A, Ole Römers väg 3, Lund.
June 13th, 2025 at 09:15

Faculty opponent
Associate Professor Alberto Botter

DOKUMENTDATABLAD enl SIS 61 41 21

Organization LUND UNIVERSITY Department of Biomedical Engineering P.O. Box 118 SE-221 00, Lund, Sweden	**Document name** DOCTORAL DISSERTATION **Date of issue** 2025-05-12 **Sponsoring organization** The Promobilia Foundation
Author Jonathan Lundsberg	

Title
Computational Methods for High-Density Surface EMG Analysis: Decomposition, Localization, and Modelling

Abstract
The ability to generate and control movement is essential for human interactions and overall well-being. Neuromuscular impairment caused by neurological injuries and diseases, such as stroke or limb amputation, severely limits the ability of affected individuals to interact with the surrounding environment, necessitating advanced strategies for rehabilitation and restoration of motor function. Voluntary muscle contractions are initiated by motor neurons that transmit electrical impulses, or action potentials, which propagate along nerves and throughout muscle fibres. A single motor neuron and its associated muscle fibres form a motor unit, which creates a direct link between the nervous system output and electrical signals generated by muscles. High-density surface electromyography (HDsEMG) is a powerful non-invasive technique for analysing neuromuscular function by capturing the electrical activity of motor unit action potentials. However, extracting meaningful information from HDsEMG recordings remains a significant challenge due to the complex spatial and temporal overlap of motor unit activity, particularly in regions with high muscle density, such as the forearm.
This dissertation consists of an introduction, background, and four papers presenting novel methods and algorithms for analysing HDsEMG data. Paper I introduces a new algorithm for motor unit decomposition, combining Fast Independent Component Analysis with an iterative peel-off scheme based on spike-triggered averaging and Principal Component Compression. Paper II presents a method for localizing motor unit action potentials, identified with the decomposition method in Paper I, estimating the centre of electrical activity using a surface fitting approach and an analytical volume conductor model. Paper III shifts the focus from motor units, and the reliance on decomposition, to localization of individual time-domain peaks directly in the HDsEMG data, and introduces a new technique for constructing a three-dimensional model of muscle activity. In this model, individual muscles are represented as distinct volumes, which are subsequently used to classify additional HDsEMG signals into specific muscle activations. Paper IV extends this approach, applying the volume-based muscle representations to gesture classification and evaluates their generalizability across participants and for novel gestures beyond the original model.

Key words
EMG, biosignal processing, decomposition, motor unit, localization, muscle modelling, gesture recognition, myoelectric control, rehabilitation assessment

Classification system and/or index terms (if any)

Supplementary bibliographical information ISRN: LUTEDX/TEEM-1143-SE, Report No. 4/25		**Language** English
ISSN and key title:		**ISBN** 978-91-8104-553-6 (print) 978-91-8104-554-3 (electronic)
Recipient's notes	**Number of pages** 169	**Price**
	Security classification	

To my family and friends

What's the point of anything exciting,
if you can't share it?

Public defence
June 13th, 2025, 09:15 in E:A, E-building, LTH, Ole Römers väg 3, 22363 Lund, Sweden

Supervisors
Associate Professor Christian Antfolk
Associate Professor Nebojša Malešević
Department of Biomedical Engineering, Faculty of Engineering, Lund University, Sweden

Professor Anders Björkman
Institute of Clinical Sciences, Sahlgrenska Academy, University of Gothenburg, Sweden
Department of Hand Surgery, Sahlgrenska University Hospital, Mölndal, Sweden

Faculty opponent
Associate Professor Alberto Botter
Department of Electronics and Telecommunications, Politecnico di Torino, Italy

Examination board
Associate Professor Jakob Lund Dideriksen
Department of Health Science and Technology, The Faculty of Medicine, Aalborg University, Denmark

Associate Professor Elaine Åstrand
Division of Intelligent Future Technologies, School of Innovation, Design and Engineering, Mälardalen University, Sweden

Associate Professor Daniel Benoit
Department of Health Sciences, Faculty of Medicine, Lund University, Sweden

Deputy member: Associate Professor Kirsten Rassmus-Gröhn
Department of Design Sciences, Faculty of Engineering, Lund University, Sweden

Chairman
Associate Professor Ingrid Svensson
Department of Biomedical Engineering, Faculty of Engineering, Lund University, Sweden

Cover illustration
A stylized rendition of muscle fibres.

ISBN: 978-91-8104-553-6 (printed version)
ISBN: 978-91-8104-554-3 (electronic version)
Report No. 4/25
ISRN: LUTEDX/TEEM-1143-SE
Printed by Tryckeriet, E-building, Faculty of Engineering, Lund University, Lund, Sweden

Contents

Populärvetenskaplig sammanfattning

Rörelse är en grundläggande del av livet och kritiskt för vårt välmående. Vi använder våra muskler för att kommunicera med varandra och interagera med världen omkring oss. Men vad gör vi när förmågan att styra våra muskler försvagas eller går förlorad? Skador och sjukdomar i nervsystemet, liksom en amputation eller stroke, har ofta en enorm påverkan på en individs rörelseförmåga och därmed deras kapacitet att uttrycka sig. I grunden så styrs våra muskler med hjälp av elektriska impulser från hjärnan och ryggmärgen som leds hela vägen ut till varje individuell muskelfiber. Målet med denna avhandling är att undersöka dessa nervimpulser, tolka dem, och utveckla nya möjligheter för att återställa eller ersätta förlorad muskelfunktion. Men vi behöver inte stanna där; kan vi även förbättra eller till och med utöka vår naturliga förmåga att interagera med omvärlden? Med dessa mål i hänseende krävs först en bättre inblick i hur nervsystemet styr våra muskler, samt vilka metoder som finns för att mäta och bearbeta de nervsignaler som kroppen genererar.

Elektriska impulser som sprids genom nerv- och muskelfibrer består av snabba kortvariga flöden av olika joner med elektrisk laddning, såsom natrium, kalium, och kalcium. När en nervimpuls når en muskel så sprids den genom ett antal muskelfibrer samtidigt, vilket får dem att dra ihop sig. En nervcell, dess utskott (axon), och de anslutna muskelfibrerna utgör en enstaka motorenhet, vilket kan sägas vara den minsta byggstenen i en muskelkontraktion. Varje motorenhet genererar ett synkroniserat flöde av laddade joner, vilket skapar en elektrisk signal som är så pass stark att den kan mätas utanför kroppen – tekniken för att mäta en sådan signal kallas för elektromyografi (EMG).

EMG möjliggör mätningar av nervsystemets styrsignaler när de uppstår i muskelfibrerna, vilket har en mängd applikationsområden, inom exempelvis rehabilitering av strokepatienter, styrning av proteser för amputerade, och utveckling av nya typer av

människa-maskininteraktioner. Med dessa områden i åtanke, utforskar denna avhandling hur EMG kan tillämpas för att återställa, ersätta, och förbättra våra muskelfunktioner. Själva mätningen av EMG är principiellt väldigt enkel. Små metallplattor, kallade elektroder, placeras på huden nära en muskel där de känner av de elektriska variationer som uppstår i muskelfibrerna. Elektroderna leder de elektriska signalerna till ett mätsystem som omvandlar dem till ett digitalt format. Den stora svårigheten med EMG ligger i att tolka signalerna. Kroppen har hundratals muskler som i sin tur består av tusentals muskelfibrer som alla kan ta emot många nervimpulser per sekund. Av särskilt intresse är våra händer, vars exceptionella finmotorik särskiljer människan från andra arter. Händerna styrs till stor del av muskler i underarmen, som med långa senor fäster sig vid handleden och fingrarna. Underarmen rymmer ett tjugotal kompakt ordnade muskler vilket gör det svårt att urskilja dem från varandra vid en EMG-mätning. Hur översätter vi då dessa EMG-signaler till information som är användbar för en fysioterapeut eller till en handprotes?

Arbetet i denna avhandling handlar om att utveckla metoder för att just *dekomponera*, *lokalisera*, och *modellera* de signaler som utgör EMG, med fokus på musklerna i underarmen och handen. Att dekomponera EMG innebär att bryta ner den sammansatta signalen i sina beståndsdelar. Mer specifikt används olika algoritmer för signalseparation som identifierar impulser från enskilda motorenheter. Intuitivt gäller samma princip då vi med vår hörsel kan urskilja och fokusera på en enskild röst i ett bullrigt rum där många pratar samtidigt. Avhandlingen presenterar den underliggande teorin för signalseparation, i kombination med nya algoritmer särskilt anpassade för muskelsignaler. När EMG mäts på huden, så behövs även metoder för att ta reda på exakt var under huden en viss signal kommer ifrån. Detta kallas lokalisering, vilket återigen kan liknas med vår hörsel, då vi ofta kan uppskatta både riktning och avstånd till ett visst ljud. På liknande sätt går det att uppskatta var en impuls från en motorenhet har sitt ursprung; en metod för detta vidareutvecklas och presenteras i denna avhandling. Slutligen, för att kunna urskilja och visualisera aktivitet från ett flertal muskler, så behövs en modell som beskriver musklernas placering. Avhandlingen presenterar en ny metod för kartläggning av muskelaktivitet baserat på EMG i en tredimensionell modell av underarmen. Denna modell, i kombination med lokaliseringsmetoden, används sedan för att tolka ny EMG-data, för att känna igen olika rörelser. Sammanfattningsvis diskuteras hur dessa metoder kan tillämpas inom muskelrehabilitering, styrning av handproteser, och i nya gränssnitt för människa-maskininteraktioner.

Abstract

The ability to generate and control movement is essential for human interactions and overall well-being. Neuromuscular impairment caused by neurological injuries and diseases, such as stroke or limb amputation, severely limits the ability of affected individuals to interact with the surrounding environment, necessitating advanced strategies for rehabilitation and restoration of motor function. Voluntary muscle contractions are initiated by motor neurons that transmit electrical impulses, or action potentials, which propagate along nerves and throughout muscle fibres. A single motor neuron and its associated muscle fibres form a motor unit, which creates a direct link between the nervous system output and electrical signals generated by muscles. High-density surface electromyography (HDsEMG) is a powerful non-invasive technique for analysing neuromuscular function by capturing the electrical activity of motor unit action potentials. However, extracting meaningful information from HDsEMG recordings remains a significant challenge due to the complex spatial and temporal overlap of motor unit activity, particularly in regions with high muscle density, such as the forearm.

This dissertation consists of an introduction, background, and four papers presenting novel methods and algorithms for analysing HDsEMG data. **Paper I** introduces a new algorithm for motor unit decomposition, combining Fast Independent Component Analysis with an iterative peel-off scheme based on spike-triggered averaging and Principal Component Compression. **Paper II** presents a method for localizing motor unit action potentials, identified with the decomposition method in Paper I, estimating the centre of electrical activity using a surface fitting approach and an analytical volume conductor model. **Paper III** shifts the focus from motor units, and the reliance on decomposition, to localization of individual time-domain peaks directly in the HDsEMG data, and introduces a new technique for constructing a three-dimensional model of muscle activity. In this model, individual muscles are represented as distinct volumes,

which are subsequently used to classify additional HDsEMG signals into specific muscle activations. **Paper IV** extends this approach, applying the volume-based muscle representations to gesture classification and evaluates their generalizability across participants and for novel gestures beyond the original model.

List of papers

Included

I. **Compressed spike-triggered averaging in iterative decomposition of surface EMG**
Lundsberg, J., Björkman, A., Malesevic, N., & Antfolk, C.
Published in: Computer Methods and Programs in Biomedicine, *228*, 107250. (2023)

Author's contributions: Study design, part of data collection, design and implementation of algorithms, analysis of results, manuscript writing.

II. **Inferring position of motor units from high-density surface EMG**
Lundsberg, J., Björkman, A., Malesevic, N., & Antfolk, C.
Published in: Scientific Reports, *14*(1), 3858, (2024)

Author's contributions: Study design, part of data collection, design and implementation of algorithms, analysis of results, manuscript writing.

III. **Muscle activity mapping by single peak localization from HDsEMG**
Lundsberg, J., Björkman, A., Malesevic, N., & Antfolk, C.
Published in: Journal of Electromyography and Kinesiology, 81, 102976. (2025)

Author's contributions: Study design, data collection, design and implementation of algorithms, analysis of results, manuscript writing.

IV. **Generalizable gesture classification of HDsEMG using volume representations of muscles averaged across multiple individuals**
Lundsberg, J., Björkman, A., Malesevic, N., & Antfolk, C
Manuscript

Author's contributions: Study design, design and implementation of algorithms, analysis of results, manuscript writing.

Related

1. **Motor Unit localization from surface EMG**
Lundsberg, J., Antfolk, C., Malesevic, N
Conference abstract for poster presentation at Rehabweek 2022

2. **Estimating the neural spike train from an unfused tetanic signal of low-threshold motor units using convolutive blind source separation**
Rohlén, R., **Lundsberg, J.**, & Antfolk, C.
Published in: Biomedical engineering online, 22(1), 10, (2023)

3. **A fast blind source separation algorithm for decomposing ultrafast ultrasound images into spatiotemporal muscle unit kinematics**
Rohlén, R., **Lundsberg, J.**, Malesevic, N., & Antfolk, C.
Published in: Journal of Neural Engineering, 20(3), 034001, (2023)

4. **Mapping the spatial distribution of motor unit activity in forearm muscles**
Lundsberg, J., Malesevic, N., Antfolk, C
Conference abstract for poster presentation at Rehabweek 2023

5. **Muscle activity mapping by 3-dimensional localization of motor unit action potentials from high-density surface electromyography**
Lundsberg, J., Malesevic, N., Björkman, A., Antfolk, C.
Conference abstract for oral presentation at ISEK 2024

Acknowledgements

This work would not have been possible without a number of people who deserve to be acknowledged. I want to dedicate this section to expressing my sincerest gratitude to those who made this entire project into such a fantastic, wonderful, and worthwhile journey.

First of all, I wish to thank my main supervisor **Christian Antfolk**, for getting this project started. Your door has always been open, and I always felt you were right there, ready to answer questions or provide any resources I needed. You gave me the freedom to try new things, to make decisions on what to do and which direction to take; this trust in my judgement has been truly motivating, and I have grown so much because of it. I wish to thank my co-supervisor **Nebojša Malešević**, for not only being an amazing supervisor but also a great friend. We've had countless discussions on so many different things; the only throughline I can think of is how incredibly enjoyable they have been. Your perspective is always valuable, and I've learnt a ton from you, whether you realize it or not. We've also travelled to so many conferences and places; the unforgettable memories are honestly too many to list. It's clear to me how our interactions have elevated my time at the department from mere work to a great living. I wish to thank my other co-supervisor **Anders Björkman**, for providing me with much needed motivation. You've made my work feel more useful, your comments always inspire me, and I've always looked forward to hearing from you. You've also made me a better writer, by returning all my drafts predominantly in the colour red; although daunting to work through, I sincerely appreciate all your feedback.

To former members of the Neuroengineering group: Thank you **Pamela**, for being the vanguard PhD of our group, and your great company in all our meetings. Thank you **Alexander**, for diving deep into endless fascinating theoretical and philosophical discussions with me, and for helping me improve my scientific rigor. Thank you **Jia**, for

providing tons of highly contagious positivity and entertainment to the office, for our long conversations and longer badminton matches. Thank you **Robin**, for inspiring me with your productivity and hard work, and your eagerness to discuss exciting new possibilities in our meetings.

Beyond our group, I wish to thank **Ulrika**, **Ammi**, and **Désirée**, for all the administrative work, always clearing up my confusion, and making everything simple and smooth. Thank you **Ola**, for helping me solve problems in LabVIEW, and showing me all its depths. I wish to thank all those who volunteered to participate in my data collection, despite our group's reputation for sticking needles into arms. And of course, thanks to **everyone** at the Department of Biomedical Engineering, who've been such wonderful company, engaged in all the thoroughly entertaining conversations, and created this amazing atmosphere to work in.

I wish to thank my friends and family, for keeping me grounded to reality, and reminding me that I've been doing some pretty cool stuff all these years. In particular, I wish to thank my **parents** and my **sister**, for providing unconditional support. You've always been there, ready to help me with anything, and you inspire me to be my best.

Lastly, I wish to give my thanks to all the researchers and engineers who came before me, who laid the vital groundwork that made my work possible, and to the **Promobilia Foundation**, which has sponsored this project.

Author's declaration of generative AI assistance

In the spirit of transparency and acknowledging the evolving landscape of research tools, it is important to disclose the use of generative AI tools, such as large language models, in the writing process. OpenAI's ChatGPT4o large language model was utilized to reword, restructure, and provide feedback on various paragraphs in the preparation of this dissertation. While the AI tool was used to enhance text for clarity and structure, the content and ideas are entirely the author's own. All output produced by AI was carefully reviewed and edited, sentence by sentence, ensuring the final work accurately reflects the author's intentions. The author is fully and solely accountable for the work in this dissertation.

Notations

Time-domain variables

$x[n]$	The discrete signal in the time-domain for samples $n = 0, 1, \dots, N-1$
N	The number of samples in a signal or window
f_s	The sampling frequency in Hz
μ	The sample mean of $x[n]$
μ_r	The r-th central moment of $x[n]$
σ	The standard deviation of $x[n]$

Frequency-domain variables

$X[k]$	The Discrete Fourier Transform of $x[n]$ for frequency bins $k = 0, 1, \dots, M-1$
M	The number of frequency bins
f_k	The frequency in Hz at bin k, where $f_k = \frac{kf_s}{N}$
$P[k]$	The power spectral density estimate, at bin k

Statistical notations

Z	A random variable of a sample space

$E\{Z\}$ The expected value, or true mean, of a random variable Z

Vectors and Matrices

w The scalar value w

$\boldsymbol{w}$ The vector $\boldsymbol{w}$

$\boldsymbol{W}$ The matrix $\boldsymbol{W}$

$\boldsymbol{W^T}$ The transpose of matrix $\boldsymbol{W}$

Functions

$sgn(x) = \begin{cases} 1\ if\ x > 0 \\ 0\ if\ x = 0 \\ -1\ if\ x < 0 \end{cases}$ The sign function

$\delta(C) = \begin{cases} 1\ if\ C\ is\ true \\ 0\ if\ C\ is\ false \end{cases}$ The indicator function

Acronyms and Abbreviations

EMG Electromyography

iEMG Intramuscular Electromyography

HDsEMG High-Density surface Electromyography

ECG Electrocardiography

CNS Central Nervous System

PNS Peripheral Nervous System

EPSP Excitatory Postsynaptic Potential

IPSP Inhibitory Postsynaptic Potential

EPP End Plate Potential

MUAP Motor Unit Action Potential

ACSA Anatomical Cross-Sectional Area

PCSA Physiological Cross-Sectional Area

EDC Extensor Digitorum Communis

PSD Power Spectral Density

PLI Power-Line Interference

RMS Root-Mean-Square

STA Spike-Triggered Averaging

CoA Centre-of-Activity

FWHM Full Width at Half-Maximum

k-NN k-Nearest Neighbour

LDA Linear Discriminant Analysis

SVM Support Vector Machine

PCA Principal Component Analysis

ICA Independent Component Analysis

BSS Blind Source Separation

CKC Convolution Kernel Compensation

HMI Human-Machine Interface

Chapter 1

Introduction

From the largest animal to the smallest bacteria, movement is arguably the most fundamental aspect of life. All living beings move to affect change and alter their surrounding environment. We act our will upon the world using hundreds of muscles throughout our bodies. These muscles, controlled by the nervous system, are our primary tools for interacting with the world. The loss of muscle control can be life-altering, be it through conditions such as stroke, neurological diseases, spinal cord injury, or amputation of limbs. When movement is compromised, so too is a person's ability to express themselves, interact with others, and engage fully with their environment. The ability to move and interact with the world depends on highly intricate coordination between muscles, which, when disrupted, significantly impacts an individual's quality of life.

The purpose of this dissertation is to contribute to the ongoing effort to restore and even enhance human functionality. At the centre of this effort is electromyography (EMG), a technique for measuring and recording the electrical activity of muscles[1,2]. By analysing this activity, EMG enables investigations into the neurophysiological signals underlying movement. The intricate relationship between neural commands and muscle contractions is explored using sophisticated signal processing algorithms that allow us to enhance our understanding of the motor system. The utility of EMG extends beyond basic physiology, however, to a wide range of practical applications. This includes assessment of various neurological diseases or injuries[3-5], such as cerebral palsy or stroke, where proper assessments are critical to guide treatment strategies. EMG can also be used as a control signal in human-machine interfaces (HMIs), most widely used in prosthetic limbs, restoring movement to amputees[6-10]. Other HMIs include sign language recognition and speller systems to improve communication[11,12]. With a vast number of potential applications, there is significant value in improving the signal processing algorithms which extract meaningful information from EMG. This dissertation pertains to the

development of signal processing methods, to enable EMG as a diagnostic and exploratory tool, and as input to human-machine interfaces (HMIs).

EMG comes in several forms, mainly intramuscular EMG (iEMG), through invasive recordings, and surface EMG (sEMG), recorded non-invasively from the skin; although preferable, non-invasive recordings are noisier and more complex. High-density EMG is where many electrodes in a grid record simultaneously over a larger area, which can be both invasive and non-invasive. The most common type is the non-invasive high-density surface EMG (HDsEMG), used throughout this dissertation. HDsEMG generates a vast amount of data which not only enables but also necessitates advanced processing algorithms. These algorithms must disentangle meaningful physiological information from artifacts, noise, and overlapping signals from multiple muscles.

In EMG analysis, ***decomposition*** is the concept of separating individual components from a compound signal. Decomposition methods make use of statistical properties of the signal and electrode grids (in most cases), to separate the activity of individual motor units from the global EMG recording. These methods face challenges in both reliability and yield; however, motor unit decomposition is a fast-moving field with significant progress year after year. With improved decomposition algorithms come deeper understanding of the control strategies employed by the nervous system, clinical assessment possibilities, and the potential for HMI control at a more granular level. ***Localization*** is the attempt to trace the origin of a signal, to map muscle activity to a physical position. Localization techniques leverage the spatial information inherent to high-density electrode grids to infer the anatomical source of electrical activity. The spatial interpretation of the EMG signal allows for intuitive analysis and understanding of muscle activity. Alongside physiological and anatomical models, accurately localizing EMG activity can deepen our understanding of the functional organization of neuromuscular activity; it may provide valuable feedback in clinical settings and identify the activity of individual muscles to control HMIs. In this dissertation, ***modelling*** refers to both electrophysiological and physical representations. An electrophysiological model may capture how signals propagate through tissue, which is critical to perform localization. Whereas a physical model may be used to visualize muscle activity and aid gesture recognition to control HMIs.

Collectively, the decomposition, localization, and modelling methods provide ways to transform EMG data into interpretable, meaningful, and actionable information; information that can be used by clinicians, researchers, and designers of assistive devices. The presented work builds upon plenty of existing theory in neurophysiology, electrical engineering, and signal processing, while introducing novel methods to incrementally move the field forward.

1.1 Aim and scope

The work presented in this dissertation covers new methods for processing and interpreting the electrical signals produced by muscle contractions, related to decomposition, localization, and modelling, with the aim of extracting intuitive and actionable information for clinicians, patients, and researchers. Although multiple input modalities exist which may solve the problems tackled here, this work focuses on signal processing of non-invasive HDsEMG data. Furthermore, while the methods may extend to other muscle groups or limbs, the work here is mostly limited to forearm muscles.

1.2 Outline

The remainder of this dissertation is structured in two parts. **Part I** serves as a background which aims equip the reader with all essential information required to understand the papers and the context in which they were written. It consists of four chapters. *Chapter 2* describes the neuromuscular system anatomically and physiologically. *Chapter 3* provides an overview of EMG, how muscle signals are recorded and the various electrodes that are used. *Chapter 4* dives into the relevant signal processing techniques and their underlying theory. *Chapter 5* describes various applications which utilize EMG and potential obstacles to overcome. **Part II** includes the scientific contribution of this dissertation in terms of four papers. The papers are appended at the end of this dissertation and summarised in *Chapter 6*. *Chapter 7* contains a broader discussion which concludes the dissertation.

Part I

Background

Chapter 2

The neuromuscular system

2.1 Anatomical and functional terminology

In order to describe various structures and properties of the body without confusion, establishing correct terminology is important. This section pertains to the various anatomical and functional terms used throughout the dissertation to describe positions and movements.

Positions

Anatomical descriptions of the body are based on the ***standard anatomical position***. In this position a person is standing with the palms of the hands facing forward and the thumbs pointing outwards. The arms are beside the body and the feet are parallel and separated at shoulder width. Anatomical references to the right and left side of the body are from the perspective of the subject and not the observer. ***Anterior*** and ***posterior*** describe positions that are at the front and back of the body respectively, from the standard anatomical position. In this position, e.g., the palm of the hand to the arm crease is the anterior side and the back the hand to the elbow is the posterior side. ***Ventral*** and ***dorsal*** also refer to the front and the back of the body but in relation to the spine, derived from the underbelly and backside respectively. It is typically used in neuroanatomy or descriptions of non-human animals. ***Superior*** and ***inferior*** describes positions that above or below, in relation to another part of the body. ***Proximal*** and ***distal*** describe positions that are closer to or farther from the body, used extensively when describing the body's limbs. E.g., the elbow is proximal to the hand, and the fingers are distal to the wrist. ***Superficial*** and ***deep*** describe the structures that are closer to or further from the skin surface of the body. Muscles of the forearm are often separated into superficial and deep muscle groups. ***Medial*** and ***lateral*** describe position that are closer to or farther from the midline of the body. Thus, from the standard anatomical position, the little finger is on

the medial side whereas the thumb is on the lateral side of the hand. ***Radial*** and ***ulnar*** are used to describe positions in relation to the radius and ulna bones of the forearm specifically. Radial and ulnar are interchangeable with lateral and medial, but due to the rotations of the forearm, the former terminology is less confusing.

Planes

There are three anatomical planes that a commonly referred to, which divide the body with two-dimensional surfaces. The ***sagittal plane*** divides the body into a right and a left side. The ***frontal plane*** divides the body into an anterior and a posterior (front and back) portion. The ***transverse plane*** divides the body horizontally into a superior and inferior (upper and lower) portion. Of particular relevance is the transverse plane, in which cross-sectional images of limbs are made.

Muscles

To create motion, a muscle is anchored between two points, referred to as its ***origin*** and ***insertion***. The origin of a muscle tends to be a more proximal and stable position compared to the insertion. The insertion tends to be the structure with less mass which moves upon a muscle contraction. ***Intrinsic*** muscles are muscles with its origin and insertion located within the part of the body they act on, an example of which are the thenar group of muscles, located completely within the hand. ***Extrinsic*** muscles have their origin and muscle bellies outside the area where the muscle tendon inserts, such as the finger flexor muscles originating from the elbow and have their muscle bellies in the forearm with long tendons traveling into the hand, inserting on individual fingers. Muscles often come in ***agonist*** and ***antagonist*** pairs, defined by how they cause and inhibit a specific motion. An agonist muscle is a muscle which produces the main force to generate an action, whereas an antagonist muscle produces an opposing force over the same joint. A ***synergist*** muscle is a muscle which aids the agonist muscle in its action.

Motion

The origin and insertion of skeletal muscles that move the body are typically attached to two separate structures. ***Flexion*** and ***extension*** refer to a movement which decreases or increases the joint angle between two body parts; thus, closing the hand makes use of flexor muscles and opening the hand makes use of extensor muscles. ***Abduction*** and ***adduction*** refer to a movement which brings a structure away from or towards the midline of the body part in question. ***Pronation*** and ***supination*** of the forearm refer to a rotation so that the palm of the hand faces the posterior direction and the anterior direction respectively, with regards to the standard anatomical position; thus, when the palm of the hand is resting on a table it is in a prone position. An ***isometric*** contraction

refers to a contraction where the length of the muscle remains static. An ***isotonic*** contraction refers to a contraction where the tension, or force, produced by the muscle remains static. ***Concentric*** and ***eccentric*** contractions refer to a contraction during which the length of the muscle decreases or increases.

2.2 The nervous system

The human nervous system is divided into two main anatomical parts, the central nervous system (CNS) and the peripheral nervous system (PNS). The CNS consists of the brain and the spinal cord, and is responsible for processing incoming (afferent) information and initiating outgoing (efferent) commands[13,14]. The brain comprises two hemispheres, a left and a right. It is anatomically organized in distinct subdivisions or lobes, with multiple gyri (ridges) and sulci (grooves). Notably, the primary somatosensory cortex (S1), where afferent sensory information is received, and the primary motor cortex (M1), from where muscle commands are sent to the spinal cord, are both organized in a topographical manner as well. These adjacent interconnected regions[15], M1 located just anterior to S1, are structured in a way which creates a map of the body, where various regions represent specific points across the body. This representative map is also referred to as a homunculus, and was demonstrated as early as 1937[16]. While S1 reflects the input to sensory neurons from receptors throughout the entire body, M1 engages specific muscles, far fewer in number, to control the movement of limbs, resulting in some topographical differences. These differences are exemplified with more recent neuroimaging studies showing separate representations in the motor cortex of the same digits performing opposing actions controlled by different muscles, such as grasping and releasing a ball[17], revealing a functional organization present in M1 that is absent in S1.

The motor system is complex, with several areas in the brain that are important for motor control, which can collectively be referred to as the motor network. The motor network, especially M1, contains upper motor neurons which send commands down the spinal cord to pattern generating networks. In the spinal cord, coordinated muscle activation patterns for various actions are generated, as evidenced by rhythmic activation of specific muscles in spinal cord stimulation studies[18,19]. The activation patterns are relayed by lower motor neurons in the ventral horn of the spinal cord, which defines the border between the CNS and the PNS, to muscles throughout the body. The efferent division of the PNS is further subdivided into a somatic nervous system and an autonomic nervous system, where the former is made up of the fibres connecting motor neurons in the spinal cord to skeletal muscles throughout the body[13]. In the PNS, neuron fibres (axons) are bundled together with connective tissue along common pathways which are called nerves. There are 31 pairs of spinal nerves that connect both afferent and efferent fibres to the spinal cord (Figure 2.1), called roots, which are grouped by the vertebral levels

they exit: cervical (C1-C8), thoracic (T1-T12), lumbar (L1-L5), sacral (S1-S5), and coccygeal (CO1). Of particular relevance to human limbs and the generation of movement are the cervical nerves which innervate neck, shoulders, arms, and hands, as well as the lumbar nerves associated with the lower abdomen, hips, and legs. The nerve roots branch out and merge with one another at several points, forming the major nerves supplying the upper and lower limbs. In the cervical spine, branches from the C5 to T1 roots eventually merge into three large nerves innervating the upper limb: the radial, medial, and ulnar nerves. These nerves are the communication pathways that enable the wide range of dexterous capabilities of human hands.

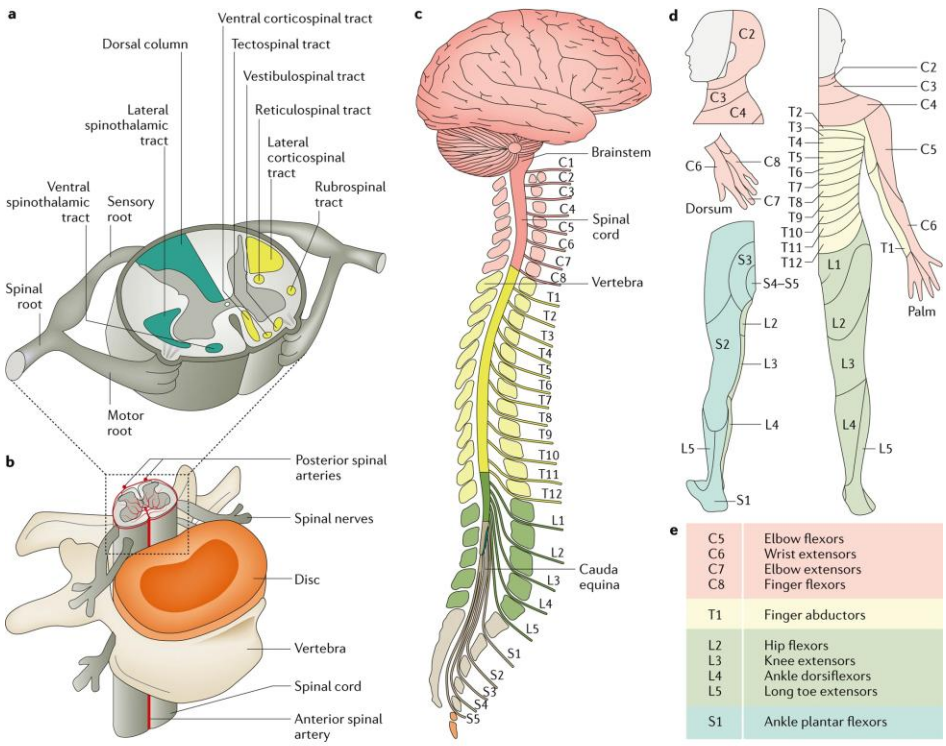

*Figure 2.1: The spinal cord and the nerve roots of the various vertebral levels are shown in **a**, **b**, and **c**. The colours in **c**, **d**, and **e** represent the different vertebral levels. The dermatomes for afferent nerve fibres are shown **d**, with a posterior view (left) and anterior view (right). Reused with permission from Ahuja et al (2017)[20], © 2017, https://doi.org/10.1038/nrdp.2017.18.*

2.3 Neurons

The foundation of neurobiology is the neuron itself. While there are many types of neurons in the nervous system, they are all cells specialized for communication. The neuron is typically divided into three parts; the soma, which is the cell body containing the nucleus; the dendrites, which receive input signals; and the axon, which transmits an output signal[13]. Neurons are connected through chemical synapses, passing information from a presynaptic axon terminal, across a synaptic cleft, to a postsynaptic region located mainly on the dendrites or the adjacent cell body. Through a vast number of synapses, each neuron may connect to any number of other neurons, generating incredibly complex networks.

2.3.1 Electrochemical communication

The signalling system of neurons is made up of local changes in ion concentrations across the cell membrane, propagating from neuron to neuron as an electrochemical wave. At rest, each neuron has a potential difference across the membrane of approximately -70 mV. That is, along the cell membrane, the extracellular fluid is positively charged compared to the intracellular fluid. This resting potential is mainly generated by a balance between a surplus of extracellular sodium and chlorine ions, and a surplus of intracellular potassium ions.

There are two types of changes in membrane potentials, graded potentials and action potentials. Graded potentials are small, gradual, changes which are generated in the postsynaptic region of the receiving neuron. Action potentials, on the other hand, are large all-or-nothing changes which are generated when a neuron is transmitting a signal.

Graded potentials

When the postsynaptic dendrite receives a signal, neurotransmitters from the presynaptic axon terminal flood the synaptic cleft and bind to receptors on the postsynaptic cell membrane, resulting in the opening of ligand-gated ion channels in the membrane. The subsequent flow of ions generates a graded potential which is either excitatory or inhibitory, depending on which neurotransmitter is released. The most common excitatory neurotransmitter is acetylcholine, whereas the most common inhibitory neurotransmitter is GABA (gamma-aminobutyric acid). An *excitatory postsynaptic potential* (EPSP) opens sodium and potassium channels resulting in a depolarization of the membrane potential, followed by a slow repolarization. An *inhibitory postsynaptic potential* (IPSP) instead opens chlorine and potassium channels resulting in a hyperpolarization of the membrane potential. A neuron may receive many postsynaptic

potentials from any number of other neurons; the summation of these graded potentials then propagates throughout the cell body.

Action potentials

The bordering region between the cell body and the axon is named the axon hillock, which contains a vast number of voltage-gated ion channels. When depolarization of the membrane potential at the axon hillock exceeds a certain threshold, these ion channels open, causing a fast inward flow of sodium ions which further depolarizes the membrane potential. This positive feedback ensures that all voltage-gated ion channels open, which initiates an action potential that propagates throughout the axon. Following the influx of sodium ions, is a slower outward flow of potassium ions, which repolarizes the membrane potential (Figure 2.2). The sodium channels proceed to an inactive state, and within one to a few milliseconds that region is incapable of initiating another action potential, no matter the strength of the stimulus, which is said to be the *absolute refractory period*. The strong repolarization caused by the exodus of potassium ions create a *relative refractory period* which can last roughly 15 ms, where another action potential is possible but requires a considerably greater stimulus[13]. The refractory period prevents the backward propagation of action potentials and plays a key role in the *binary rate coding* of information in the nervous system[13,21,22].

The all-or-nothing property of action potentials means that the amplitude of the signal cannot convey meaningful information. Instead, the nervous system relies on the frequency of transmitted action potentials to code information. A higher intensity of both afferent sensory input and efferent motor output is conveyed with a higher frequency of action potentials, while each individual action potential produces a standardized response in the subsequent neuron or muscle fibre. Thus, these signals can be conceptualized as *binary spike trains* of action potential discharges.

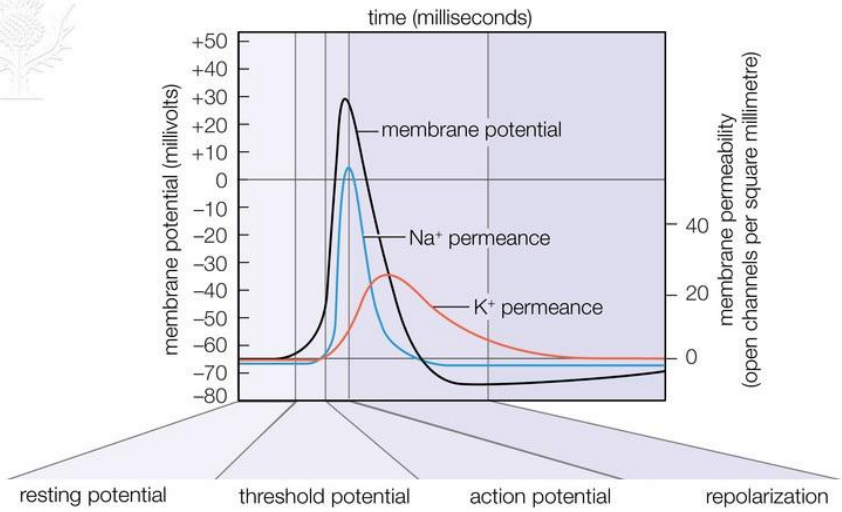

Figure 2.2: The membrane potential of a neuron during an action potential, and the density of open voltage-gated sodium (Na+) and potassium (K+) channels. From Britannica ImageQuest, © Encyclopaedia Britannica, Accessed April 25, 2025, https://quest.eb.com/images/309_366166.

2.3.2 Neuron conduction velocity

Another important property of neurons is the *conduction velocity* of the axon. Action potentials need to traverse large distances very quickly, which is especially true for motor neurons, as they connect to muscle fibres throughout the body all the way from the spinal cord. The main strategy used by the nervous system to increase conduction velocity is to insulate the membrane of axons with non-conductive sheets of myelin. The un-insulated axon has a higher internal resistance to local currents due to a leakage of charge across the membrane, as the action potential wave travels along the axon. The myelin sheets, rich in lipids, increases the electrical resistance and thus reduces the amount of leakage current across the membrane, allowing the flow of ions to spread farther along the axon instead. Since action potentials do not occur in the myelinated sections, the coating is briefly interrupted with regions containing high concentrations of voltage-gated channels, called nodes of Ranvier. Thus, the action potential is regenerated at each node, creating a jumping effect from node to node (Figure 2.3), which can result in a hundredfold increase in conduction velocity. Between small unmyelinated fibres to large myelinated fibres, conduction velocities can range from 0.5-100 meters per second[13]. Demyelination of axons is a significant effect of neurodegenerative autoimmune diseases such as multiple sclerosis[23], as well as aging and stroke[24], and spinal cord injury[25].

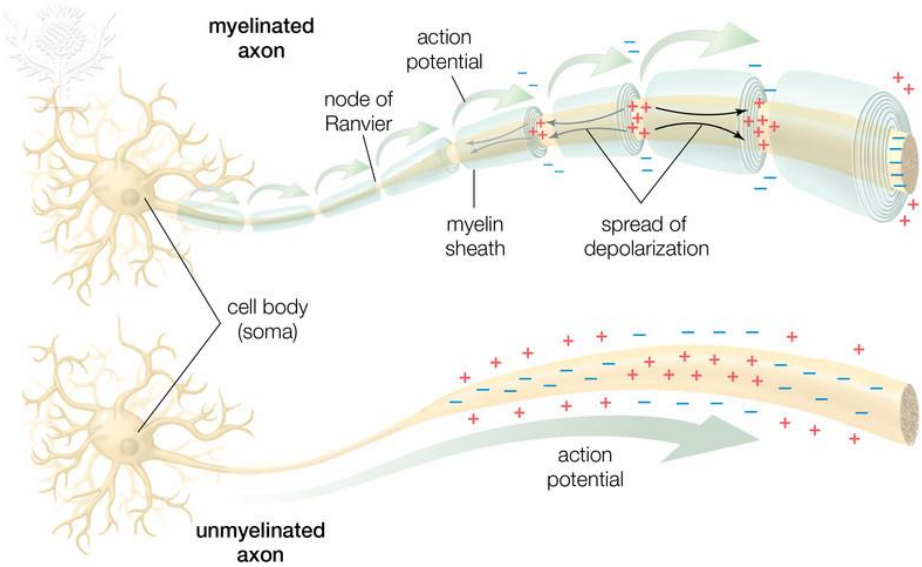

Figure 2.3: The faster 'jumping' action potential propagation in a myelinated neuron (top) and the slower propagation in an unmyelinated neuron (bottom). From Britannica ImageQuest, © Encyclopaedia Britannica, Accessed April 25, 2025, https://quest.eb.com/images/309_366329.

2.4 Neuromuscular junctions

The neuromuscular junction is the synapse between a lower motor neuron and a muscle fibre. As the motor neuron axon reaches the muscle, it branches out to multiple fibres. Each branch forms a junction with a muscle fibre, connecting the axon terminal to what is called the *motor end plate* of the fibre. A single motor neuron and the connected fibres define a single ***motor unit***. From the axon terminal the neurotransmitter acetylcholine is released, binding to ion channels in the motor end plate, allowing sodium and potassium ions to flow across the muscle fibre membrane. The flow of ions creates a local depolarization of the muscle fibre membrane called the end-plate potential (EPP), analogous to the neuron-neuron EPSP; although, there are key differences between neuromuscular junctions and inter-neuronal synapses. Neuromuscular junctions are always excitatory, in contrast to inhibitory potentials, IPSPs, generated at some synapses. Thus, to inhibit a muscle fibre contraction, the motor neuron itself needs to receive inhibitory input in the CNS. One of the most important distinctions is the magnitude of the EPP, which is much larger than that of the EPSP. Multiple EPSP are required to elicit an action potential in a neuron, whereas a single EPP is typically enough to generate an action potential in a muscle fibre[13,26]. The motor end plate has a larger surface area due

to folds in the membrane with many more ion channels. The local currents at the motor end plate propagate to the adjacent membrane containing voltage-gated sodium channels which initiates the muscle fibre action potential.

The motor end plate is typically located near the middle of the muscle fibre, wherefrom the action potential propagates, with a typical conduction velocity between 3-5 meters per second, in both directions along the surface of the fibre and throughout a tubular system within the fibre. The action potential does not directly activate the force-generating mechanism of the fibre, rather, it stimulates the release of calcium ions within the cell which act directly upon the muscle fibre filaments resulting in a contraction.

Muscle fibre twitches

While the action potential lasts 1 to 2 milliseconds the following mechanical contraction of the fibre can last 100 milliseconds or more. There is additionally some delay between the beginning of the action potential and the initial mechanical tension generated, referred to as the latent period, which can be around 10 milliseconds with varied estimates. These divergences between electrical excitation and mechanical contraction play a significant role in understanding the relationship between EMG and muscle force, especially crucial for applications in prosthetic control. Each action potential generates a single muscle fibre twitch with a contraction phase and a relaxation phase (Figure 2.4A). With increased frequency of action potentials, the twitch responses increasingly overlap, generating greater tension in the fibre (Figure 2.4B). At high enough frequencies, the twitch responses fuse together, called a fused tetanic contraction, which generates a consistent maximal tension in the muscle fibre.

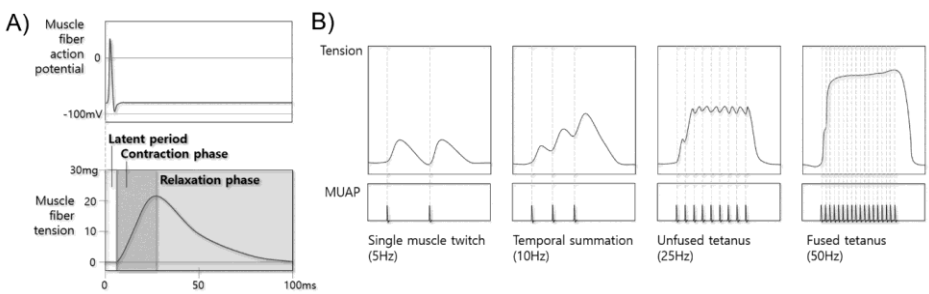

Figure 2.4: The action potential to muscle twitch tension relationship. Edited and reused with permission from Park (2023)[27], © 2023, https://doi.org/10.1007/978-3-031-20784-6_9.

2.5 Motor units

The term "motor unit" was introduced just over 100 years ago[28,29], laying the foundation for our understanding of how the nervous system controls motor output[29,30]. The motor unit is the smallest discrete component of voluntary contraction, consisting of a single lower motor neuron and all individual muscle fibres it innervates. The action potential of a single lower motor neuron triggers an action potential along all muscle fibres of that motor unit, causing a short contraction and greatly amplifying the electrical signal in the process. In the context of EMG, the importance of the motor unit is that it forms a one-to-one connection between a subset of muscle fibres and the output of the nervous system. Motor units exhibit a range of structural and functional properties that vary both across muscles and between individuals. These properties influence how motor units generate force, how they are recruited during voluntary contractions, and how they contribute to the neuromuscular strategies underlying movement. For each motor unit, the signal shapes of repeated motor unit action potentials (MUAPs) are almost identical, and the resulting contractile force is determined by the MUAP frequency and the fibre type. Identifying which motor units are active, and the time instances of action potential discharges, thus identifies the output of the central nervous system and provides insight into the neural strategies of voluntary muscle control.

2.5.1 Muscle fibre types

The cells that compose muscles (myocytes) display a great deal of variety in both form and function. There are three types of muscle cells: cardiac, skeletal, and smooth myocytes. Skeletal myocytes form the muscles under voluntary control and are responsible for the movement of limbs by connecting the bones across various joints in the body. Skeletal myocytes have a long fibrous shape and are thus merely referred to as muscle fibres. Individual muscles are made up of hundreds to hundreds of thousands of muscle fibres, and the various architectures and physiological properties affect their speed, fatigue resistance, and effective force.

Muscle fibres are mainly classified based on their mechanical properties, fast or slow, and their metabolic properties, oxidative or glycolytic. Oxidative fibres are reliant on aerobic metabolism, i.e. blood flow to deliver oxygen and fuel to the fibre. These fibres are therefore surrounded by many small blood vessels and contain large amounts of myoglobin, resulting in a distinctive red colour, and thus commonly referred to as red muscle fibres. Glycolytic fibres are less reliant on blood flow, making use anaerobic metabolism through large stores of glycogen. These fibres are pale due to a low amount of myoglobin, and thus commonly referred to as white muscle fibres. With some degree of overlap, muscle fibres are mainly grouped into ***type 1*** (slow oxidative), ***type 2a*** (fast

oxidative/glycolytic), and ***type 2x*** (fast glycolytic) fibres. Type 1 fibres are typically slow, small, highly fatigue resistant, and produce low force. Whereas type 2a fibres are typically fast, large, quite fatigue resistant, and produce moderate force. Type 2x fibres are also typically fast and large, but are quick to fatigue, and produce high force. While muscles contain a mix of fibre types, critically, the motor neuron in each motor unit innervates muscle fibres of the same type. Thus, the fibre type properties exhibited by individual muscle fibres are also properties of the entire motor unit.

2.5.2 Innervation ratios

The force produced by each motor unit twitch depends on the number of fibres in it. The number of muscle fibres in a motor unit is called the *innervation ratio*, which varies greatly between muscles. There are typically *hundreds* to *thousands* of fibres in a motor unit, depending on the level of precision required for a specific movement. The innervation ratio of muscles controlling the precise movement of fingers is far lower than that of crude but powerful leg muscles. The typical approach to derive the innervation number of muscles have been by counting, from cadavers, the total number of muscle fibres and the motor neurons innervating the muscle. However, there is a significant range of motor unit innervation ratios within a muscle, which is much more difficult to assess[31]. One method of measuring individual motor unit innervation ratios is through the glycogen depletion technique[31-33], where isolated motor neurons are stimulated long enough to reduce muscle fibre glycogen levels and the number of affected fibres are then counted. This technique, however, is limited by fibre type and that only a single motor units can be assessed at a time. An important property to consider is that the distribution of motor unit innervation ratios is also highly skewed. A large number of motor units innervate few muscle fibres, while a minority innervate many, following an exponential distribution [31,34,35]. Through a proper recruitment strategy, this allows for great precision in low-force contractions, while maintaining a large range of force output.

2.5.3 Discharge rates

In addition to the number of active motor units, the *discharge rate* of each motor neuron contributes directly to muscle force. The relationship between discharge rate and force output follows a nonlinear force-frequency curve, where force initially increases steeply with rising frequency, then plateaus approaching the mechanical contraction limit[31,34,36]. For the digit flexor muscles, Fuglevand et al thoroughly described this force-frequency relationship, while noting differences between motor unit types[36]. They stated that the minimal effective firing rate was around 8 Hz, which for slow fibres produced 40% of their maximum force, but only around 17% of maximum force for fast fibres. Thus, the slow fibres reached their half-maximum force already at 9.1 Hz, whereas the fast fibres

required 15.5 Hz. Since temporal summation occurs more easily for slow fibre twitches, this results in a much steeper force-frequency curve, where near-maximal force is reached at much lower discharge rates. The slower motor units therefore appear to have less capacity for adapting their force output through *rate modulation* of action potential discharges.

2.5.4 Recruitment strategy

The total force a muscle produces depends not only on rate modulation, but also the motor unit number and the recruitment strategy. The general strategy of the nervous system is to recruit motor units in an orderly fashion following the *size principle*[29,37]. Smaller type 1 motor units are activated first, followed by larger type 2a then 2x units as the force demand increases. This orderly recruitment ensures efficient force production and allows the nervous system to scale the force output across a broad range, while maintaining precision in at low forces. Thus, it is worth noting that low-force contractions, that are common in EMG recordings, are biased towards type 1 motor units. Furthermore, since type 1 units produce lower amounts of force, a great number of them activate rapidly as force increases[31,34,35,38]. To generate a roughly linear increase in force, the number of active motor units increase in a logarithmic fashion, reflecting the exponential distribution of motor unit innervation ratios. While the size principle generally holds for isometric contractions, some deviations have been observed. For concentric contractions, the number of recruited motor units increases, whereas for eccentric contractions, some studies have shown an altered recruitment order[31].

2.6 Muscle anatomy

2.6.1 Muscle architecture

Skeletal muscles consists of organized bundles of muscle fibres, called muscle fascicles, wrapped in layers of connective tissue, or fascia. The muscle fibres are in turn composed of many myofibrils (Figure 2.5). Each myofibril consists of contractile segments, called sarcomeres, that are chained together along the muscle fibre. The contracting force is produced by sliding filaments within the sarcomeres, where actin filaments form a "ladder" upon which the motor protein myosin "climbs". The amount of force a muscle can produce depends on the cross-sectional area of the muscle, i.e. the number of filaments per unit of area. The contraction length, in contrast, depends on the length of fibres.

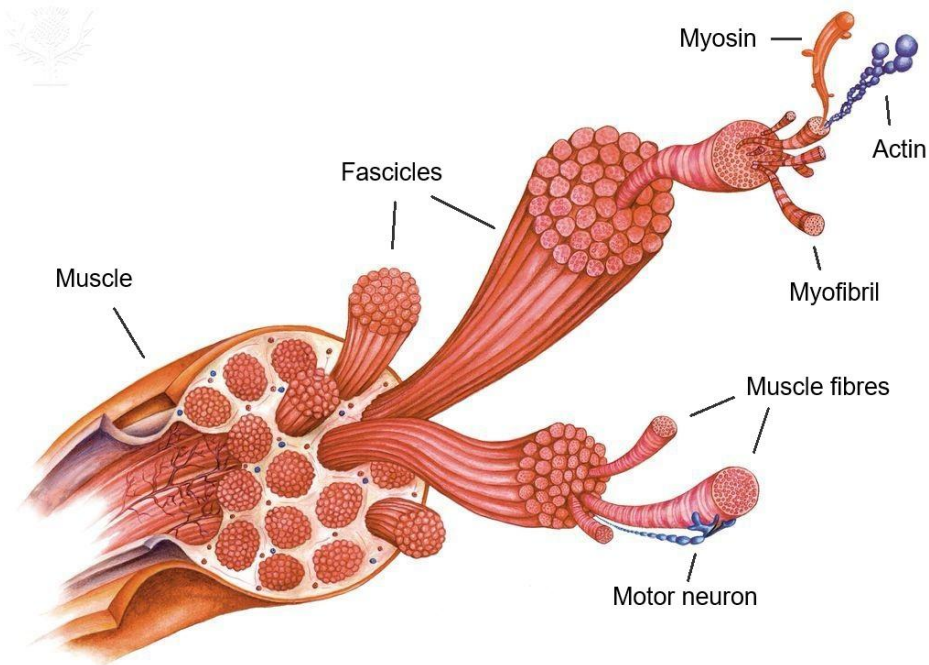

Figure 2.5: The architecture of a muscle and its fibres, down to the force-generating filaments. Edited from Britannica ImageQuest, © BSIP, Accessed April 25, 2025, https://quest.eb.com/images/181_770492.

Pennate muscle fibres

Muscle fibres are organized at various angles depending on the muscle in question, creating an important distinction between the muscles *anatomical cross-sectional area* (ACSA) and its *physiological cross-sectional area* (PCSA). The ACSA is the area of the cross-section perpendicular to the longitudinal axis of the muscle, whereas the PCSA is the area of the cross-section perpendicular to the muscle fibres, reflecting the amount of force it can produce. *Fusiform* muscles have long fibres in parallel along its longitudinal axis, making the ACSA and PCSA equal. In contrast, *pennate* muscles have angled fibres, much like the barbs of a feather (Figure 2.6), which allows them to fit a larger number of shorter fibres within the same volume. Thus, pennate muscles can produce more force for their size, reflected by the PCSA, at the cost of contraction length. Pennate muscles are further divided into unipennate, bipennate, and multipennate muscles depending on the number of sets of similarly angled fibres.

Figure 2.6: The flexor digitorum superficialis and the third digit tendon, showing the unipennate feather-like structure, with the distal end (D) on the right side and the proximal (P) insertion on the left side. Edited and reused with permission from Matsuzawa et al (2021)[39], © 2020, https://doi.org/10.1007/s00276-020-02522-7.

2.6.2 Forearm muscles

Movement of the hand is controlled by both intrinsic and extrinsic muscles. The extrinsic muscles are larger and the prime movers of the hand and fingers, whereas most of the intrinsic muscles of the hand are responsible for more precise fine-tuning or stabilizing actions. As most of the papers in this dissertation pertains to processing EMG and modelling physiological regions of muscles in the forearm, an anatomical summary of the forearm is in order (Figure 2.7). The forearm contains 20 muscles that can be categorized into the *posterior compartment* and the *anterior compartment* (Table 2.1), separated be the interosseus membrane between the radius and the ulna[40-42]. The posterior compartment can also be further categorized into the dorsal compartment and mobile wad compartment. A distinction is also made between *deep* and *superficial* muscles, with some overlap.

Relating to movements of the hand, the posterior compartment of the forearm comprises the wrist and digit extensors, thumb abductor, and the supinator muscles, all innervated by the radial nerve. The anterior compartment comprises the wrist and digit flexors, as well as two pronator muscles, innervated by the median and ulnar nerves. Most muscle bellies are located in the proximal half of the forearm, with a couple of exceptions in the distal half.

The extensor digitorum communis (EDC) is the shared finger extensor and receives more attention than other muscles in this dissertation. Where D1-D5 denotes the digits from thumb to little finger, the EDC extends only the fingers, D2-D5. Unlike most forearm muscles, the EDC is a fused muscle with some amount of compartmentalization, where the amount of independent finger extension is limited. While there is a large amount of overlap in activity between compartments, as seen through iEMG[43], distinct regions have also been observed through both anatomical and sEMG investigations[44,45]. In this dissertation, the compartmentalization of the EDC is further explored and modelled using HDsEMG data.

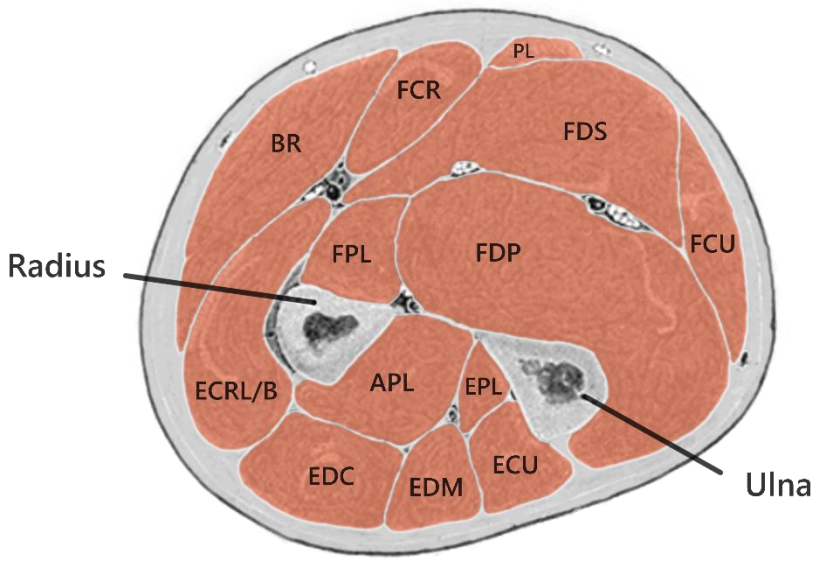

Figure 2.7: The cross-section of the middle of the forearm. Edited from Wikimedia Commons, Public domain, https://commons.wikimedia.org/wiki/File:Gray417_color.PNG.

Table 2.1: A list of the 20 forearm muscles and their main functions.

Posterior compartment	Location	Main function
ECRL Extensor carpi radialis longus	Superficial	Extends and abducts the wrist
ECRB Extensor carpi radialis brevis	Superficial	Extends and abducts the wrist
ECU Extensor carpi ulnaris	Superficial	Extends and adducts the wrist
EDC Extensor digitorum communis	Superficial	Extends the fingers (D2-D5)
EDM Extensor digiti minimi	Superficial	Extends the little finger (D5)
APL Abductor pollicis longus	Deep	Abducts the thumb (D1)
EPL Extensor pollicis longus	Deep	Extends the thumb (D1)
EPB Extensor pollicis brevis	Deep (distal)	Extends the thumb (D1)
EIP Extensor indicis proprius	Deep (distal)	Extends the index finger (D2)
- Supinator	Deep	Supinates the forearm
BR Brachioradialis	Superficial	Flexes the elbow and supinates forearm
- Anconeus	Superficial	Extends the elbow
Anterior compartment	Location	Main function
FCR Flexor carpi radialis	Superficial	Flexes and abducts the wrist
FCU Flexor carpi ulnaris	Superficial	Flexes and adducts the wrist
PL Palmaris longus	Superficial	Flexes the wrist
PT Pronator teres	Superficial	Pronates the forearm and flexes the elbow
FDS Flexor digitorum superficialis	Superficial	Flexes the fingers (D2-D5) at the proximal interphalangeal joints
FDP Flexor digitorum profundus	Deep	Flexes the fingers (D2-D5) at the distal interphalangeal joints
FPL Flexor pollicis longus	Deep	Flexes the thumb (D1)
PQ Pronator quadratus	Deep (distal)	Pronates the forearm

Chapter 3

Electromyography

3.1 Overview and origins

Electromyography (EMG) is the recorded, or the act of recording, electrical activity produced by skeletal muscles. Similar to electrocardiography (ECG) and electroencephalography (EEG), which record action potentials of the heart and brain respectively, EMG captures the action potentials of muscle fibres. EMG recordings date back to the early 20th century, where Hans Piper is generally considered to have recorded the first surface electromyogram during voluntary contractions, using a string galvanometer[29]. Although the relation between electrical activity and muscle contractions had been observed by Luigi Galvani already in the late 18th century, the practical recording of muscle-generated action potentials by Hans Piper laid the groundwork for the modern field of EMG[46].

Modern EMG makes use of computers to process and store signals, which can be broken down into three steps: detection, conditioning, and analog-to-digital (A/D) conversion [1]. *Detection* of electrophysiological signals is done using at least two electrodes placed on the skin or inside the body, measuring the potential difference between two points. In a sense, the tissue between these two points completes a circuit; electrical activity, ion currents, within this tissue drive a potential difference in the circuit, enabling the recording of one channel of EMG. *Conditioning* of the EMG signal is done to improve the quality of the recorded signal, typically using analog filters and amplifiers. *A/D-conversion* implies a discrete sampling in time of the otherwise continuous electrophysiological signals. There are many types of electrodes, components, and configurations for EMG systems. The following sections will describe different types of electrodes and setups and the impact of various factors on the recorded EMG signal.

3.2 Electrodes

There are broadly two types of EMG, based on the invasiveness of the recording, intramuscular EMG (iEMG) and surface EMG (sEMG). The former makes use of needle or wire electrodes inserted inside the muscle, whereas the latter uses electrodes placed on the skin surface above the muscle. The difference in the resulting recordings stem from the size of the electrodes' receptive fields, i.e. the detection volume, and filtering effects of the signal which depend on the tissue between the muscle fibres and the electrodes.

3.2.1 Intramuscular EMG

For intramuscular electrodes, the receptive fields vary greatly between different types[47]. The *concentric needle*, first proposed by Adrian and Bronk[48], consists of an insulated wire inside of a cannula. The potential difference is measured between the tip of the wire, which is exposed to the tissue, and the cannula. This generates a highly selective recording, where the size and shape of the exposed part of the wire affects the size of the receptive field. The precise recordings of concentric needles resulted in the first recordings of single motor units in humans[29,48]. While the needle can be readjusted until an acceptable position has been found, the downside to this electrode is the discomfort and pain which can result from the invasive nature of the recording. This is especially limiting at higher forces or during dynamic contractions, where large displacements of muscle tissue occur.

Fine-wire electrodes for EMG measurements, proposed by Basmajian in the 1960s[46,47], reduces the issues of discomfort and pain caused by a concentric needle. This type of EMG measures the potential difference between two flexible insulated wire electrodes, with uninsulated ends. The wire electrodes are placed inside a cannula which is inserted at the desired location. The ends of the wire electrodes are bent backwards, so as when the cannula is carefully removed, the wires remain in the muscle by hooking onto the tissue (Figure 3.1). While the flexibility of the wires minimizes both the pain and displacement of the electrodes during muscle contractions, they cannot be readjusted once the cannula is removed.

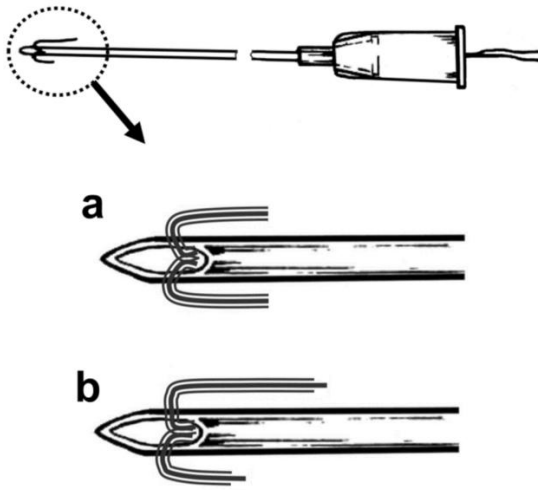

Figure 3.1: An illustration of intramuscular fine-wire electrodes and the cannula which they are inserted with. The two wires are insulated except at the ends to allow for a highly selective recording. Edited and reused with permission from Karacan and Türker (2024)[49], © 2024, https://doi.org/10.1007/s00421-024-05640-x.

3.2.2 Surface EMG

In contrast to iEMG recordings, sEMG offers a non-invasive alternative of measuring muscle activity, using electrodes placed directly on the skin above the target muscle. While this greatly improves comfort and ease of use, especially in dynamic or long-duration measurements, it also introduces several limitations. Surface electrodes detect activity from a larger volume of tissue, resulting in a broader receptive field that captures the summed activity of many motor units. As such, sEMG offers less spatial selectivity than iEMG (Figure 3.2), which can be both a feature and drawback. Furthermore, since the electrodes are placed at greater distance from target muscles, they have greater difficulty measuring the activity of deep muscles, resulting in a bias towards the activity of superficial ones. The MUAPs recorded by surface electrodes are additionally subject to low pass filtering effects, due to both the size of electrodes and the tissue between the electrodes and the muscle fibres[2,50], resulting in a blurring or smearing of the waveform.

Surface EMG signals are commonly recorded using silver/silver-chloride (Ag/AgCl) ECG electrodes (Figure 3.2), which can be both disposable and reusable. The benefit of these electrodes is that they facilitate an electrode-skin impedance that is mostly resistive and thus have a more uniform effect on the different frequency components of the signal, making them highly desirable from a signal quality perspective. In contrast, gold-plated

electrodes are more capacitive, resulting in an non-uniform electrode-skin impedance that is higher for low frequencies; the benefit of these electrodes is that they are more resistant to corrosion and thus more durable and reuseable[1]. This can make them more desirable for more expensive large grids of electrodes, which demand reusability to be affordable, despite the frequency dependence.

High-density surface EMG (HDsEMG) is an extension of sEMG achieved using grids or arrays of electrodes (Figure 3.2). These grids can vary in size, inter-electrode distance, and layout, depending on the application needs and where they are placed. Although intramuscular high-density grids are used as well[51], the non-invasive alternatives are placed on the skin, commonly using some adhesive material. By recording muscle activity from many adjacent points on the skin, HDsEMG provides a spatiotemporal recording of muscle activity, which can be conceptualized as an image, evolving in time like a movie. By covering a larger area, electrode grids make wholistic recordings of muscle activity easier. The additional spatial dimension provided by these recordings allow for more detailed analysis of MUAPs and are necessary for advanced signal processing, including motor unit decomposition and source localization, which is not feasible with individual surface electrodes. However, HDsEMG also introduces additional challenges; the amount of incoming data is much higher, placing greater demands on both the recording hardware and the processing software.

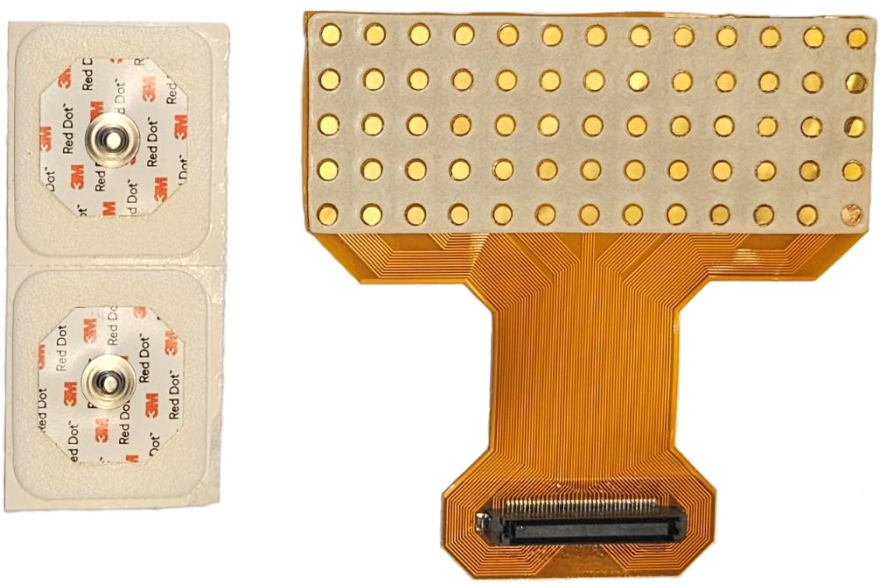

Figure 3.2: ECG electrodes (3M, left) and a HDsEMG grid (OT Bioelettronica, right).

3.3 Electrode configuration

As previously mentioned, each channel of EMG measures the potential difference between two points, requiring at least two electrodes. However, multiple channels in a system can also share one electrode, a reference electrode, between all channels. Thus, there is a distinction to be made between electrode configurations, mainly between bipolar and monopolar EMG, but also for other forms such as single differential or double differential EMG.

In *bipolar* EMG, the potential difference is measured between two identical electrodes for each channel, placed close to the muscle. This is the standard configuration for fine-wire iEMG but is also used for sEMG when the number of channels is relatively low. In this configuration, electrical activity that causes a potential increase at one electrode and a decrease at the other is amplified, whereas signals that affect both electrodes equally are attenuated. This means that the placement of the electrodes and the distance between them has a large impact on the recorded signal. In effect, the shorter the inter-electrode distance is the more local the recording will be, since there is less tissue between them to generate a strong signal. Signals generated far away from the electrodes affect them equally, known as common-mode signals, and are therefore reduced. This is often a highly desirable trait, since common-mode signals are typically generated by other muscles, i.e. crosstalk, or noise from distant sources such as powerlines interference.

A *monopolar* configuration is preferable over bipolar when a large number of channels is desired, since a shared reference electrode reduces the number of electrodes required. The reference electrode is typically placed in an electrically stable location away from muscle activity. This creates a much simpler setup at the cost of higher sensitivity to common-mode noise, due to the increased distance between the reference and the remaining electrodes.

Single differential and *double differential* configurations are commonly used in high-density surface EMG and can be understood as forms of spatial filtering applied to monopolar recordings. In single differential EMG, the potential difference is sequentially derived between two adjacent electrodes. This is similar in principle to bipolar EMG, as both electrodes are placed near the active tissue and results in a more selective signal. However, single differentials are typically derived digitally from monopolar signals and can also be conceptualized as the first spatial derivative over an electrode grid or array. Double differential EMG extends this concept by subtracting the single differential signals of two adjacent electrode pairs, i.e. the second spatial derivative (Figure 3.3). For electrode grids, this can be further extended into two dimensions, which enables a flexible selection of electrodes to include in spatial filtering. This results in various

spatial filter masks, such as the normal double differential or inverse binomial of order two[52,53]:

$$M_{SD} = \begin{pmatrix} 1 \\ -1 \end{pmatrix}, \qquad M_{DD} = \begin{pmatrix} 1 \\ -2 \\ 1 \end{pmatrix}$$

$$M_{NDD} = \begin{pmatrix} 0 & 1 & 0 \\ 1 & -4 & 1 \\ 0 & 1 & 0 \end{pmatrix}, \qquad M_{IB^2} = \begin{pmatrix} 1 & 2 & 1 \\ 2 & -12 & 2 \\ 1 & 2 & 1 \end{pmatrix}$$

In HDsEMG, these filter masks are applied for each electrode in grid, computing a two-dimensional spatial convolution that combines adjacent channels into one, forming a new signal that can increase the selectivity of the recording and aid motor unit analysis[50,54,55].

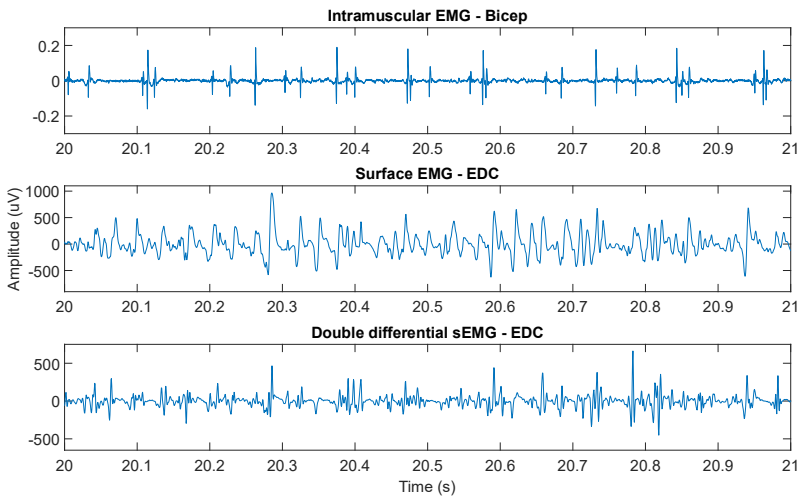

Figure 3.3: One second of iEMG (top), single channel sEMG (middle), and double differential sEMG derived from 3 electrodes (bottom). Note that the iEMG signal is from a separate recording while the sEMG signals are from the same recording.

Chapter 4

Signal processing

This chapter provides the core technical foundation of the dissertation, outlining the methods and concepts used to process and interpret EMG signals. It serves as a bridge between the raw electrophysiological signals described earlier and the broad range of applications presented later, providing the background most directly related to the work presented in the papers. The chapter begins, as all EMG analysis does, with pre-processing, covering frequency analysis and basic filters. It then broadly covers feature extraction, and describes localization in relation to spatial features, providing background to Paper II. Learning methods that make use of extracted features are introduced next, including classification and regression, with direct relevance to spatial classification and modelling performed in Paper III and IV. The chapter continues with a detailed description of signal separation, including Principal Component Analysis and Independent Component Analysis, which underpin many decomposition algorithms, including that of Paper I. Finally, it concludes with an overview of motor unit decomposition, summarizing progress in the field and the challenges that remain.

4.1. Pre-processing and filtering

4.1.1 The Fourier transform

Any time-varying signal, including EMG, can be represented in two fundamental ways: in the *time-domain*, which is how the signal is sampled and recorded, and in the *frequency-domain*, which shows how the signal's energy is distributed across different frequencies. The transformation between time- and frequency-domains is formalized by the Fourier Transform, a mathematical operation that decomposes a time-domain signal, $x[n]$, into its constituent frequencies (sine waves). In the context of EMG, which is recorded in discrete samples, the Discrete Fourier Transform (DFT) is used, efficiently computed using a Fast Fourier Transform (FFT) algorithm. The DFT, $X[k]$, over a number of samples, N, is defined as follows:

$$X[k] = \sum_{n=0}^{N-1} x[n] \cdot e^{-i2\pi kn/N}$$

The Fourier Transform is a complex-valued function with the magnitude and phase of each frequency. To visualize the frequency content of a signal in a real-valued spectrum, power spectral density (PSD) is used, calculated from the magnitude of each frequency component, discarding the phase (Figure 4.1).

$$PSD = P[k] = \frac{1}{N}|X[k]|^2$$

The frequency-domain representation is essential in EMG analysis, as it allows for the identification and isolation of frequency components associated with either muscle activity or noise[56]. For instance, lower frequencies may contain movement artifacts, and higher frequencies may consist mostly of ambient or inherent equipment noise[57-60]. Understanding the spectral content of EMG and designing proper filters is critical for any signal processing pipeline.

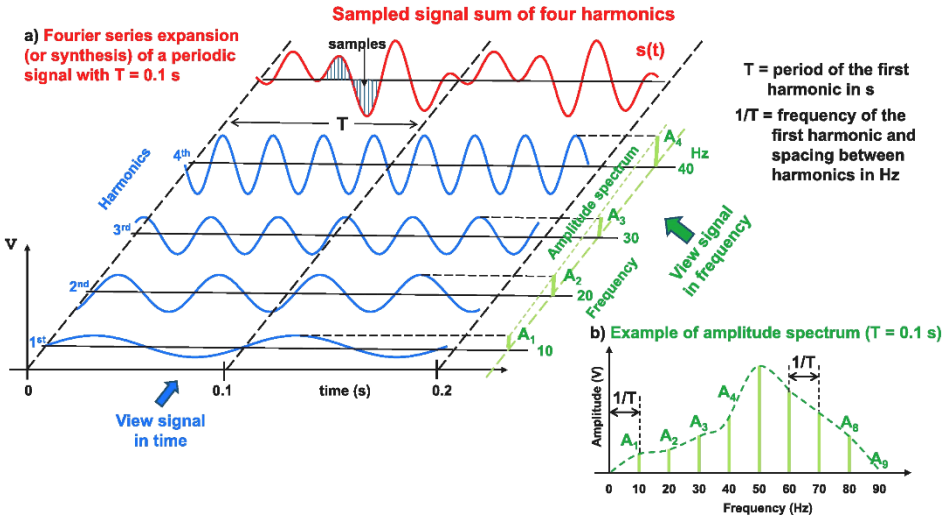

Figure 4.1: The complex valued Fourier frequencies (blue) of a sampled signal (red), and the power spectrum (green). Reused from Muceli and Merletti (2024)[56], under CC-BY-4.0.

4.1.2 Noise

EMG recordings always contain some degree of noise, artifacts, or interference, which are by definition unwanted signals. Noise can generically refer to any unwanted signal, whereas *baseline noise* more specifically refers to a consistent random signal in a recording while muscles are not contracting. Baseline noise includes thermal noise inherent to the recording system, as well as electrochemical noise introduced at the skin-electrode interface[61,62]. Artifacts refer to transient perturbations in the recording; this is most commonly the result of body movements. *Movement artifacts* are generated by changes in the skin-electrode impedance, as the skin stretches and deforms or moves relative to the electrode, and are generally below 20 Hz[63]. *Interference* is generally periodic and to some extent predictable, generated by sources both internal and external to the body. Within the body, the ECG signal can produce interference up to 100 Hz[64]. Interference from a muscle that is not a target muscle is referred to as cross-talk, which shares the same frequency spectrum as the intended EMG signal. Outside the body the main source of interference is that of electrical equipment, which can mostly be avoided by moving away from the source, and power-lines, which is generally too widespread and pervasive to avoid. Power-line interference (PLI) is centred at 50 or 60 Hz, depending on the regional power standard, and often includes its harmonic frequencies (i.e. multiples of 50 or 60 Hz). PLI is a particularly strong source of interference which

necessitates additional countermeasures; this typically includes impedance balancing and notch filters[1], but also adaptive noise cancelling[65,66], and virtual references[67].

4.1.3 Bandpass filtering

Bandpass filtering is one of the most fundamental steps in EMG signal preprocessing. It involves applying both a high-pass filter and a low-pass filter to isolate the frequency band that contains the majority of the physiological signal, while attenuating unwanted components outside this range. These two parts serve distinct but complementary purposes.

The *high-pass filter* attenuates low-frequency components, primarily targeting movement artifacts, electrode drift, and the DC component in the signal. Movement artifacts and electrode drift, caused by skin-electrode impedance changes and cable motion, typically occur below 20 Hz. Depending on the amount of noise and the application, high-pass filters used in sEMG preprocessing have many recommended cutoff frequencies, typically in the range of 5–30 Hz[58-60]. However, aggressive high-pass filtering risks attenuating genuine low-frequency components, limiting the information in the signal.

The *low-pass filter*, on the other hand, attenuates high-frequency noise and interference above the EMG signal bandwidth. In sEMG, the majority of signal power lies below 350 Hz, although some components can extend up to 500 Hz, depending on the recording. Frequencies above this range are generally considered to be noise, and the low-pass cutoff frequencies for sEMG are therefore typically set between 400–500 Hz. In contrast, intramuscular EMG (iEMG) contains higher frequency components that may exceed 1 kHz, due to its proximity to motor units which reduces the low-pass filtering effects of the tissue.

Together, these filters form a bandpass filter that preserves the EMG frequency band of interest, while attenuating high- and low-frequency noise. Bandpass filtering is crucial not only for improving signal quality but also for ensuring the effectiveness of subsequent feature extraction, decomposition, and classification algorithms, all of which rely on a clean representation of the muscle activation signal.

4.1.4 Bandstop filtering

Bandstop filters, also known as notch filters, are designed to attenuate a narrow range of frequencies while allowing others to pass largely unaffected. For EMG signals, they are most commonly used to suppress power-line interference (PLI) from electrical infrastructure, centred at 50 Hz or 60 Hz, often with harmonic components at integer

multiples of the base frequency. PLI can be many times greater than the EMG signal itself, which poses a considerable problem for investigating muscle activity. While filtering is often necessary, preventative measure should be taken to reduce PLI at the source, prior to filtering. This includes proper grounding of the EMG acquisition system and impedance balancing across electrode pairs to reduce interference pickup. PLI can also be reduced actively with a Driven Right Leg (DRL) circuit, which actively cancels common-mode noise by driving an inverted version of the detected noise back into the body. As a secondary countermeasure, however, a notch filter can very effectively suppress PLI even at high amplitudes. The downside to notch filters is that they also distort the content of the EMG signal. Since the frequency content of EMG signals stretches across 50-60 Hz, aggressive filtering may significantly attenuate important signal components, altering original signal.

4.1.5 Filter characteristics

While filtering improves signal quality by suppressing unwanted frequency components, it can also introduce unintended distortions, particularly in the temporal structure of the signal. One of the most critical artifacts of filtering is *phase delay*, or phase distortion, which occurs when different frequency components of the signal experience different time delays as they pass through the filter. To mitigate this, digital off-line filters often employ zero-phase filtering, typically by applying the filter twice, first in the forward direction from the first sample and then in the backward direction from the last sample. This compensates the introduced delays, effectively cancelling it out. However, this is not possible for analog or real-time filters. Filter performance is typically assessed by examining both the magnitude response and the phase response. The magnitude response shows how much the filter attenuates or passes each frequency, while the phase response indicates how different frequency components are shifted in time. Different filter types offer trade-offs between optimal magnitude and phase responses. The choice of filter depends on the demands of the application, particularly whether preserving waveform shape or achieving a sharp frequency cutoff is more critical.

The *Butterworth filter* is one of the most commonly used filters for EMG signals due to its maximally flat magnitude response in the passband. However, its roll-off is relatively gradual, meaning it requires a higher order to achieve steep transitions between passband and stopband. The *Chebyshev filter* offers a much steeper roll-off than the Butterworth for a given filter order; it has the best approximation to an ideal filter, at the cost of ripples in the frequency response. The *Bessel filter*, in contrast, is designed to preserve the waveform shape over time, featuring a near-linear phase response. In practice, the selection of filter type represents a trade-off between passband flatness, noise suppression, and phase preservation.

4.2 Feature extraction

The purpose of feature extraction is to simplify the raw or filtered data, by identifying the most valuable or informative properties. The entire HDsEMG input contains a lot of information that may not be meaningful or necessary for a given task. Thus, instead of analysing the entire signal directly, the most relevant features are extracted that capture and distil meaningful properties in a compact and interpretable form. The following sections describe various features of different types used in EMG analysis, including time-domain, frequency-domain, statistical, and spatial features.

4.2.1 Time-domain features

The *mean absolute value* (MAV) is the average amplitude within a given interval and is one of the most simple and robust features used for EMG signals.

$$MAV = \frac{1}{N}\sum_{n=0}^{N-1}|x[n]|$$

The *root mean square* (RMS) is an average amplitude measure similar to MAV but is directly related to the signal's power, which also makes it more sensitive to outliers.

$$RMS = \sqrt{\frac{1}{N}\sum_{n=0}^{N-1}x[n]^2}$$

Zero crossings (ZC) is the number of times the signal changes sign, which reflects the frequency content of the signal. It can be calculated any number of ways and is often combined with a threshold to avoid counting noise.

$$ZC = \sum_{n=0}^{N-2}\delta(|sgn(x[n]) - sgn(x[n+1])| > 1)$$

Slope sign changes (SSC) measures the number of times the slope of the EMG signal changes direction, reflecting the signal complexity or the degree to which high-frequency content is present.

$$SSC = \sum_{n=1}^{N-2}\delta\big((x[n] - x[n-1]) \cdot (x[n] - x[n+1]) > 0\big)$$

Waveform length (WL) is the cumulative length of the signal, providing a measure of signal complexity affected by both amplitude and frequency.

$$WL = \sum_{n=0}^{N-2} |x[n+1] - x[n]|$$

4.2.2 Frequency-domain features

The *total power* can be calculated as the sum of the power spectral density over a frequency band of interest. Total power over the entire frequency spectrum gives the energy of a signal, closely related to RMS in the time-domain. This measure is useful when the energy of interest is limited to a specific frequency band.

$$TP = \sum_{k=0}^{M-1} P[k]$$

The *mean frequency* of the PSD can be used to assess fatigue in prolonged contractions.

$$MNF = \frac{\sum_{k=0}^{M-1} f_k \cdot P[k]}{\sum_{k=0}^{M-1} P[k]}$$

The *median frequency* is similarly used in fatigue analysis, defined as f_m such that:

$$\sum_{k=0}^{m} P[k] = \frac{1}{2} \sum_{k=0}^{M-1} P[k]$$

4.2.3 Statistical features

While time- and frequency-domain features provide compact and valuable signal characteristics, they often focus on local signal properties computed on short windows (e.g. 250 ms) and are used to analyse changes in continuous data. In contrast, statistical features describe properties of the entire signal distribution and are often more time-invariant. They capture more global characteristics that quantify the shape and structure of the signal's amplitude distribution, which are essential for understanding the underlying signal-generating process. In the context of EMG, one particularly important set of statistical features is the *central moments*, which quantify key aspects of a probability distribution such as variance, skewness, and kurtosis. These moments provide a foundation for both principal and independent component analysis, critical to motor unit decomposition of HDsEMG.

The central moments of a random variable provide a formal mathematical description of the shape of its probability distribution. For a real-valued random variable Z, the r-th central moment is defined as $E\{(Z - E[Z])^r\}$. In practice, the underlying distribution of the EMG signal is unknown, and moments must be estimated from data. This is done using a finite set of signal samples yielding the sample central moment:

$$\mu_r = \frac{1}{N}\sum_{n=0}^{N-1}(x[n] - \mu)^r \approx E\{(Z - E[Z])^r\}$$

Note that central moments differ from raw moments in that they are computed about the signal's mean rather than zero. While the first raw moment is the *mean*, the first central moment is, by definition, zero. The second central moment is the *variance*, which quantifies the spread of the signal around the mean. It reflects the overall power of the signal and is directly related to both the RMS and TP (total power) features.

The third and fourth central moments are typically standardized by dividing by appropriate powers of the standard deviation in order to make them dimensionless and comparable across signals with different scales. This yields the standardized moments of skewness and kurtosis, which describe the asymmetry and tailedness of the distribution, respectively (Figure 4.2).

Skewness is computed as the third central moment divided by the cube of the standard deviation. It reflects whether the signal distribution leans toward higher or lower amplitude values, with positive skew indicating a longer right tail and negative skew a longer left tail.

$$Skewness = \frac{\mu_3}{\sigma^3}$$

Kurtosis is defined as the fourth central moment divided by the fourth power of the standard deviation, indicating how peaked or heavy-tailed the distribution is. Signals with high kurtosis more frequently exhibit large intermittent deviations, such as sharp transients or bursts.

$$Kurtosis = \frac{\mu_4}{\sigma^4}$$

These standardized higher-order moments are particularly important in statistical decomposition techniques like Independent Component Analysis, where these features are key to identifying statistically independent sources within a mixture of signals.

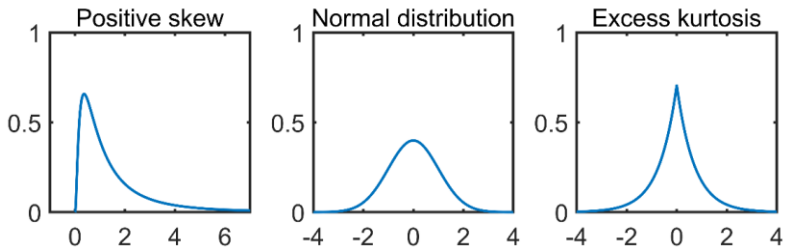

Figure 4.2: Probability distributions of the log-normal distribution (left) with positive skew, the normal distribution (middle), and the Laplace distribution with positive excess kurtosis.

4.2.4 Spatial features

The advent and widespread usage of high-density electrode grids have enabled the extraction of a new class of features, i.e. *spatial features*, which play a central role in the methods presented in this dissertation. By simultaneously recording electrical activity at multiple neighbouring sites, electrode arrays capture not only temporal variations but also the spatial distribution of the EMG signal across the skin surface. This spatial information adds a new dimension to EMG analysis, enabling the derivation of more intuitive features that reflect the underlying anatomical and physiological structures. Characterizing how signal intensity varies across space allows for physically grounded and interpretable descriptions of muscle activity.

Activation maps

While amplitude-based features such as RMS provide information about the intensity of muscle activations over time, HDsEMG enables these features to be interpreted in a spatial context. When RMS or similar measures are computed independently for each electrode in a grid, the result can be visualized as an *activation map*, or *heat map*, which is a two-dimensional representation of signal amplitude distributed across the skin surface. In practice, activation maps are typically computed over short time windows and continuously updated to display muscle activity over time. The results for each electrode are arranged according to the physical layout of the grid. Interpolation can also be applied to create a smooth surface (Figure 4.3), or fill in missing channels[68].

Activation maps capture the spatial footprint of muscle activity as projected onto the electrode array. Unlike single-channel EMG, which offers only a localized view, activation maps reveal broader patterns, such as the regions of peak intensity, asymmetries in activation, or changes in the distribution over time[69-73]. Beyond visualization, activation maps serve as a foundation for other spatial features, including

the centre of activity and spread of activity, as well as direct input for convolutional neural networks[74,75]. They have also been used to directly estimate muscle fibre conduction velocity and muscle fibre orientation[76].

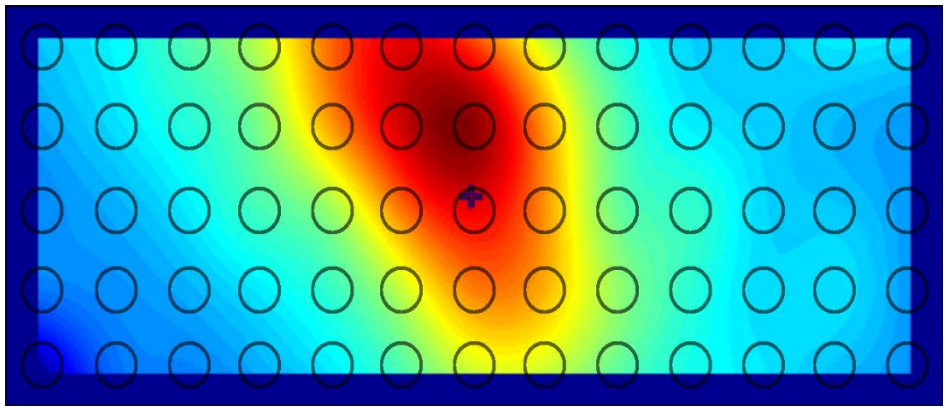

Figure 4.3: An activation map of a 5-by-13 HDsEMG grid during index finger extension.

Waveform distribution maps

While activation maps provide a scalar summary of signal amplitude at each electrode over a given time window, longer waveforms can be visualized in a similar manner as well. In this case, a short window of samples (e.g. 50 ms) is extracted and plotted for each electrode at its corresponding grid location (Figure 4.4), forming a *spatiotemporal map* of electrical activity[77].

These waveform distribution maps reveal how the shape and timing of the signal vary across space. Measuring the difference in timing of electrical activity along the direction of muscle fibres captures the propagation of motor unit action potentials, from which valuable properties such as *muscle fibre conduction velocity* can be derived. Waveform distribution maps are commonly used in motor unit decomposition to visualize the motor unit potential distribution, typically derived using spike-triggered averaging (STA) with identified motor unit spike trains; they are, however, equally applicable to non-decomposed signals. In the context of this dissertation, these waveform distributions are used not only for visualization, but also as the basis for iterative decomposition, localization of both decomposed and non-decomposed EMG signals, and subsequent modelling of muscle activity.

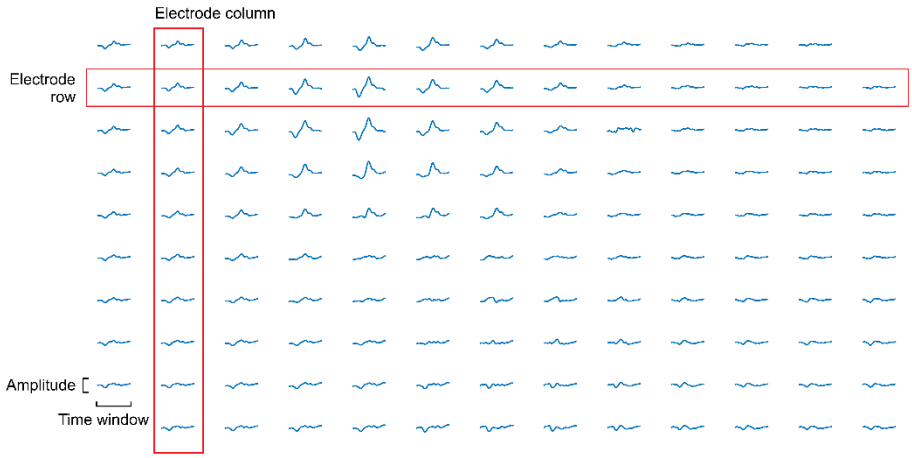

Figure 4.4: A waveform distribution map of a motor unit action potential derived using spike-triggered averaging.

Centre of Activity

The centre of activity (CoA) provides a compact summary of the spatial distribution of EMG intensity across the electrode grid. It represents the weighted average location of signal amplitude, effectively identifying the "centre of mass" of muscle activation within the recording window[70,78,79]. To compute the CoA, a scalar amplitude measure, such as the RMS value, is first calculated for each electrode over a short time window, i.e. generating an activation map. The spatial coordinates of the electrodes, (x_i, y_i), are then weighted by their corresponding amplitude values, A_i.

$$x_{CoA} = \frac{\sum_i A_i x_i}{\sum_i A_i}, \quad y_{CoA} = \frac{\sum_i A_i y_i}{\sum_i A_i}$$

This results in a single point that indicates where the majority of activity is concentrated across the grid, useful for tracking changes in muscle activity over time or comparing activation patterns across tasks or subjects.

Spread of Activity

Following the centre of activity as a spatial analogue to the signal mean, the spread of activity represents the next logical feature, as a spatial analogue to the signal variance. While the centre of activity quantifies where the EMG signal is concentrated on the electrode grid, the spread of activity captures whether it is tightly localized or broadly distributed.

Although the concept of spatial dispersion has been visualized and qualitatively assessed through activation maps, a formalized feature to quantify it has not been widely adopted. A potential spread of activity metric can, however, be conceptualized as the weighted spatial variance of signal amplitude across the electrode grid.

$$SoA = \sigma_{x,y}^2 = \frac{1}{\sum_i A_i} \sum_i A_i \left[(x_i - x_{CoA})^2 + (y_i - y_{CoA})^2 \right]$$

This feature is a spatial analogue of the weighted sample variance, where signal amplitudes serve as weights over the spatial coordinates. The result is a scalar value representing the overall spatial spread of activity across the electrode grid. While overall spread of activity is not a common feature on its own, spread along a specific axis is central to source localization techniques that triangulate the origin of motor unit action potentials.

Localization

In the context of this dissertation, unless otherwise stated, localization of EMG signals refers to estimating or approximating the 3D position of a signal source within a muscle, rather than a position projected onto the electrode grid at the skin surface. In contrast to the centre of activity, providing a weighted average location on the surface, 3D localization methods infer the subsurface origin of electrical activity, extending the spatial interpretation from two dimension into three. Finite element models have long been explored to solve this problem[80-83], but they tend to be computationally heavy. The simpler approach is to make use of the surface signal as presented by waveform distribution maps and inferring the depth of the motor unit source from the properties of the distribution alongside an analytical volume conductor model[84-87].

Roeleveld et al presented a method for estimating motor unit depth by measuring the spread of the MUAP amplitude decay perpendicular to the muscle fibre direction[84]. Using a linear array of surface EMG and intramuscular scanning EMG, they identified a number of motor units at varying depths and obtained their waveform distributions along the surface array from spike-triggered averaging. They managed to characterize the relation between the depth of motor units and features of the waveform distribution. Since superficial motor units are disproportionately close to some electrodes over others, the amplitude decays rapidly from its peak value at the electrode directly above the motor unit to the more distant electrodes. In contrast, deeper motor units have a more uniform distance to each electrode, resulting in a more uniform, wider, amplitude distribution across the electrode array. Specifically, they estimated the full width at half-maximum (FWHM) of the amplitudes of the waveform distribution (Figure 4.5)[84].

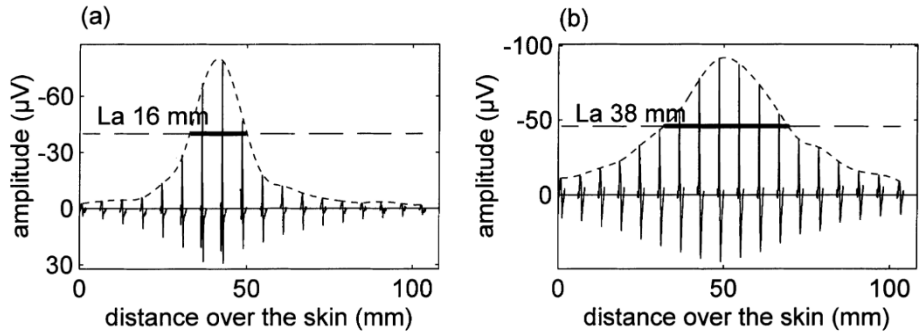

Figure 4.5: The waveform distribution of a linear array width the full width at half-maximum (FWHM) for a superficial (left) and deep (right) motor unit. The superficial motor unit has a rapid amplitude decay and thus a small FWHM, whereas the deep motor unit has a slow decay and a large FWHM. Reused with permission from Roeleveld et al (1997)[84], © 2003, https://doi.org/10.1046/j.1365-201X.1997.00247.x.

The amplitude decay, characterized by the FWHM, can then be modelled as signal attenuation which increases with distance from the motor unit source. The relation between the attenuation power and motor unit depth is described in an analytical volume conductor model[84]. A multitude of volume conductor models have also been explored and proposed for HDsEMG, with multiple layers and inhomogeneities[85,88-93]. While some alternatives to solve this inverse problem have been explored[94-96], the association between the FWHM and depth described by Roeleveld et al is the core stepping stone for the source localization method used in this dissertation and introduced in Paper II.

4.3 Feature-based learning methods

Once features have been extracted from EMG signals, they can be used as inputs to machine learning models or algorithms for interpreting muscle activity. Models that learn the relationship between input features and target outputs from labelled data are categorized as supervised learning methods. This broadly covers two applications: classification and regression.

4.3.1 Classification

Classification methods attempt to assign the input features, represented as feature vectors, to one or more discrete classes. In the context of EMG, classification answers questions such as which muscle is active, or which gesture is performed. Papers III and IV in this dissertation focus on spatial classification within a 3D muscle model, but this section provides general context by briefly describing common alternative approaches.

K-nearest neighbours (k-NN) is one of the simplest classification algorithms. It assigns a class label to a new input based on the majority class among its k closest neighbours in the feature space. Rather than learning an explicit model, k-NN simply stores all training data in memory and performs classification through direct comparison. While intuitive and easy to implement, it scales poorly in high-dimensional spaces.

Linear discriminant analysis (LDA) separates data into distinct classes by finding a linear combination of features that maximizes separability[97]. It assumes that each class follows a Gaussian distribution with a shared covariance matrix, and projects the data onto a lower-dimensional space that maximizes the between-class variance while minimizing within-class variance. LDA is computationally efficient and commonly in EMG classification due to its simplicity and fast inference.

Support vector machines (SVM) aim to find a decision boundary that maximizes the margin between classes in the feature space[98]. In the linear case, the boundary is a hyperplane, while non-linear separations can be achieved using kernel functions that map the data into higher-dimensional spaces. SVMs are robust to overfitting and often perform well on small-to-moderate datasets, due to their emphasis on margin maximization and their reliance on only a sparse set of support vectors, resulting in fewer effective parameters compared to high-capacity models like neural networks.

Artificial neural networks are highly flexible models capable of learning complex non-linear relationships between inputs features and class labels. They consist of multiple layers of interconnected nodes, resembling neurons, each applying a non-linear transformation to its input. Neural networks are conceptually different in that they are

typically trained layer-by-layer, through an iterative optimization process called backpropagation. While neural networks can act as powerful function approximators, their large number of parameters often requires substantial data to train effectively. They are also prone to overfitting, necessitating regularization techniques to ensure generalizability.

In this dissertation, *spatial classification* based on 3D modelling of muscle volumes is introduced in Paper III. This approach leverages the spatial features derived from waveform distribution maps to first model muscle regions as volume functions and then perform spatial classification of new points within the model. Here, the feature vector becomes the Cartesian coordinates of a given 3D position, and a unique ellipsoid volume function is used to represent each muscle. These functions then serve as distance metrics to the volume centre, used to assign each new observation to the closest muscle representation. It is conceptually simple and somewhat similar to k-NN, where instead $k = 1$ and the distance metric varies between classes to account for varying distributions.

4.3.2 Regression

Although not the explicit focus of the work in this dissertation, regression is widely used in HDsEMG applications. It is also closely related to some modern decomposition algorithms, and thus worth mentioning.

Linear regression is one of the simplest and most widely used methods for modelling the relationship between a set of input features and a continuous output variable. In the context of EMG, it is often applied to estimate muscle force or joint torque. The model assumes a linear relationship between the input, $\boldsymbol{X}$, and the predicted output, $\hat{\boldsymbol{y}}$, determined by a vector of learned weights, $\boldsymbol{w}$.

$$\hat{\boldsymbol{y}} = \boldsymbol{w}^T \boldsymbol{X}$$

The optimal weights are typically found by minimizing the mean squared error between the predicted output and ground truth, $\boldsymbol{y}$:

$$min\|\boldsymbol{y} - \hat{\boldsymbol{y}}\|^2 = \sum_{n=1}^{N} (y[n] - \boldsymbol{w}^T \boldsymbol{x}[n])^2$$

This minimization problem has the optimal solution:

$$\boldsymbol{w} = (\boldsymbol{X}^T \boldsymbol{X})^{-1} \boldsymbol{X}^T \boldsymbol{y}$$

It is worth noting that this solution is mathematically equivalent to estimating the Wiener filter, commonly described in filter theory[99] and central to some motor unit

decomposition techniques using lower-order statistics. It is expressed as the input autocorrelation, $\boldsymbol{R_{xx}}$, and the input-output cross-correlation, $\boldsymbol{r_{xy}}$:

$$\boldsymbol{w} = \boldsymbol{R_{xx}^{-1}} \boldsymbol{r_{xy}}$$

$$\boldsymbol{R_{xx}} = E\{\boldsymbol{X^T X}\}, \quad \boldsymbol{r_{xy}} = E\{\boldsymbol{X^T y}\}$$

4.4 Unsupervised learning methods

4.4.1 Principal component analysis

Principal Component Analysis (PCA) is a statistical technique commonly used to reduce the dimensionality of a dataset while preserving as much variance as possible. In the context of processing HDsEMG signals, PCA can simplify high-dimensional data by identifying orthogonal directions, or basis vectors, along which the data has the highest variance.

If each channel in a high-density recording represents a dimension in a high-dimensional space, then PCA performs a linear transformation, or rotation, of this space to align the new coordinate system with the directions of maximal variance. The first principal component is the direction (a vector) along which the data vary most. It is a *linear combination* of the original channels, meaning that each new component is formed by scaling each input channel by a weight and summing the result. Each subsequent component is chosen to capture as much of the remaining variance as possible while staying orthogonal to the previous components. The result is a set of components ordered by how much variance they explain.

Mathematically, PCA involves computing the *covariance matrix*, $\boldsymbol{R}$, of the data matrix, $\boldsymbol{x}$, after removing the mean across channels (centring the data). The principal components are the *eigenvectors* of this matrix, and the amount of variance explained by each component is given by its associated *eigenvalue*.

$$\boldsymbol{R} = \frac{1}{N} \boldsymbol{X^T X}, \quad \boldsymbol{R e_i} = \lambda_i \boldsymbol{e_i}$$

where $\boldsymbol{e_i}$ is the i-th principal direction and λ_i the corresponding eigenvalue representing the variance along that component. PCA serves multiple purposes in HDsEMG analysis, most commonly as a preprocessing step for other methods. It is used to reduce size of large data matrices by retaining only the top principal components that account for most of the signal structure, referred to as *dimensionality reduction*. In the same vein, it is used for *noise reduction*, by discarding low-variance components often dominated by noise. Additionally, PCA is used to perform *whitening* (or *sphering*), which is the process of

decorrelating signals and normalizing their variances. By removing the influence of lower-order statistics, i.e. the mean and variance, PCA prepares the data for Independent Component Analysis (ICA), which leverages higher-order statistics such as skewness and kurtosis to identify underlying sources that are statistically independent. Whitening is formulated as:

$$\boldsymbol{Z} = \boldsymbol{V}\boldsymbol{X}$$

$$\boldsymbol{V} = \boldsymbol{E}\boldsymbol{D}^{-1/2}\boldsymbol{E}^{T}$$

Where $\boldsymbol{Z}$ is the whitened data matrix and $\boldsymbol{V}$ is the whitening matrix, produced by the matrix of unit-norm eigenvectors, $\boldsymbol{E}$, and a diagonal matrix of their eigenvalues, $\boldsymbol{D}$, from the previously defined covariance matrix.

4.4.2 Independent component analysis

While PCA transforms the data into uncorrelated components, this is not enough to separate independent components, such as individual motor unit signals. Independent Component Analysis (ICA), however, seeks a linear transformation based on higher-order statistics which do reflect independence, making it a powerful method for *blind source separation* (BSS) tasks[100-102]. Blind source separation refers to the task of separating a set of mixed signals into their original source components without prior knowledge of how they were combined. The task is exemplified by the "cocktail party problem", where multiple people speak simultaneously in a room, and several microphones record overlapping audio signals. ICA attempts to unmix these recordings and isolate each individual voice. In the context of HDsEMG, the recordings from the electrode grid are mixtures of motor unit sources, and ICA seeks a de-mixing transform to recover statistically independent sources, based solely on the observed surface signals.

$$\boldsymbol{y} = \boldsymbol{w}^{T}\boldsymbol{Z}$$

Where the de-mixing vector, $\boldsymbol{w}$, is the linear combination applied to the centred and whitened data matrix, $\boldsymbol{Z}$, producing an independent source, $\boldsymbol{y}$.

Non-gaussianity and entropy

The key assumption in ICA is that the observed signals are linear mixtures of statistically independent sources with *non-Gaussian* distributions. ICA works because of a fundamental statistical principle: the Central Limit Theorem, which states that the sum (or mixture) of independent random variables tends toward a Gaussian distribution, even if the original variables themselves are not Gaussian. ICA leverages the inverted logic;

if the underlying sources are individually less Gaussian than their mixture, then maximizing non-Gaussianity will identify sources that are maximally independent.

To measure and maximize non-Gaussianity, ICA algorithms rely on higher-order statistical moments such as kurtosis (the fourth central moment) and skewness (the third). This is because Gaussian distributions exhibit zero skewness and zero excess kurtosis, from which structured sources may deviate. In information-theoretic terms, Gaussian variables carry the least information and have the highest entropy among variables of equal variance; whereas independent sources are typically sparse or structured and thus carry more information. ICA is often theoretically formulated using negative entropy (negentropy), a measure of how far a distribution is from a Gaussian.

$$J(\boldsymbol{y}) = H(\boldsymbol{y}_{gauss}) - H(\boldsymbol{y})$$

Although negentropy provides a powerful theoretical measure of non-Gaussianity, it is not easily computed for arbitrary distributions. Negentropy can, however, be approximated using higher-order moments[100].

$$J(\boldsymbol{y}) \approx \frac{1}{12} skew(\boldsymbol{y})^2 + \frac{1}{48}[kurt(\boldsymbol{y}) - 3]^2$$

Note here that a Gaussian distribution has no skew and a kurtosis of 3; by subtracting 3 from kurtosis, we get *excess kurtosis*, which is thus relative to the Gaussian distribution.

Contrast functions

In practice, the approximation using higher-order moments can be used as is, but it runs into instability as these polynomial functions are sensitive to outlier samples. A pair of non-polynomial *contrast functions*, G^1 and G^2, which reflect skewness and kurtosis are commonly used instead:

$$J(\boldsymbol{y}) \approx k_1(E\{G^1(\boldsymbol{y})\})^2 + k_2\big(E\{G^2(\boldsymbol{y})\} - E\{G^2(\boldsymbol{y}_{gauss})\}\big)^2$$

If one where to choose $G^1(\boldsymbol{y}) = \boldsymbol{y}^3$ and $G^2(\boldsymbol{y}) = \boldsymbol{y}^4$, we return to the prior approximation of negentropy. More practical choices that are robust to outliers, would be:

$$G^1(\boldsymbol{y}) = \boldsymbol{y} \exp(-\boldsymbol{y}^2/2)$$

$$G^2(\boldsymbol{y}) = \exp(-\boldsymbol{y}^2/2)$$

Any number of contrast functions that reflect skewness and kurtosis can be used; the goal remains the same: to maximize $J(\boldsymbol{y})$. This optimization problem is often further simplified, by using only one contrast function and dropping the constants.

$$J(\boldsymbol{y}) \propto \left(E\{G^2(\boldsymbol{y})\} - E\{G^2(\boldsymbol{y}_{gauss})\}\right)^2$$

From here, any optimization method can be used, such as gradient descent, which would find stationary points of the derivate of the function. One of the most widely used methods, however, is the *FastICA algorithm*, due to its fast convergence properties.

FastICA

The FastICA algorithm is a fixed-point iteration algorithm which converges much faster than traditional gradient descent[100,101]. It is derived using Newton's method, containing the first and second derivatives, g and g', of the original contrast function, G^2. After inserting $\boldsymbol{y} = \boldsymbol{w}^T\boldsymbol{Z}$, the iterative update for the de-mixing vector in FastICA is:

$$\boldsymbol{w} \leftarrow \boldsymbol{E}\{\boldsymbol{Z}g(\boldsymbol{w}^T\boldsymbol{Z})\} - \boldsymbol{E}\{g'(\boldsymbol{w}^T\boldsymbol{Z})\}\boldsymbol{w}$$

$$\boldsymbol{w} \leftarrow \boldsymbol{w}/\|\boldsymbol{w}\|$$

Where the de-mixing vector is normalized in each iteration. This iteration then continues until changes to the de-mixing vector are very small, set by some threshold, or reaches a chosen maximum number of iterations.

$$\boldsymbol{y} = \boldsymbol{w}_{final}\boldsymbol{Z}$$

The final output is an estimated independent source component. Identifying multiple sources can be done either one at a time or simultaneously in each iteration; both cases require an orthogonalization step for the different de-mixing vectors. The goal is to prevent each de-mixing vector from converging to the same values. Thus, the overlap between vectors, their dot product, is removed in each iteration, typically applied before normalization. Removing the overlap with the previously identified de-mixing vectors, $\boldsymbol{w}_j$, from the current de-mixing vector, $\boldsymbol{w}_p$, is referred to as *deflationary* orthogonalization, used when estimating sources one at a time:

$$\boldsymbol{w}_p \leftarrow \boldsymbol{w}_p - \sum_{j=1}^{p-1}(\boldsymbol{w}_p^T\boldsymbol{w}_j)\boldsymbol{w}_j$$

Symmetric orthogonalization refers to an even, or unbiased, decorrelation between multiple de-mixing vectors, combined in the de-mixing matrix $\boldsymbol{W}$, used when estimating multiple sources simultaneously:

$$\boldsymbol{W} \leftarrow (\boldsymbol{W}\boldsymbol{W}^T)^{-1/2}\boldsymbol{W}$$

In the context of HDsEMG, ICA works for motor unit decomposition because motor unit signals are very sparse. A sparse signal contains mostly zeros, with concentrated bursts of activity, which results in high kurtosis. A combination of two motor unit spike trains has lower kurtosis (and is less sparse), as their common distribution is closer to a Gaussian distribution due to the Central Limit Theorem. Furthermore, ICA cannot "go too far" and separate individual MUAPs from the same motor unit (which would create an even sparser signal). This is because MUAPs from the same motor unit tend to be almost identical, and the de-mixing vector is applied uniformly across the HDsEMG data. The result is that for a linear combination of channels, it is maximally kurtotic, or sparse, for *individual* motor units with their *full spike train* intact.

4.5 Motor unit decomposition

4.5.1 Development of motor unit decomposition

The decomposition of surface EMG into individual motor unit spike trains has undergone a substantial evolution, with a range of computational methods and models from different theoretical backgrounds. Early approaches relied on template matching techniques, originally developed for intramuscular EMG, where action potential waveforms could be cleanly isolated and clustered based on shape similarity[103-105], and with software applications such as EMGLAB[106-108] and DQEMG[109-112]. When applied to sEMG, however, these methods faced significant limitations due to the signal complexity, with overlapping MUAPs and smearing due to the inherent low pass filtering effects[113-118].

The introduction of HDsEMG enabled a new class of methods based on BSS. These approaches treat the EMG signal as an unknown mixture of sources, aiming to unmix them using statistical criteria. In this context, ICA methods, such as FastICA and JADE, became prominent and were successful in decomposing a small number of motor units[119-124].

However, classical ICA assumes instantaneous linear mixing and does not account for the temporal structure in real signals, as if all samples were recorded simultaneously without order. To make better use of this temporal information, the model underlying EMG decomposition methods shifted to a finite impulse response (FIR) filter model:

$$x_i[n] = \sum_{j=1}^{J} \sum_{l=0}^{L-1} a_{ij}[l] s_j[n-l]$$

Where $x_i[n]$ is the i-th EMG channel, $s_j[n-l]$ is the spike train (impulses) of the j-th motor unit, $a_{ij}[l]$ is the action potential (impulse response) of the j-th motor unit at channel i, where L is the length of the action potential, and J is the number of active motor units. This gave rise to the Convolution Kernel Compensation (CKC) framework[125-127], where the goal instead is to reverse (compensate) the impulse responses and recover the underlying spike trains directly. The impulse response is compensated by iteratively estimating and updating an optimal filter, which is based on second-order statistics rather than higher-order statistics. CKC has been applied and improved upon extensively[128,129], combined with clustering algorithms[130,131], peel-off strategies[132,133], neural networks[134,135], real-time adaptation[136,137], and dynamic contractions[138,139].

The convolutive framework in CKC, however, can always be reformulated, or linearized, in ordinary ICA as well[100], which was done by Chen and Zhou[140] and Negro et al[141] for HDsEMG. The reformulation consists of extending the original dataset with delayed copies as new channels. Thus, the de-mixing vector becomes longer, and the linear combination channels now spans multiple samples in time. Chen and Zhou applied a batch estimation of sources using FastICA with symmetric orthogonalization, and a peel-off strategy to remove the identified sources from the dataset, allowing subsequent iterations to reveal new motor unit sources[140,142]. Negro et al applied FastICA with deflationary orthogonalization combined with further refinements to the source estimates proposed in the CKC framework[126,141]. These convolutive FastICA approaches are built upon in the first paper included in this dissertation[143], by making use of a peel-off strategy with spike-triggered averaging (STA) and compression. The STA approach to peel-off has since then also been used in combination with CKC[144]. Alternative real-time decomposition methods have been proposed as well[145-147]. But perhaps more significantly, open-source tools for motor unit decomposition of HDsEMG have recently been developed[148,149], and tutorials have been published[150], which greatly lower the entry barrier and increase the collaborative potential of the field.

4.5.2 Issues affecting motor unit decomposition

There are, however, a few hurdles to overcome in motor unit decomposition which may not be present in other source separation tasks. These range from necessary reliability measures to characteristics of muscle contractions and the foundation of motor units as signal sources.

Reliability measures

In most iterative decomposition methods, the most prominent motor units are found first. In the subsequent iterations, motor units are increasingly hidden behind baseline noise or inseparable overlaps. Inevitably, there is a point where the source output may no longer represent a motor unit spike train. Thus, it is essential to assess the reliability of estimated motor unit sources. This is typically done with some measure reflecting the signal-to-noise ratio of the source, such as the silhouette[141] or pulse-to-noise ratio[151]. By some determined threshold, poor estimates are then either discarded or improved upon in some manner. The optimal choice of threshold may be difficult to assess, and different measures may not be comparable due to potential transformations applied in the calculation, as argued by Chen and Zhou in a recent review[152].

Due to the uncertainty in motor unit decomposition, many validation studies have been conducted to gauge decomposition reliability. An established validation approach on experimental data is the simultaneous recording of iEMG and HDsEMG, with subsequent comparison of decomposition results for motor units identified in common[153-155]. Another approach is the comparison between methods, to assess their rate of agreement or matching rate[156,157], or to decompose synthetic data[151].

Number of motor units

Decomposition reliability extends from the accuracy of individual motor unit estimates to the entire population of estimated motor units. The number of decomposed motor units that are reported have drastically increased over the years. While decomposition algorithms continually improve, reports might be exaggerated[152]. An inflated motor unit count could manifest from lower acceptance thresholds for individual motor units, which can vary significantly. Additionally, a large number of repetitive motor units may also affect reported results. The same motor unit could be counted more than once, either through partial initial decomposition and subsequent identification of residual firings, or through duplicate estimates with identical firing instances.

Duplicate estimates

Duplicate estimates occur due to inherent limitation in the methods used for the motor unit decomposition task. Typically, a source estimate in motor unit decomposition reflects the instances of MUAP discharges, but not the entire motor unit signal. This is partly because the motor unit signal is not a single point source, rather it is a cylinder source, where the signal is spread out in both space and time along the muscle fibre. The MUAP cannot be represented as a single one-dimensional signal, as it varies in two dimensions. Thus, motor unit decomposition is typically focused on identifying the motor unit spike train instead of the MUAP waveform, with the MUAPs represented in waveform distribution maps after decomposition. The issue, in practice, is that two de-mixing vectors can converge on two "versions" of the same motor unit, even with an orthogonalization step, resulting in duplicate motor unit estimates which need to be dealt with. Thus, in addition to reliability measures of the source output, a step for removing duplicate estimates is critical as well[152].

Chapter 5

Applications of electromyography

Electromyography has found a wide range of applications across research, clinical, and commercial domains. These applications can be broadly divided into three main areas, each defined by the functional state of the individual and the role EMG plays in supporting, restoring, or enhancing motor function. The first category involves *rehabilitation and clinical assessment*, where individuals typically have an intact limb with impaired function due to neuromuscular disorders or injuries that disrupt normal muscle control. In this context, EMG is primarily used as a diagnostic or monitoring tool, to assess neuromuscular health, quantify recovery, or guide therapeutic interventions. The second major category is *prosthetic control*, aimed at individuals who have lost parts of or entire limbs. In these cases, EMG is used to interpret residual muscle activity to drive the control of prosthetic devices. Because the original muscles may be absent or anatomically displaced, this places unique demands on EMG acquisition and processing methods for every individual. The final set of applications relates to *human-machine interfaces* for individuals without impairments. Here, EMG is leveraged not for recovery or compensation, but as a means to enhance or extend human capabilities. In these scenarios, ranging from gesture-based control of devices and exoskeletons to interactions with virtual and augmented reality, EMG acts as visceral interface between the body and external technology.

5.1 Rehabilitation and clinical assessment

The potential clinical value of sEMG is extensive as described in the scientific literature, but it is contrasted with a limited degree of clinical adoption, as a consequence of a range of cultural, educational, and technical barriers[3-5]. The utility of sEMG spans many pathologies and injuries, particularly those involving altered motor control. With regards to muscle activation patterns, sEMG is used to assess muscle coordination, commonly used in gait analysis where healthy and pathological activations patterns can be distinguished[158]. It extends to both neurological impairments, such as stroke[159], cerebral palsy[159,160], and amyotrophic lateral sclerosis[161]; and orthopedic impairments, such as back pain[162,163], osteoarthritis[164], and anterior cruciate ligament injury[165]. Moreover, sEMG is also used to assess muscle synergies, load sharing, and fatigue[3,166-169], as well as monitoring alterations in posture control[170-172]. Localization of muscle innervation zones from sEMG have been used to guide injections of botulinum toxin in treatments of spasticity from cerebral palsy and stroke[173-175]. There are also more active applications, where sEMG is used in interactive robot-assisted therapy[176] and as biofeedback to enhance treatment[177]. Across applications in rehabilitation and assessment, motor unit decomposition is especially relevant; it allows for the exploration of, e.g., motor unit organization and synchronization during recovery, with the potential to provide more extensive assessment capabilities.

Despite this wide breadth of applications, going far beyond the short list mentioned here, the clinical use of sEMG remains limited. The barriers to widespread adoption include a cultural reluctance among clinicians, lack of technical competence and education, communication gaps, and economic limitations[3]. Overcoming these barriers require greater interdisciplinary collaboration and simple user-friendly systems and processing algorithms.

5.2 Prosthetic control

While prosthetic control falls under the definition of HMIs, it is worth making a distinction between prosthetics and generic HMIs, due to the unique challenges they face. There are three general categories of upper limb prosthetic devices: passive, body-powered, and electrically powered prosthetics[6-8]. Passive prosthetics do not move and are mainly adopted for their aesthetics and comfort[178]; they provide limited, although still significant, function, often with a highly customized task in mind[6]. Body-powered prosthetics use a harness system and a cable mechanism, allowing the user to control the device with the movement of other body parts; they provide significant functional value, durability, and secondary proprioceptive feedback to the user[6,179]. Electrically powered prosthetics are most commonly controlled through EMG signals; they provide better

speed and grip force compared to the alternatives, as well as a more pleasing appearance[6]. However, despite considerable advances in hardware, the sustained use of active upper limb prosthetics is limited, with high rejection rates for myoelectric-controlled devices[8,180,181].

Unlike applications in clinical assessment, where signals are interpreted by trained professionals, EMG-based prosthetic control requires the system to autonomously interpret intent and execute movement in real time. Thus, there is a high demand on both robust signal acquisition and processing, as well as a stable long-term interface. The degree of individual adaptation is vast, as residual muscles may be displaced or weakened. Furthermore, users must learn to generate repeatable EMG patterns while receiving little or no sensory feedback, and if the control system is too complex, it placed a high cognitive load or burden on the user, resulting in frustrations and ultimately rejection of the prosthesis[182,183].

5.3 Human-machine interfaces

Human-machine interfaces is a broader umbrella term for any form of aid that integrates people with technology, in order to augment or supplement human capabilities. Here, we refer to generic HMIs as technology that is applicable to anyone, not just patients, meaning the potential user base is far greater and perhaps more commercially lucrative. In contrast to clinical applications, where each patient may pose unique challenges requiring individual technical solutions, generic HMIs aim for cross-user generalizability with minimal individual training.

While this dissertation focuses on myoelectric control signals, HMIs cover a diverse set of sensing modalities, with unique advantages and drawbacks. Inertial and bending sensors, such as IMUs (inertial measurement units) and flex sensor, incorporated into data gloves[184] can provide robust movement information, for e.g. gesture recognition. However, they rely entirely on physical motion, providing no information on muscle force or isometric contractions, and interfere with the hands they measure. Vision-based systems, such as Kinect[185] or Leap Motion[186], can also reliably track hands for gesture recognition, but rely on external cameras, limiting portability. Ultrasound can be used to provide information on deep muscles with high spatial resolution. However, typical clinical transducers are bulky and susceptible to motion artifacts[187]. The appeal of sEMG-based HMIs is that even very subtle signals from low-effort or isometric muscle contractions can be used; and contra image processing, HDsEMG deals with fewer data channels which reduces the computational burden[9,10,188,189]. Furthermore, EMG precedes the muscle contraction; this reduced latency could be critical in real-time processing and ultimately increase the natural feel of HMIs.

Beyond prosthetic control, applications for HMIs are wide-ranging and rapidly evolving. A major domain for sEMG-based HMIs is communication, including sign language recognition[11,190,191] and speller systems[12]. Adjacent to prosthetics is the control of robots in unsafe of uncertain environments[192]. sEMG has also been used in map navigation[193], to enhance game interactions[194], and evoke force exertion in virtual reality environments[195]; even specialized training programs have been explored, for improving hand hygiene[196] or gestures from sports referees[197].

While the number of potential applications is vast, sEMG-based HMIs have yet to see widespread adoption. To achieve the lofty promises HMI, as often described in popular science, the systems need robustness, intuitive control, seamless integration, and cross-user generalization. Solving these challenges could ultimately move sEMG-based HMIs beyond research prototypes, to become everyday tools and natural extensions of the human body.

Part II

Included papers

Chapter 6

Summary of papers

This chapter comprises brief summaries of the papers in this dissertation, including three published journal papers and one unpublished manuscript. All papers relate to methods of processing HDsEMG data in various ways, with a clear shift in direction for Papers III and IV. Paper I presents a novel algorithm for motor unit decomposition which outperformed a state-of-the-art method based on the similar underlying signal separation theory. Paper II introduces a motor unit localization method, validated with simultaneous iEMG, and demonstrates the differences in the spatial distribution of active motor units between different actions. Paper III presents a new approach to processing HDsEMG, visualizing muscle activity and modelling muscles using volume representations, with substantial statistical robustness compared to approaches reliant on motor unit decomposition. Paper IV demonstrates far-reaching potential and generalizability in gesture classification using a model with volume representations of muscle regions.

Paper I:
Compressed spike-triggered averaging in iterative decomposition of surface EMG

This paper proposes a method for automatic decomposition of HDsEMG signals into motor unit spike trains using a peel-off approach combined with FastICA. The new method employs spike-triggered averaging compressed via PCA to reduce noise in each iteration, and high-dimensional density-based clustering to improve spike train estimation accuracy. Additionally, a reliability measure based on source variance before and after peel-off is introduced to identify and discard unreliable motor unit estimates.

Validation against synthetic data demonstrated superior performance over a state-of-the-art algorithm that used an established deflationary FastICA approach, especially at lower signal-to-noise ratios, while maintaining computational efficiency. These enhancements represent further progress towards the complete and accurate extraction of motor unit activity from HDsEMG recordings.

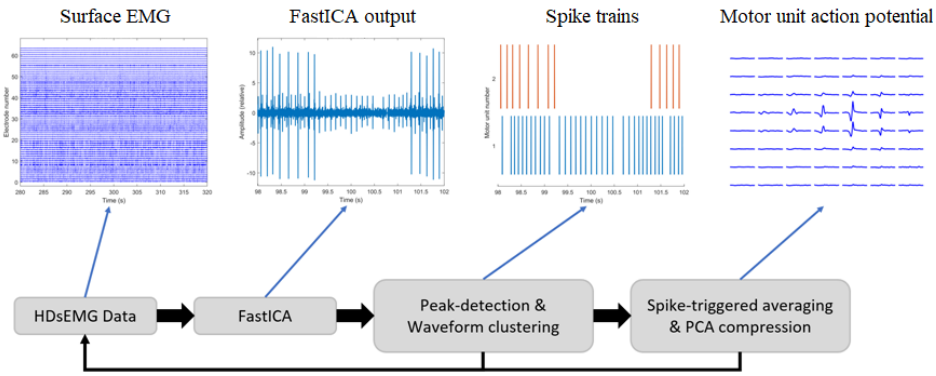

Figure 6.1. A block diagram of the motor unit decomposition method for HDsEMG proposed in Paper I, based on FastICA, iterative peel-off, and PCA compression.

Paper II:
Inferring position of motor units from high-density surface EMG

This paper presents an automatic, non-invasive method for motor unit localization from HDsEMG data. By applying principal component compression and a rotatable Gaussian surface fit to MUAP amplitude distributions, the method estimates the position and fibre direction of motor units. Validation was conducted in two scenarios: one with motor units obtained through synchronized iEMG and ultrasound as reference, and another with motor units obtained through decomposition of HDsEMG during specific muscle contractions. The results demonstrate the method's ability to discern the distinct spatial distributions of motor units between different muscle contractions, which could be used to assess individual muscles on a motor unit level.

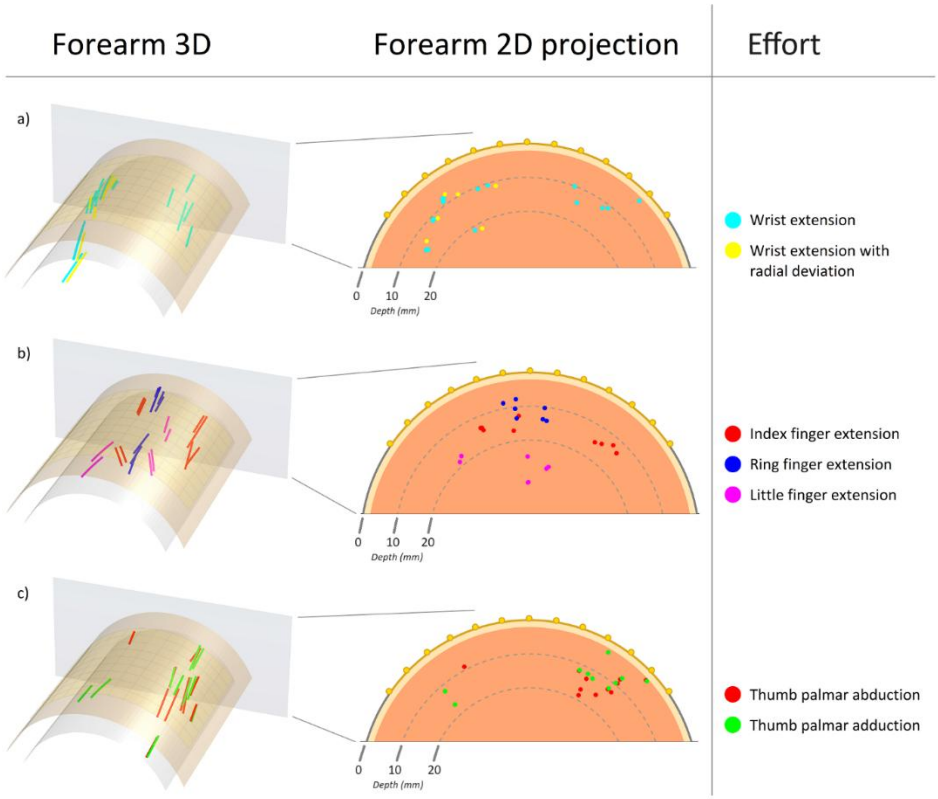

Figure 6.2. The localization results of motor units identified through decomposition of HDsEMG data during specific actions.

Paper III:
Muscle activity mapping by single peak localization from HDsEMG

This study explores a novel approach for mapping muscle activity by localizing and visualizing individual time-domain peaks in HDsEMG recordings, rather than decomposed motor units, aiming to provide a more robust alternative for assessing muscle activation patterns in the forearm. A vast number of localized peaks are then used to define distinct muscle volumes corresponding to different finger movements. The study demonstrates that the organization of the estimated muscle regions remain highly consistent across participants and follow anatomical expectations. The identified volumes are further utilized to classify individual EMG peaks, achieving high classification accuracy for finger extensions. By circumventing the need for motor unit decomposition, this approach provides a scalable and interpretable alternative for analysing muscle activity in dense anatomical regions, with potential applications in human-machine interfaces, rehabilitation, and prosthetic control.

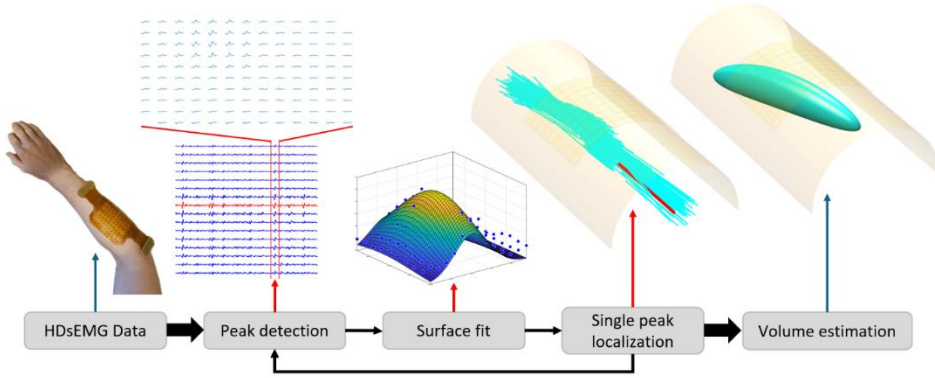

Figure 6.3. A block diagram of the muscle activity mapping and modelling method, proposed in Paper III.

Paper IV:
Generalizable gesture classification of HDsEMG using volume representations of muscles averaged across multiple individuals

This study presents a novel approach to gesture classification of HDsEMG data by utilizing functional volume representations of muscle regions. The work builds upon the previously developed method for muscle activity mapping (Paper III) and extends it to assess the generalizability of these representations across individuals and novel finger gestures. Volume representations were estimated based on the spatial distribution of localized time-domain peaks in the HDsEMG signals and averaged across multiple individuals. Instead of obtaining modelling data for all conceivable gestures, the approach focuses on identifying the activations of individual muscles, which has the potential to generalize to a wide range of gestures.

The model was created and tested on a publicly available dataset with 19 participants performing various single- and multi-digit gestures. By leveraging a leave-one-out approach to modelling and testing, the study showed that functional volume representations of muscles generalize across most individuals, which makes this method suitable for widespread applications. Furthermore the method showed limited generalizability to multi-digit gestures, in a model created only using single-digit gestures. These findings are an initial step towards the creation of comprehensive three-dimensional models, usable by anyone for gesture classification, without additional training or modelling data.

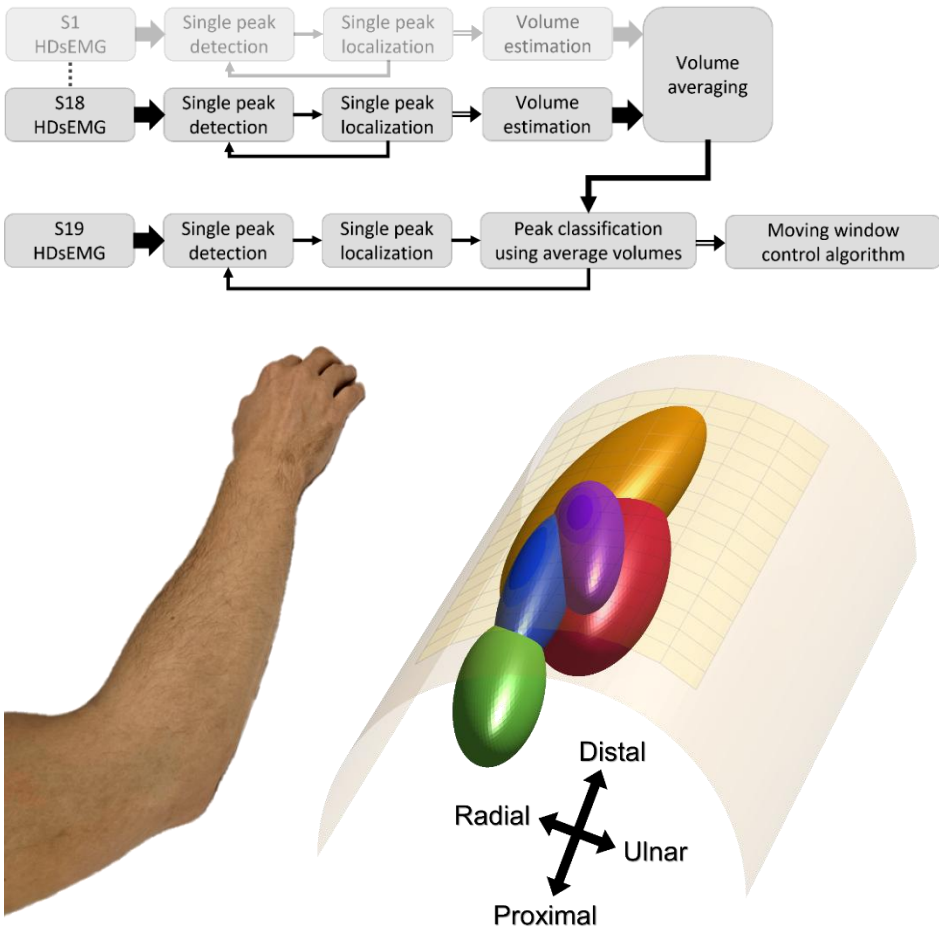

Figure 6.4. A block diagram (top) of the modelling of representative muscle volumes and subsequent classification of new data. With a set of average volume representations in a cylinder model of the forearm (bottom) for extension of the thumb (red), index finger (orange), middle finger (green), ring finger (blue), and little finger (purple).

Chapter 7

Discussion and outlook

This entire project started with the idea of non-invasively localizing motor units, aiming to track muscle activity in patients during rehabilitation following conditions such as stroke. In some ways the initial aim was met, in other ways it evolved, and in a few ways, it left more to be desired. The guiding philosophy in the development of the methods in this dissertation has been to keep things as simple as possible, and no simpler. Each step has always been relatively straightforward, whereas the complexity arose in the aggregate. In this chapter, I will discuss the progress and evolution of this project, the thoughts behind it and throughout, the results and their impact, and the future directions as I see it; all with a bit less formality and more subjectivity.

Decomposition

At the onset of the project, motor unit decomposition programs for HDsEMG were scarce, limited to a few commercial alternatives. The program we initially used for decomposition had several limitations. Firstly, the transfer of data and results between the decomposition software and my own code in Matlab or Python was cumbersome. But most importantly, it was not open source, which was severely restrictive when attempting to improve the processing pipeline. This was the motivation for making a new decomposition algorithm.

Paper I delivered a decomposition algorithm which is rather simple on a surface level, with several additions aiming to provide incremental performance improvements. Beyond the source separation algorithm, two main challenges in motor unit decomposition are that the problem is underdetermined and that repeated iterations may converge on the same source. The peel-off approach is arguably the simplest and most straightforward way to solve both problems at once. As long as the motor unit signal is correctly identified and directly subtracted from the dataset, it becomes irrelevant

whether the problem is over- or underdetermined. In the ideal case, an iterative peel-off algorithm removes a single motor unit completely from the dataset, and this process can repeat in perpetuity. In practice, however, avoiding mistakes and minor alignment errors in the removal process of every iteration is likely impossible, resulting in a buildup of residual noise. The additional steps presented in the method of Paper I, attempted to address these issues. Both PCA compression of the MUAP waveform distribution and the high-dimensional clustering of the motor unit spike train aimed to generate accurate MUAP representations while minimizing noise. However, multiple other techniques which have become common in motor unit decomposition algorithms could be incorporated in the future. As presented, the method is lacking any assessments of the consistency in the inter-spike intervals, or instantaneous firing rates. Moreover, it seems to me that the most optimal approach is a dual or two-phase decomposition; where the motor unit is first estimated quickly by FastICA and then enters a second more thorough iteration, such as constrained FastICA[148], to improve the initial estimate. The field of motor unit decomposition is advancing quickly since recent years, and the move towards open-source algorithms greatly facilitate the integration of multiple techniques. However, I share the concerns expressed in the recent review by Chen and Zhou[152] about motor unit decomposition yields. It is easy, in my experience, to generate a significant number of motor units with dubious reliability. I believe full transparency and availability of decomposition results and the HDsEMG dataset used is therefore desirable.

Regarding the work presented in Paper I, I believe using PCA compression to reduce noise in the MUAP waveform distribution may be the strongest contribution, as this idea extends beyond decomposition algorithms, and is used throughout all papers. Moreover, this work made clear some limitations in decomposition algorithms, which would inform the direction of Paper III and IV.

Localization

In contrast to motor unit decomposition, motor unit localization has received far less attention. Paper II brought the motor unit localization technique of Roeleveld et al[84] from one dimension into two, making multiple advances in the process. In contrast to the original method, using a linear array of electrodes, the main idea of Paper II was to make use of the additional information high-density grids provide, to create a more optimal and automatic estimate of motor unit depth. The idea of estimating the FWHM of the amplitudes in the waveform distribution remains the same, however. The two-dimensional Gaussian function incorporated all electrodes of the grid, to create a more robust FWHM estimate. Rotation was introduced by applying a rotation matrix to the coordinate system, which allowed for an estimate of fibre direction. The analytical

volume conductor model was chosen to be as mathematically simple as possible. In this case, many papers have been published on models with varying complexity. This is a key area which I think should be explored to improve localization accuracy, expressly with the aim to increase the contrast between estimates along the depth axis. In Paper II, PCA compression also re-enters the picture; through noise reduction the residual signal on channels further away from the action potential centre are pushed towards zero, making the subsequent Gaussian fit very stable, and resilient to noise. The localization method, in my view, is very robust due to the relative simplicity of the calculations. This simplicity furthermore makes it easily adaptable, and the surface fitting approach to localization can be applied to any other anatomical region as well as the forearm. I believe it can easily be incorporated into any future method that would benefit from the spatial characteristics of identified motor units.

The issue, however, is quite clear with regards to the aim of tracking overall muscle activity; the reliance on motor unit decomposition severely limits conclusions on the broader distribution of muscle activity. Decomposition algorithms do not identify all motor units, and the decomposed subset may not reflect the full distribution. Furthermore, decomposition is more robust and better validated in offline processing methods compared to real-time methods, limiting their current application in prosthetics or HMIs. At this point it is essential to consider what the end application is. Motor unit analysis is very valuable to physiological investigations and assessments relating to the output of individual motor neurons. However, mapping the full distribution of muscle activity or inferring strength of a specific muscle, could be achieved more easily without decomposition, which is the thought that guided the move away from motor units in Paper III.

Modelling

Paper III took the localization algorithm from decomposition and motor units to the HDsEMG data directly. The central idea was that the individual localization estimates would have a very high variance, but a vast number of estimates would achieve statistical robustness in aggregate, enabling the spatial modelling of distinct muscle volumes. Worth noting here, is that PCA compression was used again to reduce noise and increased the robustness of individual estimates. This approach, in my view, overperformed expectations. While this work was limited to low-force contractions, the degree to which the activity within the EDC, a single fused muscle, could be distinctly separated was surprising. From the spatial distribution of localization estimates, muscle regions were modelled with representative ellipsoid volumes, to be used as classifiers. Unlike classification using, e.g., neural networks, this form of spatial classification using volumes is highly intuitive and easy to visualize, as well as surprisingly consistent. It

may or may not work for higher forces in its current form, but I believe it is a strong contender in many applications. For example, to assess muscle synergies and load sharing for patients with reduced motor function, as visual biofeedback during rehabilitation, or as discrete control in low-effort HMIs.

The final, yet to be published, Paper IV, was perhaps the most far-reaching work included in this dissertation. The initial idea was to test whether volumes as classifiers would generalize across users. The cross-user generalizability was surprisingly strong, particularly given the small size of the EDC muscle. The far-reaching question posed by this work was whether multi-labelled data could be classified using a model based on single-labelled data. The distribution of classified activity was clearly distinct, though classification performance was more limited in this case. Regardless, I believe these results show significant potential for generic HMI applications, especially those that prioritize minimal training and widespread adoption.

With minimal calibration and intuitive spatial interpretability, these models could be embedded into future plug-and-play interfaces that require little to no expertise. Moreover, by adapting the localization algorithm for real-time processing, these methods lay the groundwork for a new form of EMG-based systems. In clinical settings, this could empower therapists and patients with robust, visual insight into muscle function, revealing the organization, strength, and compensation strategies of various muscles. In consumer applications, it could open the door to the seamless use of wearable devices that interface with a multitude of systems in our environment. If future technologies continue to prioritize simplicity, interpretability, and adaptability, we may eventually see EMG-based interfaces as natural extensions of our neuromuscular system, as intuitive and inconspicuous as the movement of our limbs.

References

[1] Merletti, R. & Cerone, G. Tutorial. Surface EMG detection, conditioning and pre-processing: Best practices. *Journal of Electromyography and Kinesiology* **54**, 102440 (2020).

[2] Merletti, R. & Muceli, S. Tutorial. Surface EMG detection in space and time: Best practices. *Journal of Electromyography and Kinesiology* **49**, 102363 (2019).

[3] Campanini, I., Disselhorst-Klug, C., Rymer, W. Z. & Merletti, R. Surface EMG in clinical assessment and neurorehabilitation: barriers limiting its use. *Frontiers in Neurology* **11**, 556522 (2020).

[4] Drost, G., Stegeman, D. F., Van Engelen, B. G. & Zwarts, M. J. Clinical applications of high-density surface EMG: a systematic review. *Journal of Electromyography and Kinesiology* **16**, 586-602 (2006).

[5] Zwarts, M. J. & Stegeman, D. F. Multichannel surface EMG: basic aspects and clinical utility. *Muscle & Nerve: Official Journal of the American Association of Electrodiagnostic Medicine* **28**, 1-17 (2003).

[6] Trent, L. *et al.* A narrative review: current upper limb prosthetic options and design. *Disability and Rehabilitation: Assistive Technology* (2020).

[7] Ribeiro, J. *et al.* Analysis of man-machine interfaces in upper-limb prosthesis: A review. *Robotics* **8**, 16 (2019).

[8] Marinelli, A. *et al.* Active upper limb prostheses: A review on current state and upcoming breakthroughs. *Progress in Biomedical Engineering* **5**, 012001 (2023).

[9] Zongxing, L. *et al.* Human–machine interaction technology for simultaneous gesture recognition and force assessment: A review. *IEEE Sensors Journal* **23**, 26981-26996 (2023).

[10] Guo, L., Lu, Z. & Yao, L. Human-machine interaction sensing technology based on hand gesture recognition: A review. *IEEE Transactions on Human-Machine Systems* **51**, 300-309 (2021).

[11] Su, R., Chen, X., Cao, S. & Zhang, X. Random forest-based recognition of isolated sign language subwords using data from accelerometers and surface electromyographic sensors. *Sensors* **16**, 100 (2016).

[12] Vasiljevas, M., Turčinas, R. & Damaševičius, R. Development of EMG-based speller. In *Proceedings of the XV International Conference on Human Computer Interaction.* 1-5 (2014).

[13] Widmaier, E. & Strang, K. *Vander's Human Physiology: 13th Edition*. (McGraw-Hill, 2013).

[14] Brodal, P. *The central nervous system*. (Oxford University Press, 2010).

[15] Kinnischtzke, A. K., Simons, D. J. & Fanselow, E. E. Motor cortex broadly engages excitatory and inhibitory neurons in somatosensory barrel cortex. *Cerebral Cortex* **24**, 2237-2248 (2014).

[16] Penfield, W. & Boldrey, E. Somatic motor and sensory representation in the cerebral cortex of man as studied by electrical stimulation. *Brain* **60**, 389-443 (1937).

[17] Huber, L. *et al.* Sub-millimeter fMRI reveals multiple topographical digit representations that form action maps in human motor cortex. *Neuroimage* **208**, 116463 (2020).

[18] Wagner, F. B. *et al.* Targeted neurotechnology restores walking in humans with spinal cord injury. *Nature* **563**, 65-71 (2018).

[19] Danner, S. M. *et al.* Human spinal locomotor control is based on flexibly organized burst generators. *Brain* **138**, 577-588 (2015).

[20] Ahuja, C. S. *et al.* Traumatic spinal cord injury. *Nature Reviews Disease Primers* **3**, 1-21 (2017).

[21] Hodgkin, A. L. & Huxley, A. F. A quantitative description of membrane current and its application to conduction and excitation in nerve. *The Journal of Physiology* **117**, 500 (1952).

[22] Berry, M. & Meister, M. Refractoriness and neural precision. *Advances in Neural Information Processing Systems* **10** (1997).

[23] Trapp, B. D. & Stys, P. K. Virtual hypoxia and chronic necrosis of demyelinated axons in multiple sclerosis. *The Lancet Neurology* **8**, 280-291 (2009).

[24] Chen, D. *et al.* Demyelinating processes in aging and stroke in the central nervous system and the prospect of treatment strategy. *CNS Neuroscience & Therapeutics* **26**, 1219-1229 (2020).

[25] Waxman, S. G. Demyelination in spinal cord injury. *Journal of the Neurological Sciences* **91**, 1-14 (1989).

[26] Heckman, C. & Enoka, R. M. Motor unit. *Comprehensive Physiology*, 2629-2682 (2012).

[27] Park, K. S. Electrical Signals from the Muscles and Nerves. In *Humans and Electricity: Understanding Body Electricity and Applications*, 199-222 (Springer International Publishing, 2023).

[28] Liddell, E. G. T. & Sherrington, C. S. Recruitment and some other features of reflex inhibition. *Proceedings of the Royal Society of London. Series B, Containing Papers of a Biological Character* **97**, 488-518 (1925).

[29] Duchateau, J. & Enoka, R. M. Human motor unit recordings: origins and insight into the integrated motor system. *Brain Research* **1409**, 42-61 (2011).

[30] Clarac, F. & Barbara, J.-G. The emergence of the "motoneuron concept": From the early 19th C to the beginning of the 20th C. *Brain Research* **1409**, 23-41 (2011).

[31] Enoka, R. M. & Fuglevand, A. J. Motor unit physiology: some unresolved issues. *Muscle & Nerve: Official Journal of the American Association of Electrodiagnostic Medicine* **24**, 4-17 (2001).

[32] Krnjević, K. & Miledi, R. Motor units in the rat diaphragm. *The Journal of Physiology* **140**, 427 (1958).

[33] Kugelberg, E. & Edström, L. Differential histochemical effects of muscle contractions on phosphorylase and glycogen in various types of fibres: relation to fatigue. *Journal of Neurology, Neurosurgery, and Psychiatry* **31**, 415 (1968).

[34] Fuglevand, A. J., Winter, D. A. & Patla, A. E. Models of recruitment and rate coding organization in motor-unit pools. *Journal of Neurophysiology* **70**, 2470-2488 (1993).

[35] Clamann, H. P. Motor unit recruitment and the gradation of muscle force. *Physical Therapy* **73**, 830-843 (1993).

[36] Fuglevand, A. J., Macefield, V. G. & Bigland-Ritchie, B. Force-frequency and fatigue properties of motor units in muscles that control digits of the human hand. *Journal of Neurophysiology* **81**, 1718-1729 (1999).

[37] Henneman, E. Relation between size of neurons and their susceptibility to discharge. *Science* **126**, 1345-1347 (1957).

[38] Duchateau, J. & Enoka, R. M. Distribution of motor unit properties across human muscles. *Journal of Applied Physiology* **132**, 1-13 (2022).

[39] Matsuzawa, K. *et al*. The origin structure of each finger in the flexor digitorum superficialis muscle. *Surgical and Radiologic Anatomy* **43**, 3-10 (2021).

[40] Perotto, A. O. *Anatomical guide for the electromyographer: the limbs and trunk*. (Charles C Thomas Publisher, 2011).

[41] Moore, K. L. & Dalley, A. F. *Clinically oriented anatomy*. (Wolters Kluwer, 2018).

[42] Chaudhry, M., Aminullah, H., Sinkler, M. A. & Arain, A. *Anatomy, shoulder and upper limb, forearm compartments*. (StatPearls Publishing, 2023).

[43] Van Duinen, H., Yu, W. S. & Gandevia, S. C. Limited ability to extend the digits of the human hand independently with extensor digitorum. *The Journal of Physiology* **587**, 4799-4810 (2009).

[44] Leijnse, J. N., Campbell-Kyureghyan, N. H., Spektor, D. & Quesada, P. M. Assessment of individual finger muscle activity in the extensor digitorum communis by surface EMG. *Journal of Neurophysiology* **100**, 3225-3235 (2008).

[45] Leijnse, J., Carter, S., Gupta, A. & McCabe, S. Anatomic basis for individuated surface EMG and homogeneous electrostimulation with neuroprostheses of the extensor digitorum communis. *Journal of Neurophysiology* **100**, 64-75 (2008).

[46] Basmajian, J. V. & De Luca, C. J. *Muscles Alive: Their Functions Revealed by Electromyography*. (Williams & Wilkins, 1985).

[47] Merletti, R. & Farina, D. Analysis of intramuscular electromyogram signals. *Philosophical Transactions of the Royal Society A: Mathematical, Physical and Engineering Sciences* **367**, 357-368 (2009).

[48] Adrian, E. D. & Bronk, D. W. The discharge of impulses in motor nerve fibres: Part II. The frequency of discharge in reflex and voluntary contractions. *The Journal of Physiology* **67**, i3 (1929).

[49] Karacan, I. & Türker, K. S. A comparison of electromyography techniques: surface versus intramuscular recording. *European Journal of Applied Physiology*, 1-17 (2024).

[50] Farina, D., Mesin, L., Martina, S. & Merletti, R. Comparison of spatial filter selectivity in surface myoelectric signal detection: influence of the volume conductor model. *Medical and Biological Engineering and Computing* **42**, 114-120 (2004).

[51] Muceli, S. *et al.* Blind identification of the spinal cord output in humans with high-density electrode arrays implanted in muscles. *Science Advances* **8**, eabo5040 (2022).

[52] Farina, D., Cescon, C. & Merletti, R. Influence of anatomical, physical, and detection-system parameters on surface EMG. *Biological Cybernetics* **86**, 445-456 (2002).

[53] Disselhorst-Klug, C., Silny, J. & Rau, G. Improvement of spatial resolution in surface-EMG: a theoretical and experimental comparison of different spatial filters. *IEEE Transactions on Biomedical Engineering* **44**, 567-574 (1997).

[54] Farina, D. & Holobar, A. Characterization of human motor units from surface EMG decomposition. *Proceedings of the IEEE* **104**, 353-373 (2016).

[55] Merletti, R., Holobar, A. & Farina, D. Analysis of motor units with high-density surface electromyography. *Journal of Electromyography and Kinesiology* **18**, 879-890 (2008).

[56] Muceli, S. & Merletti, R. Tutorial. Frequency analysis of the surface EMG signal: best practices. *Journal of Electromyography and Kinesiology* **79**, 102937 (2024).

[57] Boyer, M., Bouyer, L., Roy, J.-S. & Campeau-Lecours, A. Reducing noise, artifacts and interference in single-channel EMG signals: A review. *Sensors* **23**, 2927 (2023).

[58] Broman, H., De Luca, C., Rau, G., Kadefors, R. & Winter, D. *Units, terms and standards in the reporting of EMG research*. (International Society of Electrophysiological Kinesiology, 1980).

[59] Stegeman, D. & Hermens, H. Standards for surface electromyography: The European project Surface EMG for non-invasive assessment of muscles (SENIAM). *Enschede: Roessingh Research and Development* **10**, 8-12 (2007).

[60] Merletti, R. Standards for reporting EMG data. *Journal of Electromyography and Kinesiology* **9**, 3-4 (1999).

[61] Huigen, E., Peper, A. & Grimbergen, C. Investigation into the origin of the noise of surface electrodes. *Medical and Biological Engineering and Computing* **40**, 332-338 (2002).

[62] De Luca, C. J., Gilmore, L. D., Kuznetsov, M. & Roy, S. H. Filtering the surface EMG signal: Movement artifact and baseline noise contamination. *Journal of Biomechanics* **43**, 1573-1579 (2010).

[63] Clancy, E. A., Morin, E. L. & Merletti, R. Sampling, noise-reduction and amplitude estimation issues in surface electromyography. *Journal of Electromyography and Kinesiology* **12**, 1-16 (2002).

[64] Drake, J. D. & Callaghan, J. P. Elimination of electrocardiogram contamination from electromyogram signals: An evaluation of currently used removal techniques. *Journal of Electromyography and Kinesiology* **16**, 175-187 (2006).

[65] Glover, J. Adaptive noise canceling applied to sinusoidal interferences. *IEEE Transactions on Acoustics, Speech, and Signal Processing* **25**, 484-491 (1977).

[66] Keshtkaran, M. R. & Yang, Z. A fast, robust algorithm for power line interference cancellation in neural recording. *Journal of Neural Engineering* **11**, 026017 (2014).

[67] Botter, A. & Vieira, T. M. Filtered virtual reference: A new method for the reduction of power line interference with minimal distortion of monopolar surface EMG. *IEEE Transactions on Biomedical Engineering* **62**, 2638-2647 (2015).

[68] Ghaderi, P. & Marateb, H. R. Muscle activity map reconstruction from high density surface EMG signals with missing channels using image inpainting and surface reconstruction methods. *IEEE Transactions on Biomedical Engineering* **64**, 1513-1523 (2016).

[69] Rojas-Martínez, M., Mañanas, M. A. & Alonso, J. F. High-density surface EMG maps from upper-arm and forearm muscles. *Journal of Neuroengineering and Rehabilitation* **9**, 1-17 (2012).

[70] Rojas-Martínez, M., Mañanas, M., Alonso, J. & Merletti, R. Identification of isometric contractions based on High Density EMG maps. *Journal of Electromyography and Kinesiology* **23**, 33-42 (2013).

[71] Kleine, B.-U., Schumann, N.-P., Stegeman, D. F. & Scholle, H.-C. Surface EMG mapping of the human trapezius muscle: the topography of monopolar and bipolar surface EMG amplitude and spectrum parameters at varied forces and in fatigue. *Clinical Neurophysiology* **111**, 686-693 (2000).

[72] Vieira, T. M., Merletti, R. & Mesin, L. Automatic segmentation of surface EMG images: Improving the estimation of neuromuscular activity. *Journal of Biomechanics* **43**, 2149-2158 (2010).

[73] Gallina, A., Merletti, R. & Gazzoni, M. Uneven spatial distribution of surface EMG: what does it mean? *European Journal of Applied Physiology* **113**, 887-894 (2013).

[74] Tam, S., Boukadoum, M., Campeau-Lecours, A. & Gosselin, B. A fully embedded adaptive real-time hand gesture classifier leveraging HD-sEMG and deep learning. *IEEE Transactions on Biomedical Circuits and Systems* **14**, 232-243 (2019).

[75] Geng, W. *et al.* Gesture recognition by instantaneous surface EMG images. *Scientific Reports* **6**, 36571 (2016).

[76] Grönlund, C., Östlund, N., Roeleveld, K. & Karlsson, J. S. Simultaneous estimation of muscle fibre conduction velocity and muscle fibre orientation using 2D multichannel surface electromyogram. *Medical and Biological Engineering and Computing* **43**, 63-70 (2005).

[77] Rodriguez-Falces, J., Negro, F., Gonzalez-Izal, M. & Farina, D. Spatial distribution of surface action potentials generated by individual motor units in the human biceps brachii muscle. *Journal of Electromyography and Kinesiology* **23**, 766-777 (2013).

[78] Van Elswijk, G. *et al.* Muscle imaging: Mapping responses to transcranial magnetic stimulation with high-density surface electromyography. *Cortex* **44**, 609-616 (2008).

[79] Gallina, A. & Botter, A. Spatial localization of electromyographic amplitude distributions associated to the activation of dorsal forearm muscles. *Frontiers in Physiology* **4**, 67953 (2013).

[80] Jesinger, R. A. & Stonick, V. L. Processing signals from surface electrode arrays for noninvasive 3D mapping of muscle activity. In *Proceedings of IEEE 6th Digital Signal Processing Workshop.* 57-60 (IEEE, 1994).

[81] Stonick, J. T., Jesinger, R. A., Stonick, V. L. & Baumann, S. B. Estimation and localization of multiple dipole sources for noninvasive mapping of muscle activity. In *1996 IEEE International Conference on Acoustics, Speech, and Signal Processing Conference Proceedings.* 2912-2915 (IEEE, 1996).

[82] Van Den Doel, K., Ascher, U. M. & Pai, D. K. Source localization in electromyography using the inverse potential problem. *Inverse Problems* **27**, 025008 (2011).

[83] Van Den Doel, K., Ascher, U. M. & Pai, D. K. Computed myography: three-dimensional reconstruction of motor functions from surface EMG data. *Inverse Problems* **24**, 065010 (2008).

[84] Roeleveld, K., Stegeman, D., Vingerhoets, H. & Oosterom, A. V. The motor unit potential distribution over the skin surface and its use in estimating the motor unit location. *Acta Physiologica Scandinavica* **161**, 465-472 (1997).

[85] Roeleveld, K., Blok, J. H., Stegeman, D. F. & Van Oosterom, A. Volume conduction models for surface EMG; confrontation with measurements. *Journal of Electromyography and Kinesiology* **7**, 221-232 (1997).

[86] Roeleveld, K., Stegeman, D. F., Falck, B. & Stålberg, E. V. Motor unit size estimation: confrontation of surface EMG with macro EMG. *Electroencephalography and Clinical Neurophysiology/Electromyography and Motor Control* **105**, 181-188 (1997).

[87] Roeleveld, K., Stegeman, D., Vingerhoets, H. & Oosterom, A. V. Motor unit potential contribution to surface electromyography. *Acta Physiologica Scandinavica* **160**, 175-183 (1997).

[88] Farina, D., Mesin, L., Martina, S. & Merletti, R. A surface EMG generation model with multilayer cylindrical description of the volume conductor. *IEEE Transactions on Biomedical Engineering* **51**, 415-426 (2004).

[89] Mesin, L. Volume conductor models in surface electromyography: computational techniques. *Computers in Biology and Medicine* **43**, 942-952 (2013).

[90] Farina, D., Mesin, L. & Martina, S. Advances in surface electromyographic signal simulation with analytical and numerical descriptions of the volume conductor. *Medical and Biological Engineering and Computing* **42**, 467-476 (2004).

[91] Mesin, L. & Farina, D. A model for surface EMG generation in volume conductors with spherical inhomogeneities. *IEEE Transactions on Biomedical Engineering* **52**, 1984-1993 (2005).

[92] Mesin, L. Simulation of surface EMG signals for a multilayer volume conductor with a superficial bone or blood vessel. *IEEE Transactions on Biomedical Engineering* **55**, 1647-1657 (2008).

[93] Lowery, M. M., Stoykov, N. S., Dewald, J. P. & Kuiken, T. A. Volume conduction in an anatomically based surface EMG model. *IEEE Transactions on Biomedical Engineering* **51**, 2138-2147 (2004).

[94] Chauvet, E., Fokapu, O. & Gamet, D. Inverse problem in the surface EMG: A feasibility study. In *2001 Conference Proceedings of the 23rd Annual International Conference of the IEEE Engineering in Medicine and Biology Society.* 1048-1050 (IEEE, 2001).

[95] Mesin, L. & Troiano, A. Motor unit distribution estimation by multi-channel surface EMG. In *4th IET International Conference on Advances in Medical, Signal and Information Processing-MEDSIP 2008.* 1-3 (IET, 2008).

[96] Mesin, L. Real time identification of active regions in muscles from high density surface electromyogram. *Computers in Biology and Medicine* **56**, 37-50 (2015).

[97] Fisher, R. A. The use of multiple measurements in taxonomic problems. *Annals of Eugenics* **7**, 179-188 (1936).

[98] Cortes, C. & Vapnik, V. Support-vector networks. *Machine Learning* **20**, 273-297 (1995).

[99] Haykin, S. *Adaptive Filter Theory: International Edition*. (Pearson Education, 2014).

[100] Hyvärinen, A., Karhunen, J. & Oja, E. *Independent Component Analysis*. (Wiley, 2001).

[101] Hyvärinen, A. & Oja, E. A fast fixed-point algorithm for independent component analysis. *Neural Computation* **9**, 1483-1492 (1997).

[102] Comon, P. Independent component analysis, a new concept? *Signal Processing* **36**, 287-314 (1994).

[103] De Luca, C. J. & Adam, A. Decomposition and analysis of intramuscular electromyographic signals. In *Modern Techniques in Neuroscience Research*, 757-776 (Springer, 1999).

[104] LeFever, R. S. & De Luca, C. J. A procedure for decomposing the myoelectric signal into its constituent action potentials-part I: technique, theory, and implementation. *IEEE Transactions on Biomedical Engineering*, 149-157 (1982).

[105] Lefever, R. S., Xenakis, A. P. & De Luca, C. J. A procedure for decomposing the myoelectric signal into its constituent action potentials-part II: execution and test for accuracy. *IEEE Transactions on Biomedical Engineering*, 158-164 (1982).

[106] McGill, K. C. & Dorfman, L. J. High-resolution alignment of sampled waveforms. *IEEE Transactions on Biomedical Engineering*, 462-468 (1984).

[107] McGill, K. C., Lateva, Z. C. & Marateb, H. R. EMGLAB: an interactive EMG decomposition program. *Journal of Neuroscience Methods* **149**, 121-133 (2005).

[108] McGill, K. C. Optimal resolution of superimposed action potentials. *IEEE Transactions on Biomedical Engineering* **49**, 640-650 (2002).

[109] Stashuk, D. W. Decomposition and quantitative analysis of clinical electromyographic signals. *Medical Engineering & Physics* **21**, 389-404 (1999).

[110] Stashuk, D. & De Bruin, H. Automatic decomposition of selective needle-detected myoelectric signals. *IEEE Transactions on Biomedical Engineering* **35**, 1-10 (1988).

[111] Parsaei, H. & Stashuk, D. W. EMG signal decomposition using motor unit potential train validity. *IEEE Transactions on Neural Systems and Rehabilitation Engineering* **21**, 265-274 (2012).

[112] Stashuk, D. EMG signal decomposition: how can it be accomplished and used? *Journal of Electromyography and Kinesiology* **11**, 151-173 (2001).

[113] Gazzoni, M., Farina, D. & Merletti, R. A new method for the extraction and classification of single motor unit action potentials from surface EMG signals. *Journal of Neuroscience Methods* **136**, 165-177 (2004).

[114] Kleine, B. U., Van Dijk, J. P., Lapatki, B. G., Zwarts, M. J. & Stegeman, D. F. Using two-dimensional spatial information in decomposition of surface EMG signals. *Journal of Electromyography and Kinesiology* **17**, 535-548 (2007).

[115] Gligorijević, I. *et al.* A new and fast approach towards sEMG decomposition. *Medical & Biological Engineering & Computing* **51**, 593-605 (2013).

[116] De Luca, C. J., Chang, S.-S., Roy, S. H., Kline, J. C. & Nawab, S. H. Decomposition of surface EMG signals from cyclic dynamic contractions. *Journal of Neurophysiology* **113**, 1941-1951 (2015).

[117] Nawab, S. H., Chang, S.-S. & De Luca, C. J. High-yield decomposition of surface EMG signals. *Clinical Neurophysiology* **121**, 1602-1615 (2010).

[118] Xu, Z., Xiao, S. & Chi, Z. ART2 neural network for surface EMG decomposition. *Neural Computing & Applications* **10**, 29-38 (2001).

[119] Nakamura, H., Yoshida, M., Kotani, M., Akazawa, K. & Moritani, T. The application of independent component analysis to the multi-channel surface electromyographic signals for separation of motor unit action potential trains: Part I—Measuring techniques. *Journal of Electromyography and Kinesiology* **14**, 423-432 (2004).

[120] Hideo, N., Masaki, Y., Manabu, K., Kenzo, A. & Toshio, M. The application of independent component analysis to the multi-channel surface electromyographic signals for separation of motor unit action potential trains: part II—modelling interpretation. *Journal of Electromyography and Kinesiology* **14**, 433-441 (2004).

[121] García, G. A., Maekawa, K. & Akazawa, K. Decomposition of synthetic multi-channel surface-electromyogram using independent component analysis. In *Independent Component Analysis and Blind Signal Separation: Fifth International Conference, ICA 2004, Granada, Spain, September 22-24, 2004. Proceedings 5*. 985-992 (Springer, 2004).

[122] Garcia, G. A., Okuno, R. & Azakawa, K. A decomposition algorithm for surface electrode-array electromyogram. *IEEE Engineering in Medicine and Biology Magazine* **24**, 63-72 (2005).

[123] Theis, F. J. & García, G. A. On the use of sparse signal decomposition in the analysis of multi-channel surface electromyograms. *Signal Processing* **86**, 603-623 (2006).

[124] Zhou, P., Lowery, M. M. & Rymer, W. Z. Extracting Motor Unit Firing Information by Independent Component Analysis of Surface Electromyogram: A Preliminary Study Using a Simulation Approach. *The International Journal of Computers, Systems and Signals* **7**, 19-28 (2006).

[125] Holobar, A. & Zazula, D. Correlation-based decomposition of surface electromyograms at low contraction forces. *Medical and Biological Engineering and Computing* **42**, 487-495 (2004).

[126] Holobar, A. & Zazula, D. Multichannel blind source separation using convolution kernel compensation. *IEEE Transactions on Signal Processing* **55**, 4487-4496 (2007).

[127] Holobar, A. & Zazula, D. Gradient convolution kernel compensation applied to surface electromyograms. In *International Conference on Independent Component Analysis and Signal Separation.* 617-624 (Springer, 2007).

[128] Holobar, A., Farina, D., Gazzoni, M., Merletti, R. & Zazula, D. Estimating motor unit discharge patterns from high-density surface electromyogram. *Clinical Neurophysiology* **120**, 551-562 (2009).

[129] Chen, C., Ma, S., Yu, Y., Sheng, X. & Zhu, X. Segment-wise decomposition of surface electromyography to identify discharges across motor neuron populations. *IEEE Transactions on Neural Systems and Rehabilitation Engineering* **30**, 2012-2021 (2022).

[130] Ning, Y., Zhu, X., Zhu, S. & Zhang, Y. Surface EMG decomposition based on K-means clustering and convolution kernel compensation. *IEEE Journal of Biomedical and Health Informatics* **19**, 471-477 (2014).

[131] Mohebian, M. R. *et al.* Non-invasive decoding of the motoneurons: a guided source separation method based on convolution kernel compensation with clustered initial points. *Frontiers in Computational Neuroscience* **13**, 14 (2019).

[132] Zheng, Y. *et al.* High-density surface EMG decomposition by combining iterative convolution kernel compensation with an energy-specific peel-off strategy. *IEEE Transactions on Neural Systems and Rehabilitation Engineering* **31**, 3641-3651 (2023).

[133] Chen, C., Ma, S., Sheng, X. & Zhu, X. A peel-off convolution kernel compensation method for surface electromyography decomposition. *Biomedical Signal Processing and Control* **85**, 104897 (2023).

[134] Wen, Y. *et al.* A convolutional neural network to identify motor units from high-density surface electromyography signals in real time. *Journal of Neural Engineering* **18**, 056003 (2021).

[135] Clarke, A. K. *et al.* Deep learning for robust decomposition of high-density surface EMG signals. *IEEE Transactions on Biomedical Engineering* **68**, 526-534 (2020).

[136] Glaser, V., Holobar, A. & Zazula, D. Real-time motor unit identification from high-density surface EMG. *IEEE Transactions on Neural Systems and Rehabilitation Engineering* **21**, 949-958 (2013).

[137] Chen, C., Ma, S., Sheng, X., Farina, D. & Zhu, X. Adaptive real-time identification of motor unit discharges from non-stationary high-density surface electromyographic signals. *IEEE Transactions on Biomedical Engineering* **67**, 3501-3509 (2020).

[138] Glaser, V. & Holobar, A. Motor unit identification from high-density surface electromyograms in repeated dynamic muscle contractions. *IEEE Transactions on Neural Systems and Rehabilitation Engineering* **27**, 66-75 (2018).

[139] Kramberger, M. & Holobar, A. On the prediction of motor unit filter changes in blind source separation of high-density surface electromyograms during dynamic muscle contractions. *IEEE Access* **9**, 103533-103540 (2021).

[140] Chen, M. & Zhou, P. A novel framework based on FastICA for high density surface EMG decomposition. *IEEE Transactions on Neural Systems and Rehabilitation Engineering* **24**, 117-127 (2015).

[141] Negro, F., Muceli, S., Castronovo, A. M., Holobar, A. & Farina, D. Multi-channel intramuscular and surface EMG decomposition by convolutive blind source separation. *Journal of Neural Engineering* **13**, 026027 (2016).

[142] Chen, M., Zhang, X., Chen, X. & Zhou, P. Automatic implementation of progressive FastICA peel-off for high density surface EMG decomposition. *IEEE Transactions on Neural Systems and Rehabilitation Engineering* **26**, 144-152 (2017).

[143] Lundsberg, J., Björkman, A., Malesevic, N. & Antfolk, C. Compressed spike-triggered averaging in iterative decomposition of surface EMG. *Computer Methods and Programs in Biomedicine*, 107250 (2022).

[144] Wu, W. *et al.* A new EMG decomposition framework for upper limb prosthetic systems. *Journal of Bionic Engineering* **20**, 2646-2660 (2023).

[145] Zheng, Y. & Hu, X. Adaptive real-time decomposition of electromyogram during sustained muscle activation: a simulation study. *IEEE Transactions on Biomedical Engineering* **69**, 645-653 (2021).

[146] Zhao, H., Zhang, X., Chen, M. & Zhou, P. Online decomposition of surface electromyogram into individual motor unit activities using progressive FastICA peel-off. *IEEE Transactions on Biomedical Engineering* **71**, 160-170 (2023).

[147] Zhao, H., Zhang, X., Chen, M. & Zhou, P. Adaptive online decomposition of surface EMG using progressive FastICA peel-off. *IEEE Transactions on Biomedical Engineering* **71**, 1257-1268 (2023).

[148] Chen, M. & Zhou, P. 2CFastICA: AN ovel Method for H igh D ensity S urface EMG D ecomposition B ased on K ernel C onstrained FastICA and C orrelation C onstrained FastICA. *IEEE Transactions on Neural Systems and Rehabilitation Engineering* (2024).

[149] Avrillon, S., Hug, F., Baker, S. N., Gibbs, C. & Farina, D. Tutorial on MUedit: An open-source software for identifying and analysing the discharge timing of motor

units from electromyographic signals. *Journal of Electromyography and Kinesiology* **77**, 102886 (2024).

[150] Del Vecchio, A. *et al.* Tutorial: Analysis of motor unit discharge characteristics from high-density surface EMG signals. *Journal of Electromyography and Kinesiology* **53**, 102426 (2020).

[151] Holobar, A., Minetto, M. A. & Farina, D. Accurate identification of motor unit discharge patterns from high-density surface EMG and validation with a novel signal-based performance metric. *Journal of Neural Engineering* **11**, 016008 (2014).

[152] Chen, M. & Zhou, P. High-Density Surface EMG Decomposition: Achievements, Challenges, and Concerns. *IEEE Transactions on Neural Systems and Rehabilitation Engineering* (2025).

[153] Holobar, A., Minetto, M. A., Botter, A., Negro, F. & Farina, D. Experimental analysis of accuracy in the identification of motor unit spike trains from high-density surface EMG. *IEEE Transactions on Neural Systems and Rehabilitation Engineering* **18**, 221-229 (2010).

[154] Marateb, H. R. *et al.* Accuracy assessment of CKC high-density surface EMG decomposition in biceps femoris muscle. *Journal of Neural Engineering* **8**, 066002 (2011).

[155] Chen, M., Zhang, X., Lu, Z., Li, X. & Zhou, P. Two-source validation of progressive FastICA peel-off for automatic surface EMG decomposition in human first dorsal interosseous muscle. *International Journal of Neural Systems* **28**, 1850019 (2018).

[156] Chen, M., Holobar, A., Zhang, X. & Zhou, P. Progressive FastICA peel-off and convolution kernel compensation demonstrate high agreement for high density surface EMG decomposition. *Neural Plasticity* **2016** (2016).

[157] Dai, C. & Hu, X. Independent component analysis based algorithms for high-density electromyogram decomposition: Systematic evaluation through simulation. *Computers in Biology and Medicine* **109**, 171-181 (2019).

[158] Frigo, C. & Crenna, P. Multichannel SEMG in clinical gait analysis: a review and state-of-the-art. *Clinical Biomechanics* **24**, 236-245 (2009).

[159] Rosa, M. C. N., Marques, A., Demain, S., Metcalf, C. D. & Rodrigues, J. Methodologies to assess muscle co-contraction during gait in people with neurological impairment–a systematic literature review. *Journal of Electromyography and Kinesiology* **24**, 179-191 (2014).

[160] Gómez-Pérez, C., Font-Llagunes, J. M., Martori, J. C. & Vidal Samsó, J. Gait parameters in children with bilateral spastic cerebral palsy: a systematic review of

randomized controlled trials. *Developmental Medicine & Child Neurology* **61**, 770-782 (2019).

[161] Bashford, J., Mills, K. & Shaw, C. The evolving role of surface electromyography in amyotrophic lateral sclerosis: A systematic review. *Clinical Neurophysiology* **131**, 942-950 (2020).

[162] Becker, S. *et al.* The relationship between functionality and erector spinae activity in patients with specific low back pain during dynamic and static movements. *Gait & Posture* **66**, 208-213 (2018).

[163] Paoletti, M., Belli, A., Palma, L. & Pierleoni, P. Electromyography pattern likelihood analysis for flexion-relaxation phenomenon evaluation. *Electronics* **9**, 2046 (2020).

[164] Batista Jr, J. P. *et al.* Joint angle and movement velocity effects on muscle activity of elderly with knee osteoarthritis–categorized and probabilistic analysis. *Journal of Electromyography and Kinesiology* **41**, 50-59 (2018).

[165] Nawasreh, Z. H., Marmon, A. R., Logerstedt, D. & Snyder-Mackler, L. The effect of training on a compliant surface on muscle activation and co-contraction after anterior cruciate ligament injury. *International Journal of Sports Physical Therapy* **14**, 3554 (2019).

[166] De Luca, C. J. Myoelectrical manifestations of localized muscular fatigue in humans. *Critical Reviews in Biomedical Engineering* **11**, 251-279 (1984).

[167] Botter, A., Lanfranco, F., Merletti, R. & Minetto, M. A. Myoelectric fatigue profiles of three knee extensor muscles. *International Journal of Sports Medicine* **30**, 408-417 (2009).

[168] Al-Mulla, M. R., Sepulveda, F. & Colley, M. A review of non-invasive techniques to detect and predict localised muscle fatigue. *Sensors* **11**, 3545-3594 (2011).

[169] González-Izal, M., Malanda, A., Gorostiaga, E. & Izquierdo, M. Electromyographic models to assess muscle fatigue. *Journal of Electromyography and Kinesiology* **22**, 501-512 (2012).

[170] Tanabe, H., Fujii, K. & Kouzaki, M. Intermittent muscle activity in the feedback loop of postural control system during natural quiet standing. *Scientific Reports* **7**, 10631 (2017).

[171] Hodson-Tole, E. F., Loram, I. D. & Vieira, T. M. Myoelectric activity along human gastrocnemius medialis: different spatial distributions of postural and electrically elicited surface potentials. *Journal of Electromyography and Kinesiology* **23**, 43-50 (2013).

[172] Dos Anjos, F. V., Pinto, T. P., Gazzoni, M. & Vieira, T. M. The spatial distribution of ankle muscles activity discriminates aged from young subjects during standing. *Frontiers in Human Neuroscience* **11**, 190 (2017).

[173] Lapatki, B., Van Dijk, J., Van de Warrenburg, B. & Zwarts, M. Botulinum toxin has an increased effect when targeted toward the muscle's endplate zone: A high-density surface EMG guided study. *Clinical Neurophysiology* **122**, 1611-1616 (2011).

[174] Wissel, J. *et al.* Management of spasticity associated pain with botulinum toxin A. *Journal of Pain and Symptom Management* **20**, 44-49 (2000).

[175] Zhang, C. *et al.* Three dimensional innervation zone imaging in spastic muscles of stroke survivors. *Journal of Neural Engineering* **16**, 034001 (2019).

[176] Dipietro, L. *et al.* Customized interactive robotic treatment for stroke: EMG-triggered therapy. *IEEE Transactions on Neural Systems and Rehabilitation Engineering* **13**, 325-334 (2005).

[177] De Biase, M., Politti, F., Palomari, E., Barros-Filho, T. E. P. d. & De Camargo, O. Increased EMG response following electromyographic biofeedback treatment of rectus femoris muscle after spinal cord injury. *Physiotherapy* **97**, 175-179 (2011).

[178] Maat, B., Smit, G., Plettenburg, D. & Breedveld, P. Passive prosthetic hands and tools: A literature review. *Prosthetics and Orthotics International* **42**, 66-74 (2018).

[179] Smail, L. C., Neal, C., Wilkins, C. & Packham, T. L. Comfort and function remain key factors in upper limb prosthetic abandonment: findings of a scoping review. *Disability and Rehabilitation: Assistive Technology* **16**, 821-830 (2021).

[180] Salminger, S. *et al.* Current rates of prosthetic usage in upper-limb amputees–have innovations had an impact on device acceptance? *Disability and Rehabilitation* **44**, 3708-3713 (2022).

[181] Farina, D. & Aszmann, O. Bionic limbs: clinical reality and academic promises. *Science Translational Medicine* **6**, 257ps212-257ps212 (2014).

[182] Rackerby, R., Lukosch, S. & Munro, D. Understanding and measuring the cognitive load of amputees for rehabilitation and prosthesis development. *Archives of Rehabilitation Research and Clinical Translation* **4**, 100216 (2022).

[183] Parker, P., Englehart, K. & Hudgins, B. Myoelectric signal processing for control of powered limb prostheses. *Journal of Electromyography and Kinesiology* **16**, 541-548 (2006).

[184] Dipietro, L., Sabatini, A. M. & Dario, P. A survey of glove-based systems and their applications. *IEEE Transactions on Systems, Man, and Cybernetics, Part C (Applications and Reviews)* **38**, 461-482 (2008).

[185] Murata, T. & Shin, J. Hand gesture and character recognition based on kinect sensor. *International Journal of Distributed Sensor Networks* **10**, 278460 (2014).

[186] Zeng, W., Wang, C. & Wang, Q. Hand gesture recognition using leap motion via deterministic learning. *Multimedia Tools and Applications* **77**, 28185-28206 (2018).

[187] Akhlaghi, N. *et al.* Real-time classification of hand motions using ultrasound imaging of forearm muscles. *IEEE Transactions on Biomedical Engineering* **63**, 1687-1698 (2015).

[188] Sussillo, D., Kaifosh, P. & Reardon, T. A generic noninvasive neuromotor interface for human-computer interaction. CTRL-labs at Reality Labs (Preprint). *bioRxiv*, (2024).

[189] Simao, M., Mendes, N., Gibaru, O. & Neto, P. A review on electromyography decoding and pattern recognition for human-machine interaction. *IEEE Access* **7**, 39564-39582 (2019).

[190] Wu, J., Sun, L. & Jafari, R. A wearable system for recognizing American sign language in real-time using IMU and surface EMG sensors. *IEEE Journal of Biomedical and Health Informatics* **20**, 1281-1290 (2016).

[191] Zhang, X. *et al.* A framework for hand gesture recognition based on accelerometer and EMG sensors. *IEEE Transactions on Systems, Man, and Cybernetics-Part A: Systems and Humans* **41**, 1064-1076 (2011).

[192] Ajoudani, A., Tsagarakis, N. & Bicchi, A. Tele-impedance: Teleoperation with impedance regulation using a body–machine interface. *The International Journal of Robotics Research* **31**, 1642-1656 (2012).

[193] Sathiyanarayanan, M. & Mulling, T. Map navigation using hand gesture recognition: A case study using myo connector on apple maps. *Procedia Computer Science* **58**, 50-57 (2015).

[194] Nacke, L. E., Kalyn, M., Lough, C. & Mandryk, R. L. Biofeedback game design: using direct and indirect physiological control to enhance game interaction. In *Proceedings of the SIGCHI Conference on Human Factors in Computing Systems.* 103-112 (2011).

[195] Chen, K. B., Ponto, K., Tredinnick, R. D. & Radwin, R. G. Virtual exertions: Evoking the sense of exerting forces in virtual reality using gestures and muscle activity. *Human Factors* **57**, 658-673 (2015).

[196] Kutafina, E., Laukamp, D. & Jonas, S. M. Wearable sensors in medical education: supporting hand hygiene training with a forearm EMG. In *pHealth 2015*, 286-291 (IOS Press, 2015).

[197] Pan, T.-Y., Tsai, W.-L., Chang, C.-Y., Yeh, C.-W. & Hu, M.-C. A hierarchical hand gesture recognition framework for sports referee training-based EMG and accelerometer sensors. *IEEE Transactions on Cybernetics* **52**, 3172-3183 (2020).

Paper I

Compressed spike-triggered averaging in iterative decomposition of surface EMG

Lundsberg, J., Björkman, A., Malesevic, N., & Antfolk, C.

Published in: Computer Methods and Programs in Biomedicine, *228*, 107250. (2023)

Computer Methods and Programs in Biomedicine 228 (2023) 107250

Contents lists available at ScienceDirect

Computer Methods and Programs in Biomedicine

journal homepage: www.elsevier.com/locate/cmpb

Biomedical signal and image processing methods

Compressed spike-triggered averaging in iterative decomposition of surface EMG☆

Jonathan Lundsberg[a,*], Anders Björkman[b], Nebojsa Malesevic[a], Christian Antfolk[a,*]

[a] Dept. of Biomedical Engineering, Faculty of Engineering, Lund University, Lund, Sweden
[b] Dept. of Hand Surgery, Institute of Clinical Sciences, Sahlgrenska University Hospital and University of Gothenburg, Gothenburg, Sweden

ARTICLE INFO

Article history:
Received 8 April 2022
Revised 11 October 2022
Accepted 16 November 2022

Keywords:
Electromyography
decomposition
motor unit
FastICA
density-based clustering
PCA-compression

ABSTRACT

Background and Objective: Analysis of motor unit activity is important for assessing and treating diseases or injuries affecting natural movement. State-of-the-art decomposition translates high-density surface electromyography (HDsEMG) into motor unit activity. However, current decomposition methods offer far from complete separation of all motor units.

Methods: This paper proposes a peel-off approach to automatic decomposition of HDsEMG into motor unit action potential (MUAP) trains, based on the Fast Independent Component Analysis algorithm (FastICA). The novel steps include utilizing compression by means of Principal Component Analysis and spike-triggered averaging, to estimate surface MUAP distributions with less noise, which are iteratively subtracted from the HDsEMG dataset. Furthermore, motor unit spike trains are estimated by high-dimensional density-based clustering of peaks in the FastICA source output. And finally, a new reliability measure is used to discard poor motor unit estimates by comparing the variance of the FastICA source output before and after the peel-off step. The method was validated using reconstructed synthetic data at three different signal-to-noise levels and was compared to an established deflationary FastICA approach.

Results: Both algorithms had very high recall and precision, over 90%, for spikes from matching motor units, referred to as matched performance. However, the peel-off algorithm correctly identified more motor units for all noise levels. When accounting for unidentified motor units, total recall was up to 33 percentage points higher; and when accounting for duplicate estimates, total precision was up to 24 percentage points higher, compared to the state-of-the-art reference. In addition, a comparison was done using experimental data where the proposed algorithm had a matched recall of 97% and precision of 85% with respect to the reference algorithm.

Conclusion: These results show a substantial performance increase for decomposition of simulated HDsEMG data and serve to validate the proposed approach. This performance increase is an important step towards complete decomposition and extraction of information of motor unit activity.

1. Introduction

The recording of electromyography (EMG) signals is a widely established technique used clinically to diagnose certain neuromuscular diseases [1], to control prosthetic devices [2] and in biomechanics [3]. The basis of EMG is the electrical activity of muscle fibres. Commands to activate and control our skeletal muscles are sent from the brain using upper motor neurons which descend to the ventral horn of the spinal cord. Here, the upper motor neurons synapse with lower motor neurons. Axons from the lower motor neurons form the peripheral nerves, where action potentials are sent to groups of muscle cells (fibres). The signal is received at neuromuscular junctions, which start action potentials in the muscle fibres, causing them to contract. A single lower motor neuron and the muscle fibres it innervates make up a motor unit. Each action potential result in simultaneous activation (i.e. contraction) of all muscle fibres in that specific motor unit. This generates an electrical signal strong enough to reach recording electrodes positioned inside the muscle or on the skin surface. Through this neuromuscular connection, motor unit action potentials (MUAPs) recorded by EMG correspond to the outputs of individual motor neurons.

☆ Visiting address E-building, Ole Römers väg 3, SE-22,363, Lund, Sweden.
* Corresponding author at: Postal address P.O. Box 118, SE, 22100 Lund, Sweden.
E-mail addresses: jonathan.lundsberg@bme.lth.se (J. Lundsberg), christian.antfolk@bme.lth.se (C. Antfolk).

https://doi.org/10.1016/j.cmpb.2022.107250

The surface EMG signal is the summation of activity from all motor units within the recording area of the electrode.

Because of the complex superposition of underlying sources (motor units), surface EMG recordings offer limited information related to the individual originating action potentials. One approach to try and extract the underlying neural information is by decomposition. The intention of decomposition is to separate the mixed sources into their constituent parts. Successful decomposition allows for the individual study of motor units, which is an important aspect in several branches of science and engineering. In the case of neurology, analysis of motor unit activation patterns provides insights to the organization of neural pathways and diseases affecting motor function [4,5]. In the control of prosthetic limbs, a better functional understanding of the EMG signal could help to devise more natural control strategies based on decoding user intent at the level of individual motor units [6–8]. This type of direct translation from the basic units of human movement to fine control of a prosthesis could result in a more intimate body-machine interaction, ultimately reducing rejection rates of prosthetic devices due to poor function and control [9]. Hence, there is clearly much to gain from improving EMG decomposition techniques, and the number of motor units that can be separated.

The traditional approach to study motor units is by using intramuscular recordings (iEMG). By placing electrodes inside the muscle, the recording is far more local [5]. This effectively reduces the recording area since the motor units close to the electrode have a considerably stronger signal. Much work has been done on development and optimization of iEMG decomposition algorithms. Programs are readily available utilizing template matching and clustering techniques to try and extract the firing timings (spike trains) and waveforms of individual motor units [10,11]. The decomposition of iEMG signals is still being improved upon, with more recent attempts [12] using a peel-off approach to resolve superimposed waveforms. Furthermore, on-line decomposition of iEMG signals has been proposed [13], which allows for a much wider area of application. Since the iEMG signal is in a sense simple, validation of decomposition results, whilst time-consuming, can also be done manually. The disadvantage of using intramuscular electrodes is the invasive nature of such recordings. When recording electrodes penetrate the skin, there is a risk of infection, damage to the muscle fibres and surrounding tissue, and discomfort for the subject. Due to the more local nature of intramuscular recordings, multiple penetrations of the skin are required to get a more wholistic view of muscle activity. Thus, recordings from the skin surface are a more attractive alternative if sufficient decomposition can be achieved.

The surface EMG (sEMG) signal is more complex compared to the iEMG signal. The signal-to-noise ratio for sEMG is lower due to the increased distance from the muscle to the recording electrode, and the tissue in between. A surface EMG electrode can also pickup activity from adjacent muscles, which can be detrimental when trying to extract information from one specific muscle. The recording area for sEMG is effectively much larger than, e.g., a needle electrode used in iEMG. This relatively large recording area results in more overlapping action potentials being picked up at the electrode. A large amount of overlap makes a template matching approach difficult, although it has been explored with some success [14–16]. The reduction of electrode size and increase in electrode count present a recent tendency of many research groups to obtain more information regarding the electrical activity of the underlying muscles. A large number of electrodes adds spatial information which can be used to separate mixed sources. High-density surface electrode arrays (HDsEMG) have therefore opened up several alternatives for decomposition.

Approaches to decompose HDsEMG signals to their constituent parts have been proposed using different algorithms. Blind source separation techniques specifically, have been in focus, using higher and lower-order statistics. Zazula and Holobar studied decomposition by using higher-order cumulants [17], and also proposed the convolution kernel compensation (CKC) method [18], and the natural gradient CKC extension [19]. In the CKC method, the data is modelled as channel responses to sparse pulse trains, and the method aims to compensate these responses to reconstruct the pulse trains. Furthermore, Ning et al. claimed better decomposition performance by combining a modified CKC method with k-means clustering [20]. The CKC method has also been used recently in conjunction with deep learning, where recurrent [21] and convolutional [22] neural networks were trained on the CKC output. The results, however, provide relatively few motor units compared to the total amount present in muscles. Using Fast Independent Component Analysis (FastICA) [23] and an iterative removal process, Chen and Zhou proposed their progressive FastICA peel-off (PFP) approach [24], and its automated implementation [25]. It was shown to have similar accuracy as the CKC method [26], and has been validated for multichannel iEMG decomposition as well [27]. In the peel-off approach, motor units are estimated individually and subtracted from the dataset in each iteration. The removal process greatly reduces the likelihood of converging on the same solution again, which enables more motor units to be found in the following iterations. The downside, as argued by Negro et al. [28], is the possibility of induced noise from alignment errors. Negro et al. proposed the deflationary FastICA alternative, which avoids induced noise that may be caused by a peel-off approach. The orthogonalization step in their algorithm is instead what prevents further iterations from converging on the same solution. However, the signal produced by the motor unit sources is very complex as it is generated along the entire length of the muscle fibres. As the action potential travels from the neuromuscular junction to the ends of the muscle fibres, the signal at the surface shifts. From the perspective of the FastICA algorithm, which relies on spatial information, the same motor unit could be perceived as multiple spatially independent sources. The orthogonalization step in deflationary FastICA cannot always guarantee non-convergence on the same motor unit. Duplicate motor unit estimates must therefore be dealt with as well. Although the method by Negro et al. [28] has shown success in finding many motor units, the downside is an increasing complexity in the algorithm and computational load as the set of estimates expands. In contrast, the strength of the peel-off approach lies in how repeated convergence on the same motor unit is avoided. Additionally, it is unclear to what extent peel-off decomposition is hindered by possible errors during motor unit subtraction. With a careful removal process, the peel-off approach may ultimately be more efficient and consistent.

In this paper, a peel-off decomposition method for HDsEMG is presented, based on FastICA [23] and multiple new approaches, promoting efficiency and consistency. Density-based waveform clustering of peaks in the FastICA output was used to estimate motor unit spike trains with consistency across spikes. Surface MUAP distributions were estimated by compressed spike-triggered averaging. Compression by principal component analysis (PCA) was used to reduce noise in the surface MUAP estimates, while maintaining the proper shapes and amplitudes. Motor unit estimates were iteratively removed from the dataset in a peel-off manner, and a new reliability measure was used by comparing the variance of the FastICA source before and after peel-off. The method was validated by decomposing simulated data at different noise levels, and compared to the deflationary FastICA approach by Negro et al. [28]. Additionally, decomposition of experimental

data was done as well, with the deflationary FastICA approach as reference.

2. Method

2.1. Independent component analysis

Independent component analysis (ICA) provides an approximate solution to the general signal separation problem, in this case separating HDsEMG into constituent motor unit sources, under three assumptions [23]. In ICA terms; the underlying sources must be statistically independent, there must be more observations (e.g. recording electrodes) than sources, and the signal distribution of each source must be non-gaussian. For HDsEMG, the first assumption is true for many motor units due to differences in position, but it is difficult to prove for all motor units. The second assumption is a theoretical problem since the number of motor unit sources in HDsEMG recordings is unknown. However, this assumption mainly concerns simultaneous estimation of all sources, which can be circumvented by iterative algorithms that estimate one source at a time. In the third assumption of non-gaussian distributions lies the core of ICA. From the central limit theorem, a summation of two unique non-gaussian distributions will always be closer to a gaussian distribution. Reversely, non-gaussianity can therefore be used as a measure for independence [23].

In the standard ICA model, the observations, x, are defined as an instantaneous linear mixture of sources, s, with an invertible matrix, A.

$$x = As$$

A demixing matrix, W, returns an approximation of the sources, y, when applied to the observations.

$$y = Wx$$

The demixing matrix is iteratively estimated by maximizing for the independence of the output y, with a non-gaussianity measure.

2.1.1. Extension

Standard ICA regards all samples as separate and disregards their correlation to neighbouring samples [23]. A useful first step is therefore to extend the dataset, by adding copies of the original dataset with a delay, as additional channels.

$$x_{ext}(n) = [x(n),\ x(n-1),\ ..,\ x(n-M)]$$

Through extension, time features can be utilized by allowing a larger demixing matrix to not only account for single instances in time, but a series of samples correlated in time. Ultimately, the use of extension results in a significantly higher signal-to-noise ratio for the estimated independent components. The rationale behind extension is stated somewhat differently in other implementations such as the CKC method [18], where sources are modelled as pulse trains and extension allows for better compensation of impulse responses. Extension is, however, computationally very expensive and should be balanced with the benefits. Therefore, in this paper, extension is performed with 1 ms delays, regardless of sampling rate. This time delay is reasonable since it allows the algorithm to work consistently across different sampling rates while utilizing more of the MUAP signal at a lower computational cost. The optimal extension factor, i.e. the number of datasets in the extended dataset, for the proposed peel-off algorithm is identified in the evaluation section from analysis on synthetic data. A similar analysis is done for the reference deflationary method; however, an implementation of a time-based delay is not described for this method [28], which means the extension factors might not be directly comparable.

2.1.2. Whitening

The search space for the demixing matrix W is very large and is therefore reduced by a pre-processing step called whitening or sphering. The mean for each channel is subtracted and a whitening transform is applied to give the observations unit variance. A whitening matrix V can be calculated using the covariance matrix of the extended observations [23].

$$V = ED^{-1/2}E^T$$

$$z = Vx_{ext}$$

Here, E is a matrix of the unit-norm eigenvectors of the covariance matrix and D is the diagonal matrix of its eigenvalues. For the whitened data, z, the search space for maximizing independence is reduced to a single unitary rotation of the demixing matrix.

2.1.3. Negentropy

The ICA algorithm used in this paper searches for the demixing matrix by maximizing negentropy. Negentropy, J, is defined as the difference in entropy of the variable in question and a gaussian distributed variable of equal variance.

$$J(y) = H(y_{gauss}) - H(y)$$

In practice, negentropy is approximated sufficiently using gradient functions, and the following expression can be maximized instead [23].

$$J(y) \propto (E\{G(y)\} - E\{G(y_{gauss})\})^2$$

The gradient function, along with the first and second derivatives used here is the gaussian function.

$$G(y) = -\exp\left(-y^2/2\right)$$

$$g(y) = y \cdot \exp\left(-y^2/2\right)$$

$$g'(y) = \left(1 - y^2\right) \cdot \exp\left(-y^2/2\right)$$

The FastICA algorithm [23] is a fixed-point algorithm which iteratively updates the demixing matrix until it converges. Using the first and second derivatives of the gradient function, the demixing matrix is updated and normalized in each iteration. For the proposed peel-off approach, only a single source is estimated at a time.

$$w \leftarrow E\left\{zg\left(w^Tz\right)\right\} - E\left\{g'\left(w^Tz\right)\right\}w$$

$$w \leftarrow w/\|w\|$$

The demixing vector w can be initialized randomly, however, for better convergence properties, a starting vector is chosen here based on the input data. The FastICA output is then also deterministic, which makes analysis and comparison easier. Similar to Negro et al. [28], the time of highest power across all channels is extracted. The demixing vector is initialized as the inverse of the observations of the extended whitened data at this time. After converging, the final matrix gives a source estimate when applied to the whitened data z, which is locally the most independent.

2.2. Peel-off using compressed spike-triggered averaging

2.2.1. Peak detection & clustering

Peak detection is performed on the estimated source for samples over an amplitude threshold. Since FastICA outputs are normalized, the absolute values carry no useful information. However, it allows for a single static threshold to be consistent across different sources and iterations. From the estimated source, the time instance of each spike in the signal is extracted. The amplitude values in an approximately 4 millisecond long window around a spike

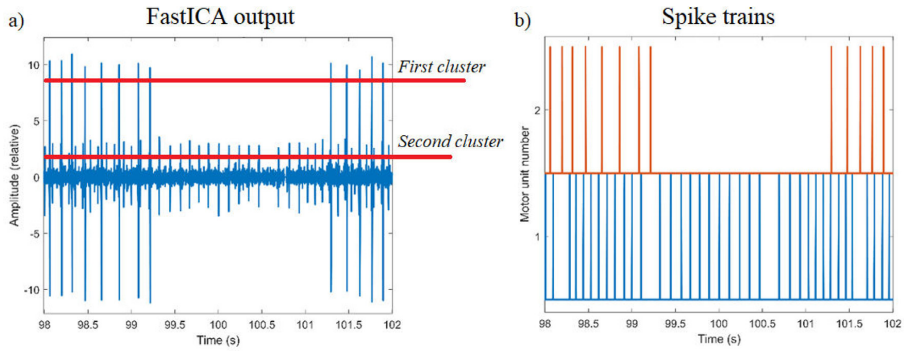

Fig. 1. a) A four second segment of a FastICA output is shown, which contains two distinct groups of spike amplitudes. Clustering of these spikes separates the groups from each other, potential outliers, and noise in the signal. b) The clustering output of the same four second segment, showing only the firing instances of the two estimated motor units.

are used as inputs to the density-based clustering algorithm (DBSCAN) [29]. The samples within each window are condensed to a single high-dimensional point, where each sample is considered a unique variable. In this manner, a more elaborate and consistent clustering of spikes is achieved, which accounts for a larger part of the waveform. Additionally, the density-based clustering method allows for an unspecified number of clusters, distinguishing between distinct groups and outliers, which is useful when more than one MU occupies the same source estimate (Fig. 1a).

The FastICA algorithm does not return meaningful morphological information of the underlying MUAPs, since a single source does not account for the entire convolutional mixture. However, since the FastICA output is a direct filtering result of the demixing vector applied to the dataset, it affects the entire signal uniformly. This means the peaks in the FastICA output should remain consistent for unique motor units across the signal, which justifies the waveform clustering approach. After clustering, however, only the time instances of each spike, i.e. the spike train, is kept, while the rest of the source signal is discarded. The resulting spike trains for each estimated motor unit are mostly zero, with sparse single values indicating when a firing has occurred (Fig. 1b). The full effect of a firing on the surface potential, the surface MUAP distribution, can then be estimated by spike-triggered averaging.

2.2.2. Spike-triggered averaging

With the assumption that the surface MUAP distribution of individual firings is relatively consistent in shape and size, they should not differ significantly from the average surface distribution. Spike-triggered averaging can therefore be used to recover the surface MUAP distribution from an estimated spike train. To perform spike-triggered averaging, data from a time window of approximately 16 milliseconds, centred around the firing instance of each spike found in the previous step, is extracted at every electrode. Calculating the average signal on every electrode result in an estimate of the surface potential distribution specific to that motor unit (Fig. 2). Since other motor units do not discharge simultaneously across most of the signal, they cancel out given enough firings. However, since there is often some residual noise in the surface MUAP distribution, a noise-reduction step is necessary before removing the motor unit to avoid disrupting the original signal.

2.2.3. PCA compression

Using PCA compression, the components accounting for the largest total variance are used to recreate the distribution, and components accounting for a smaller portion of the variance are removed. The surface MUAP affects all electrodes simultaneously, while noise in the estimated surface potential is random. There is no single component for random noise which accounts for a large portion of variance, and the noise is therefore quickly removed by compression. The surface MUAP distribution is largely unaffected by compression up to a certain point, as seen in Fig. 2 with a compression ratio of 16. However, the amount of compression is a parameter that needs to be tuned so the surface MUAP distributions are not affected. In this paper, compression down to four samples per channel is used to recreate surface distributions with considerable noise reduction.

2.2.4. Peel-off

During peel-off, the estimated surface MUAP distribution is removed from the dataset at the time instance of each firing in the spike train. This approach solves the problem where FastICA would otherwise continually converge on the same solution. It also circumvents the fact that estimated FastICA sources may not account for the entire convolutional mixture. By subtracting the spike-triggered average during peel-off, the entirety of the motor unit signal is affected. After removing the motor unit, the algorithm can be run again, iteratively revealing more motor units. The algorithm is summarized in Fig. 3.

The clustering method also separates and annotates outliers (noise points) from distinct groups. Outliers need to be removed to avoid converging on them in later iterations. The relevant samples are very few compared to the complete signal and can be dealt with in several ways. For example, the spikes can be replaced by gaussian distributed noise or attenuated by some factor. Both approaches remove the influence of outliers on the FastICA algorithm without severely impacting performance due to the small number of samples affected. For a deterministic output, attenuation of outliers by a factor of 100 is used in this paper.

2.2.5. Source variance

To gauge the credibility of a motor unit and its removal, the source can be analysed after the peel-off step. After the motor unit is removed, the demixing vector used to estimate the original source in the FastICA algorithm, can be re-applied to the updated dataset. This new source residual gives an indication of the consistency of the peel-off when compared to the original source. A large number of remaining spikes can suggest that multiple motor units were included in the estimate and could not be properly separated. This results in a higher variance in the new source residual after peel-off. On the other hand, a minimal number of remaining spikes reflect consistent peel-off and carries a lower total variance. Additionally, the variance of the original FastICA source,

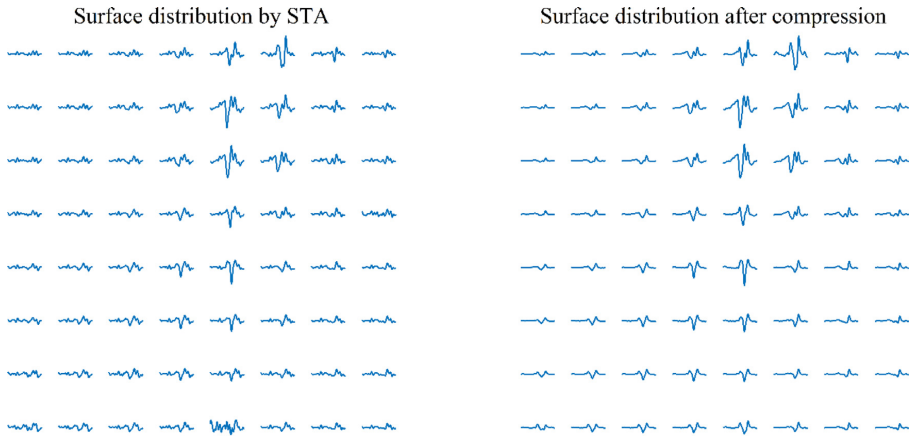

Fig. 2. The surface MUAP distribution is shown before compression (left) and after (right). PCA compression was performed on the surface distribution, recreating it from the largest principal components, at a compression ratio of 16. The noise reduction effect is particularly noticeable on noisy channels, and channels far away from the motor unit. The difference between the bottom rows of electrodes illustrates the effect clearly. The central surface MUAP distribution is largely unaffected as it accounts for the largest principal components.

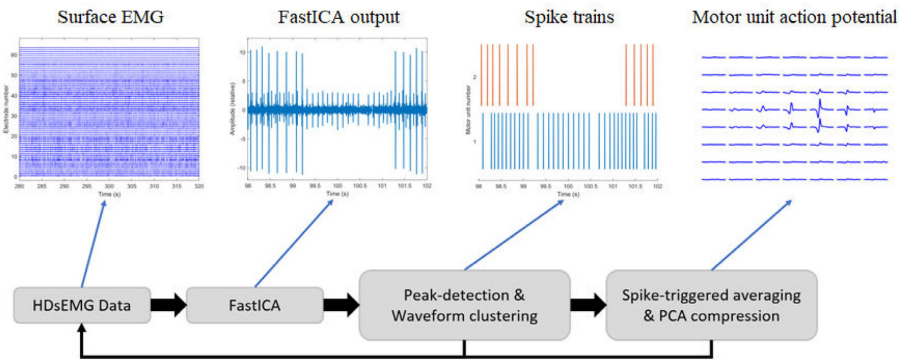

Fig. 3. Block diagram of the proposed peel-off method for decomposition of high-density surface EMG.

before peel-off, is normalized and always equal to one. A variance measure after peel-off can therefore be used as a generalized measure of credibility.

Fig. 4 illustrates the concept with examples of low and high variance. In the low variance example, the spikes are almost entirely removed, which suggests the peel-off step was consistent and accurate. In the high variance example, there are many small spikes left, which suggests an incomplete peel-off. In this case, it is possible that more than one motor unit signal is included in the original source estimate. An estimate with high variance after peel-off, should be scrutinized carefully since it is difficult to ascertain whether individual spikes where properly removed. By using a variance threshold, such estimates can be discarded or inspected manually in borderline cases. The optimal variance threshold is identified in the evaluation section from analysis on synthetic data.

2.3. Evaluation

In order to validate the proposed decomposition method for a large number of motor units with a known ground truth, a simulated dataset at different noise levels was used. This dataset was synthesized with a sampling rate of 2048 Hz using a reconstruction approach, where simulated spike trains were convolved with previously identified surface MUAP distributions. These MUAP distributions were obtained through decomposition of recorded HD-sEMG data using the deflationary approach described by Negro et al. [28] in the OTBiolab+ software (OT Bioelettronica, Torino, Italy). Furthermore, since assessment using real data is important, eight segments of the recorded datasets were used to compare the decomposition results of both methods.

2.3.1. Performance metric

Accuracy of identified motor units was measured on a per spike basis, using the same recall and precision metrics as Chen & Zhou [24]. In contrast to measures such as rate of agreement, with recall and precision, it is possible to extrapolate whether the estimates from the algorithm contain too many (low precision) or too few (low recall) firings.

$$Recall = \frac{TP}{TP + FN} = \frac{Matches}{All\ spikes}$$

$$Precision = \frac{TP}{TP + FP} = \frac{Matches}{Found\ spikes}$$

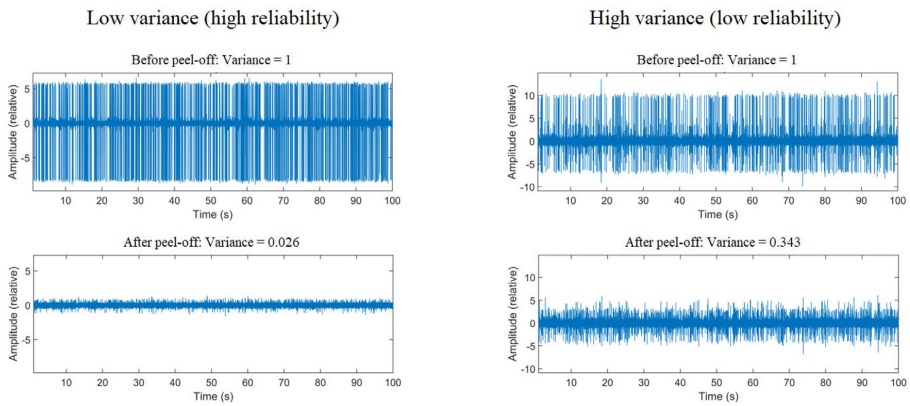

Fig. 4. The concept of different source variances is illustrated using simulated data. The same FastICA demixing vector is used generate the sources before (top) and after (bottom) peel-off. Before peel-off, the variance is normalized for both sources and there are many spikes in the FastICA output. After peel-off, in the low variance example (bottom left), all spikes are almost completely removed, whilst in the high variance example (bottom right), there is a substantial number of spikes left.

Where TP (true positives) is the number of matching spikes, FN (false negatives) is the number of missed spikes, and FP (false positives) is the number of spikes which do not match. In this paper, total recall refers to the number of matching spikes divided by the total number of existing spikes. Total precision refers to the number of matching spikes divided by the total number of identified spikes. Each true spike train is only matched with a single estimated spike train, regarding duplicate estimates as false positives. For the peel-off algorithm, the estimates were sorted by their variance measure and spikes of any duplicate estimate with higher variance were regarded as false positives. For the deflationary algorithm, since there was no variance measure available, the first estimate (lowest index) was used and spikes from any duplicate estimate were regarded as false positives. Matched recall and matched precision refer to the calculation on matching spike trains only, disregarding motor units not found and duplicate estimates respectively.

The dot product of two binary spike trains results in the number of matching spikes, if the spikes are perfectly temporally aligned. Since this is rarely the case, an offset of approximately 10 milliseconds, 20–100 samples depending on the sampling rate, was accounted for by first widening the spikes of the candidate spike train in each direction. The dot product between the candidate spike train and the true spike train produced the number of matches. A shorter offset window could have been used by first performing a time shift as done in other studies [24,30], however the difference in the number of matches was deemed insignificant since misattributing spikes for matching motor units is very rare due to the sparseness of the spike trains.

2.3.2. Data and setup

HDsEMG signals were gathered using arrays of 64 electrodes in an 8 × 8, both monopolar and differential, configuration with 1 cm interelectrode distance (OT Bioelecttronica model ELSCH064NM3), recorded at 2048 and 10,240 Hz, placed over the right forearm and upper arm on two right-handed and neurologically intact participants using a similar set-up as in [31]. The data was recorded using the OT Bioelettronica Quattrocento bioelectrical amplifier and OT BioLab+ v1.4.2 software (OT Bioelettronica, Torino, Italy) and all contraction were isometric. For the upper arm recordings, a weight of 1.9 kg was held statically in the hand with a 90-degree flexion of the elbow. For the forearm recordings, an isometric force-rig was used in conjunction with a LabVIEW program, which provided a protocol and visual feedback for contractions of the fingers [32]. The participants provided informed consent, and the study was approved by the Regional Ethical Review Board in Lund, Sweden (DNR 2017–297).

Decomposition was done using a deflationary approach by the Decomponi algorithm in the OT BioLab+ v1.5.2 software as described by Negro et al. [28]. The presented peel-off method was implemented in MATLAB R2020a (MathWorks, Natick, Massachusetts, USA). For the deflationary algorithm, the data was filtered with a bandpass filter between 5 and 500 Hz and a 50 Hz notch filter using the built-in features of OT BioLab+. For the peel-off algorithm, the data was similarly bandstop and bandpass filtered using zero-phase filtering in MATLAB. All of the data processing was performed on a benchtop computer with an AMD Ryzen Threadripper 3970X processor (32-cores) and 128 Gb of RAM.

2.3.3. Simulated data construction

From four unique datasets, containing recordings from both the forearm and upper arm, a total of 32 motor units found by the deflationary approach were selected for the simulated dataset. The surface MUAP distributions were obtained through spike-triggered averaging and downsampled to match the lowest sampling rate at 2048 Hz. The simulated spike trains were constructed by randomly assigning frequencies between 1 and 10 Hz, and subsequently randomizing all firings over 100 s. After convolving each surface MUAP distribution with a new spike train, gaussian noise was added to the data at three different levels, with a signal-to-noise ratio of 0, 10 and 20 dB.

3. Results

3.1. Simulated data decomposition results

Decomposition of 100 s of simulated data at 2048 Hz was performed at each noise level using the proposed peel-off algorithm, running for 60 iterations. The optimal variance threshold and extension factor was identified using a grid search on the synthetic dataset with a 10 dB signal-to-noise ratio (see Supplemental Figure S1). A variance threshold of 0.5 and an extension factor of 6 was chosen, after balancing both precision and recall performance. Each extended copy was delayed at 1 ms increments. With these parameters, at the noise levels 0, 10 and 20 dB, the peel-off algo-

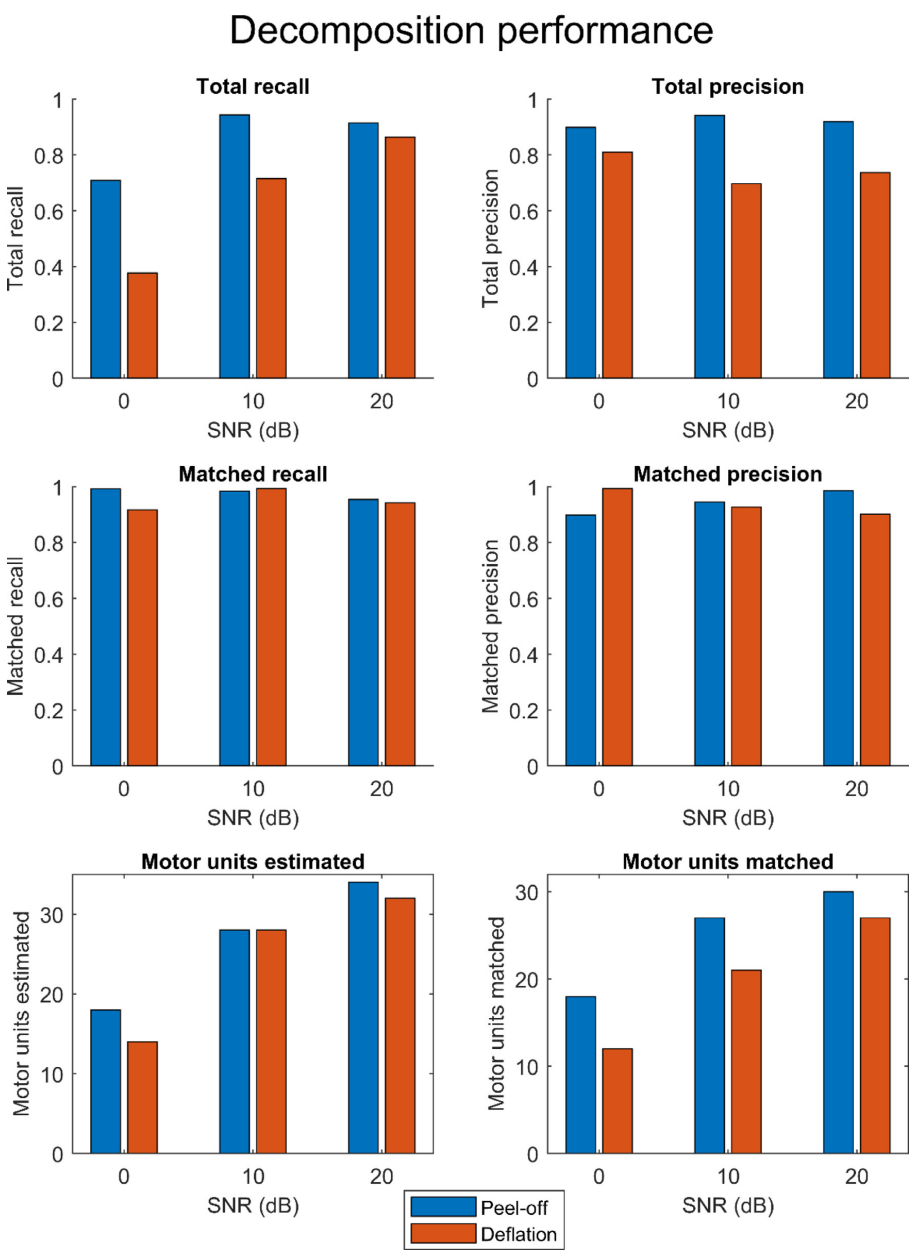

Fig. 5. A comparison of decomposition performance on simulated HDsEMG data at 2048 Hz for the proposed peel-off algorithm (blue) and the deflationary algorithm (red) is shown for three levels of signal-to-noise. Total recall refers to the number of matching spikes divided by the total number of existing spikes. Total precision refers to the number of matching spikes divided by the total number of identified spikes. Matched recall and matched precision refer to the calculation on matching spike trains only, disregarding motor units not found and duplicate estimates respectively.

rithm ran for 250, 190, and 150 s, and the accuracy is summarized in Fig. 5 (blue).

For the noise levels 0, 10, and 20 dB respectively: There were 18, 28, and 34 motor units estimated in total, with 18, 27 and 30 motor unit matches with the 32 existing motor units. The total recall was 71%, 94%, and 91% and the total precision was 90%, 94%, 92%. The matched recall was 99%, 98%, and 95% and the matched precision was 90%, 94%, and 99%.

The deflationary reference algorithm was run on the same 100 second segments for 250 iterations, which was the maximum

Table 1
The recall and precision performance of the proposed peel-off algorithm with respect to the deflationary algorithm is shown for 27 matching spike trains. The number of firings estimated by each algorithm, and the number of matches, are shown for each spike train. The matched recall and precision performance is calculated over the sum of all spikes.

Description		Spikes			Performance	
Segment	Number	Deflation	Peel-off	Matches	Recall	Precision
Index finger flexion 1	1	180	189	167	93%	88%
	2	53	47	46	87%	98%
	3	353	348	347	98%	100%
	4	75	54	53	71%	98%
	5	702	661	643	92%	97%
	6	782	759	738	94%	97%
	7	925	862	847	92%	98%
Index finger flexion 2	1	64	54	53	83%	98%
	2	351	336	334	95%	99%
	3	480	442	439	91%	99%
Index finger extension	1	513	540	513	100%	95%
	2	1002	1780	970	97%	54%
	3	767	844	756	99%	90%
	4	754	856	754	100%	88%
	5	664	759	656	99%	86%
	6	775	784	771	99%	98%
	7	713	1028	709	99%	69%
Middle finger flexion 1	1	88	72	71	81%	99%
	2	921	1627	862	94%	53%
	3	945	941	939	99%	100%
	4	871	894	866	99%	97%
Middle finger flexion 2	1	984	992	944	96%	95%
	2	1018	1092	1001	98%	92%
Middle finger extension	1	137	137	136	99%	99%
	2	909	928	897	99%	97%
Elbow flexion 1	1	1166	1156	1145	98%	99%
Elbow flexion 2	1	385	675	377	98%	56%
Total	27	16,577	18,857	16,034	97%	85%

number of iterations in the OT BioLab+ software. A similar grid search was performed for the optimal SIL threshold and extension factor in the deflationary algorithm on the synthetic dataset with 10 dB signal-to-noise ratio (see Supplemental Figure S2–3). An SIL threshold of 94 and an extension factor of 6 were chosen, after balancing both precision and recall performance. With these parameters, at the noise levels 0, 10 and 20 dB, the deflationary algorithm ran for 690, 540, and 430 s, and the accuracy is summarized in Fig. 5 (red).

For the noise levels 0, 10, and 20 dB respectively: There were 14, 28, and 32 motor units estimated in total, with 12, 21 and 27 motor unit matches with the 32 existing motor units. The total recall was 38%, 72%, and 86% and the total precision was 81%, 70%, and 74%. The matched recall was 92%, 99%, and 94% and the matched precision was 99%, 93%, and 90%.

3.2. Experimental data decomposition results

For the decomposition assessment using real data, six 80 second segments were selected from three recordings of the forearm at 10,240 Hz during contractions of the index and middle finger, and two 100 second segments were selected from two recordings of the upper arm at 2048 Hz during elbow flexion. Since the focus in this section was on evaluation of matching spike trains, manual inspection of decomposition results was done as well, discarding artifacts and estimates with less than 30 firings. The peel-off algorithm ran with the same parameters as for the simulated data, at a variance threshold of 0.5 and an extension factor of 6. For the deflationary reference algorithm, the SIL threshold was similarly set to 94. The extension factor was set to 6 for data at 2048 Hz, and to 32 for data at 10,240 Hz to accommodate the higher sampling rate.

Over all eight segments, a total of 33 spike trains were estimated with the deflationary algorithm and a total of 80 spike trains were estimated with the peel-off algorithm. Between the two algorithms, 27 spike trains matched, summarized in table 1. In order to compare the decomposition results, recall and precision of the peel-off algorithm was calculated with respect to the results of the deflationary algorithm, for each match and for all firings combined. The average matching recall was 97% and the average matching precision was 85%.

4. Discussion

In this paper, a method for decomposition of HDsEMG recordings has been presented, which builds on previous decomposition methods [18,20,24,28]. The compressed spike-triggered average from estimated spike trains were iteratively removed in a peel-off process, continually revealing more motor units. The method was evaluated using reconstructed synthetic HDsEMG at different noise levels and compared to the deflationary FastICA approach, described in [28]. Additionally, a comparison was made using experimental data.

For decomposition of simulated data, the new peel-off algorithm outperformed the deflationary algorithm regarding total recall and matching motor units found, especially at low signal-to-noise. The total precision was also higher for the peel-off algorithm, which was largely due to a higher number of duplicate estimates in the deflationary algorithm. When only considering matched motor units, both algorithms provide high recall and precision for all noise levels. These results suggest that the peel-off approach more efficiently avoids repeated convergence on the same motor units, without introducing a significant amount of noise or artifacts which would undermine reliability.

The computational time for the peel-off algorithm was also significantly less, however this largely depends on the number of iterations chosen. A large number of iterations was chosen for the deflationary algorithm to make sure the decomposition was as com-

plete as possible, prioritizing total recall and precision. Interestingly, the optimal extension factor for both algorithms was 6, even though the peel-off algorithm implemented extension with a time-based delay. It should be noted however, that the most optimal choice of parameters for the deflationary algorithm was not immediately clear (Supplemental Figure S2–3).

Further evaluation of the new peel-off method was performed using experimental data by calculating the matching recall and precision with respect to the deflationary algorithm. In contrast to other assessments such as rate of agreement, the recall and precision metrics provided more detailed information. A higher recall performance compared to precision, which was seen in this case, suggests that the peel-off algorithm could be more strict, by for example lowering the variance threshold. However, it could also mean that the deflationary algorithm missed discharges for the estimated motor units in question. Additionally, the number of motor unit estimates differed significantly, and more spike trains could have been estimated with the deflationary algorithm by applying a lower SIL threshold. However, the purpose of this part of the study was to assess reliability of discharges, with the deflationary algorithm as a substitute ground truth. Reliability of these estimates was therefore prioritized over the total number of estimates.

One of the main issues in decomposing muscle signals, is that motor units are not point sources, rather each source is spread out and the surface EMG signal shifts as the MUAP traverses the muscle fibres. A single estimate from ICA algorithms doesn't convey the complete motor unit, and hence, multiple versions of the same motor unit can be found. In typical deflationary FastICA, the search space of the demixing matrix is restricted during orthogonalization, to avoid repeated convergence. However, properly restricting the search space for all version of the same motor unit can be difficult. The strength of the peel-off approach is that the removal process directly affects each surface MUAP distribution in the HDsEMG signal. No matter which version of the motor unit is found, the peel-off step will affect the entire motor unit signal.

Density-based clustering of the FastICA output was performed by condensing multiple samples to a single high-dimensional point for each firing. This approach allowed for improved clustering of spikes, ensuring high consistency in each spike train. The chosen approach stands in contrast to a common choice of k-means clustering [20,28]. For the proposed algorithm, DBSCAN is preferred as the number of clusters is not predefined, and outliers are identified in addition to unique spike trains. If not dealt with, these outlier peaks interfere with the following iterations and may cause repeated convergence in the FastICA algorithm.

Before the peel-off step, PCA compression was performed on the surface MUAP, to reduce any noise in the spike-triggered average. The importance of this denoising step, is more pronounced for shorter signals or motor units with fewer firings, since less averaging takes place. If the average contains a large amount of noise, the risk of inducing a "phantom source" into the data or interfering with other sources is greater. With enough compression however, we err on the side of caution by removing less rather than more, ultimately minimizing the risk of interfering with subsequent iterations. Compression down to four samples per channel was empirically chosen by observing various noisy MUAP distributions. Although more optimized compression is likely possible, such a search was beyond the scope of this paper.

The new reliability measure provided in the proposed method compared the variance of the FastICA source before and after the peel-off step. It is an intuitive approach that effectively separated good estimates from poor ones. This is inherently different than the SIL measure in the deflationary algorithm, however they share the same underlying feature. Both measures are negatively affected by lower signal-to-noise ratio in the FastICA output. The selection of these thresholds was done by a grid search on one of the simulated datasets. It is possible that the optimal variance threshold (and SIL value) varies between datasets with different energies or noise levels. Inspecting borderline cases manually could in some cases improve the decomposition results.

4.1. Further research

Validation of decomposition methods is arguably the most important aspect in their development and is a thoroughly debated topic [33–36]. New algorithms and procedures for validation have also been presented in the literature [37,38]. Simulated data is a powerful tool in this regard. However, most simulated data do not take into account the effects of e.g. fatigue on the MUAP characteristics [39]. Simulated data needs to be complemented with experimental data to test applicability in a real scenario. To this end, we and others [28,40] think validation using simultaneous intramuscular and surface EMG recordings is important in order to obtain ground truth. Furthermore, to ensure the robustness of decomposition for varying motor unit characteristics, a wider range of muscles should be tested for as well. A limiting factor is that decomposition of HDsEMG is often biased towards superficial motor units, which may limit the scope of identifiable motor units. As such, future developments should aim to solve this issue. In addition, future studies should investigate the filtering choices during preprocessing. For example, a higher cut-off frequency for high-pass filtering would likely help to reduce the amount of superposition of motor units by shortening the tail ends of the MUAPs, perhaps at the cost of less distinguishable shapes.

5. Conclusion

A new peel-off algorithm was presented and validated on simulated HDsEMG data at three noise levels and compared to an established algorithm. The peel-off algorithm had significantly better performance regarding the total recall and total precision metrics for all tested noise levels, which demonstrates the utility of the method. The multiple new approaches in the algorithm include the use of density-based waveform clustering, PCA compression after spike-triggered averaging, and a variance measure before and after each motor unit estimate was subtracted. Future validation of the peel-off algorithm should focus on experimental data obtained from a wide range of muscles and on the cross-validation using simultaneous intramuscular and surface EMG recordings.

Declaration of competing interest

None declared.

Acknowledgements

This work was supported by the Promobilia Foundation, Stiftelsen för bistånd åt rörelsehindrade i Skåne and the Swedish Research Council (DNR 2019–05601). The study sponsors had no role in the study design, in the collection, analysis and interpretation of data; in the writing of the manuscript; or in the decision to submit the manuscript for publication.

Supplementary materials

Supplementary material associated with this article can be found, in the online version, at doi:10.1016/j.cmpb.2022.107250.

References

[1] E. Stålberg, B. Falck, The role of electromyography in neurology, Electroencephalogr. Clin. Neurophysiol. 103 (1997) 579–598.

[2] I. Vujaklija, D. Farina, O.C. Aszmann, New developments in prosthetic arm systems, Orthop. Res. Rev. 8 (2016) 31.
[3] M. Cifrek, V. Medved, S. Tonković, S. Ostojić, Surface EMG based muscle fatigue evaluation in biomechanics, Clin. Biomech. 24 (2009) 327–340.
[4] M.J. Zwarts, D.F. Stegeman, Multichannel surface EMG: basic aspects and clinical utility, Muscle Nerve 28 (2003) 1–17.
[5] R. Merletti, D. Farina, Analysis of intramuscular electromyogram signals, Philos. Trans. R. Soc. A 367 (2009) 357–368.
[6] X. Zhang, G. Zhu, M. Chen, X. Chen, X. Chen, P. Zhou, Muscle force estimation based on neural drive information from individual motor units, IEEE Trans. Neural Syst. Rehabilit. Eng. 28 (2020) 3148–3157.
[7] T. Kapelner, I. Vujaklija, N. Jiang, F. Negro, O.C. Aszmann, J. Principe, D. Farina, Predicting wrist kinematics from motor unit discharge timings for the control of active prostheses, J. Neuroeng. Rehabil. 16 (2019) 1–11.
[8] C. Chen, Y. Yu, X. Sheng, X. Zhu, Non-invasive analysis of motor unit activation during simultaneous and continuous wrist movements, IEEE J. Biomed. Health Inform. (2021).
[9] K. Østlie, I.M. Lesjø, R.J. Franklin, B. Garfelt, O.H. Skjeldal, P. Magnus, Prosthesis rejection in acquired major upper-limb amputees: a population-based survey, Disabil. Rehabilit. 7 (2012) 294–303.
[10] K.C. McGill, Z.C. Lateva, H.R. Marateb, EMGLAB: an interactive EMG decomposition program, J. Neurosci. Methods 149 (2005) 121–133.
[11] M. Nikolic, C. Krarup, EMGTools, an adaptive and versatile tool for detailed EMG analysis, IEEE Trans. Biomed. Eng. 58 (2010) 2707–2718.
[12] X. Ren, C. Zhang, X. Li, G. Yang, T. Potter, Y. Zhang, Intramuscular EMG decomposition basing on motor unit action potentials detection and superposition resolution, Front. Neurol. 9 (2018) 2.
[13] T. Yu, K. Akhmadeev, E.Le Carpentier, Y. Aoustin, D. Farina, On-line recursive decomposition of intramuscular EMG signals using GPU-implemented Bayesian filtering, IEEE Trans. Biomed. Eng. 67 (2019) 1806–1818.
[14] C.J. De Luca, A. Adam, R. Wotiz, L.D. Gilmore, S.H. Nawab, Decomposition of surface EMG signals, J. Neurophysiol. 96 (2006) 1646–1657.
[15] S.H. Nawab, S.-S. Chang, C.J. De Luca, High-yield decomposition of surface EMG signals, Clin. Neurophysiol. 121 (2010) 1602–1615.
[16] X. Hu, W.Z. Rymer, N.L. Suresh, Accuracy assessment of a surface electromyogram decomposition system in human first dorsal interosseus muscle, J. Neural Eng. 11 (2014) 026007.
[17] D. Zazula, A. Holobar, An approach to surface EMG decomposition based on higher-order cumulants, Comput. Methods Programs Biomed. 80 (2005) S51–S60.
[18] A. Holobar, D. Zazula, Multichannel blind source separation using convolution kernel compensation, IEEE Trans. Signal Process. 55 (2007) 4487–4496.
[19] A. Holobar, D. Zazula, Gradient convolution kernel compensation applied to surface electromyograms, in: International Conference on Independent Component Analysis and Signal Separation, Springer, 2007, pp. 617–624.
[20] Y. Ning, X. Zhu, S. Zhu, Y. Zhang, Surface EMG decomposition based on K-means clustering and convolution kernel compensation, IEEE J. Biomed. Health Inform. 19 (2014) 471–477.
[21] A.K. Clarke, S.F. Atashzar, A. Del Vecchio, D. Barsakcioglu, S. Muceli, P. Bentley, F. Urh, A. Holobar, D. Farina, Deep learning for robust decomposition of high–density surface EMG signals, IEEE Trans. Biomed. Eng. 68 (2020) 526–534.
[22] Y. Wen, S. Avrillon, J.C. Hernandez-Pavon, S.J. Kim, F. Hug, J.L. Pons, A convolutional neural network to identify motor units from high-density surface electromyography signals in real time, J. Neural Eng. 18 (2021) 056003.
[23] A. Hyvärinen, E. Oja, A fast fixed-point algorithm for independent component analysis, Neural Comput. 9 (1997) 1483–1492.
[24] M. Chen, P. Zhou, A novel framework based on FastICA for high density surface EMG decomposition, IEEE Trans. Neural Syst.Rehabilit. Eng. 24 (2015) 117–127.
[25] M. Chen, X. Zhang, X. Chen, P. Zhou, Automatic implementation of progressive FastICA peel-off for high density surface EMG decomposition, IEEE Trans. Neural Syst. Rehabilit. Eng. 26 (2017) 144–152.
[26] M. Chen, A. Holobar, X. Zhang, P. Zhou, Progressive FastICA peel-off and convolution kernel compensation demonstrate high agreement for high density surface EMG decomposition, Neural Plast. 2016 (2016).
[27] M. Chen, X. Zhang, P. Zhou, Automatic multichannel intramuscular electromyogram decomposition: progressive fastICA peel-off and performance validation, IEEE Trans. Neural Syst. Rehabilit. Eng. 27 (2018) 76–84.
[28] F. Negro, S. Muceli, A.M. Castronovo, A. Holobar, D. Farina, Multi-channel intramuscular and surface EMG decomposition by convolutive blind source separation, J. Neural Eng. 13 (2016) 026027.
[29] M. Ester, H.-P. Kriegel, J. Sander, X. Xu, A density-based algorithm for discovering clusters in large spatial databases with noise, kdd (1996) 226–231.
[30] C. Dai, X. Hu, Independent component analysis based algorithms for high-density electromyogram decomposition: systematic evaluation through simulation, Comput. Biol. Med. 109 (2019) 171–181.
[31] N. Malešević, A. Olsson, P. Sager, E. Andersson, C. Cipriani, M. Controzzi, A. Björkman, C. Antfolk, A database of high-density surface electromyogram signals comprising 65 isometric hand gestures, Sci. Data 8 (2021) 1–10.
[32] N. Malešević, G. Andersson, A. Björkman, M. Controzzi, C. Cipriani, C. Antfolk, Instrumented platform for assessment of isometric hand muscles contractions, Measur. Sci. Technol. 30 (2019) 065701.
[33] D. Farina, R.M. Enoka, Surface EMG decomposition requires an appropriate validation, J. Neurophysiol. 105 (2011) 981–982.
[34] C.J. De Luca, S.H. Nawab, Reply to Farina and Enoka: the reconstruct-and-test approach is the most appropriate validation for surface EMG signal decomposition to date, J. Neurophysiol. 105 (2011) 983–984.
[35] C.J. De Luca, S.H. Nawab, J.C. Kline, Clarification of methods used to validate surface EMG decomposition algorithms as described by Farina et al.(2014), J. Appl. Physiol. 118 (2015) 1084-1084.
[36] D. Farina, R. Merletti, R.M. Enoka, Reply to De Luca, Nawab, and Kline: the proposed method to validate surface EMG signal decomposition remains problematic, J. Appl. Physiol. 118 (2015) 1085-1085.
[37] F. Urh, A. Holobar, Automatic identification of individual motor unit firing accuracy from high-density surface electromyograms, IEEE Trans. Neural Syst. Rehabilit. Eng. 28 (2020) 419–426.
[38] T.J. Herda, M.E. Parra, J.D. Miller, A.J. Sterczala, M.R. Kelly, Measuring the accuracies of motor unit firing times and action potential waveforms derived from surface electromyographic decomposition, J. Electromyogr. Kinesiol. 52 (2020) 102421.
[39] G. Biagetti, P. Crippa, S. Orcioni, C. Turchetti, Homomorphic deconvolution for MUAP estimation from surface EMG signals, IEEE J. Biomed. Health Inform. 21 (2016) 328–338.
[40] M. Chen, X. Zhang, Z. Lu, X. Li, P. Zhou, Two-source validation of progressive FastICA peel-off for automatic surface EMG decomposition in human first dorsal interosseous muscle, Int. J. Neural Syst. 28 (2018) 1850019.

Paper II

Inferring position of motor units from high-density surface EMG

Lundsberg, J., Björkman, A., Malesevic, N., & Antfolk, C.

Published in: Scientific Reports, *14*(1), 3858, (2024)

scientific reports

Check for updates

OPEN

Inferring position of motor units from high-density surface EMG

Jonathan Lundsberg[1]✉, Anders Björkman[2], Nebojsa Malesevic[1] & Christian Antfolk[1]✉

The spatial distribution of muscle fibre activity is of interest in guiding therapy and assessing recovery of motor function following injuries of the peripheral or central nervous system. This paper presents a new method for stable estimation of motor unit territory centres from high-density surface electromyography (HDsEMG). This completely automatic process applies principal component compression and a rotatable Gaussian surface fit to motor unit action potential (MUAP) distributions to map the spatial distribution of motor unit activity. Each estimated position corresponds to the signal centre of the motor unit territory. Two subjects were used to test the method on forearm muscles, using two different approaches. With the first dataset, motor units were identified by decomposition of intramuscular EMG and the centre position of each motor unit territory was estimated from synchronized HDsEMG data. These positions were compared to the positions of the intramuscular fine wire electrodes with depth measured using ultrasound. With the second dataset, decomposition and motor unit localization was done directly on HDsEMG data, during specific muscle contractions. From the first dataset, the mean estimated depth of the motor unit centres were 8.7, 11.6, and 9.1 mm, with standard deviations 0.5, 0.1, and 1.3 mm, and the respective depths of the fine wire electrodes were 8.4, 15.8, and 9.1 mm. The second dataset generated distinct spatial distributions of motor unit activity which were used to identify the regions of different muscles of the forearm, in a 3-dimensional and projected 2-dimensional view. In conclusion, a method is presented which estimates motor unit centre positions from HDsEMG. The study demonstrates the shifting spatial distribution of muscle fibre activity between different efforts, which could be used to assess individual muscles on a motor unit level.

Keywords Electromyography, Motor unit depth, Motor unit spatial distribution, Motor unit localization

Mapping the distribution of motor unit activity is essential for understanding basic muscle neurophysiology. Motor units are the smallest functional parts of voluntary movement, consisting of a single motor neuron and the muscle fibres it innervates. These muscle fibre groups directly relay information from the nervous system. Peripheral or central nervous system injuries may therefore affect the distribution of motor unit activity in muscles. Tracking how motor unit activity is distributed could provide a quantifiable assessment of the severity of an injury and to what extent lost motor function is recovered, tools which are in high demand[1]. Furthermore, it could guide treatment of neuromuscular disorders such as spasticity[2]. The in vivo study of motor units is predominantly done with intramuscular and surface electromyography (EMG)[3–6]. More recent studies have explored motor unit imaging using ultrafast ultrasound[7], as well as a combination of ultrasound and EMG[8–11].

Intramuscular EMG (iEMG) provides high spatial selectivity and therefore reliable identification of motor units, which can be done either manually or through various algorithms[12–14]. Due to this high spatial selectivity of iEMG, the identified motor units are located close to the recording electrode. By knowing the position of the recording electrode, the position of the motor units is known as well. However, the high spatial selectivity and the invasive nature of the recording limit the ability of iEMG to simultaneously study many motor units. Thus, making it difficult to acquire a broader view of the distribution of motor unit activity since this would require a large number of intramuscular electrodes, which carries the risk of damage to muscle fibres, infection, as well as discomfort for the patient.

Ultrafast ultrasound is a promising alternative to iEMG, where decomposition of velocity images is used to single out individual motor units; a technique which directly identifies motor unit positions. However, decomposition of ultrafast ultrasound requires further validation, especially for many active motor units when higher

[1]Department of Biomedical Engineering, Faculty of Engineering, Lund University, Lund, Sweden. [2]Department of Hand Surgery, Institute of Clinical Sciences, Sahlgrenska Academy, University of Gothenburg and Sahlgrenska University Hospital, Gothenburg, Sweden. ✉email: jonathan.lundsberg@bme.lth.se; christian.antfolk@bme.lth.se

muscle force is used. An additional shortcoming of ultrafast ultrasound is the intense computational and data storage requirements for such measurement systems, which limits the duration of recordings.

Surface EMG (sEMG), on the other hand, is a well-studied non-invasive technique. In contrast to iEMG, electrodes on the skin surface need to be less spatially selective since they are further from the active muscle. Consequently, the signal is less discernible and the individual motor units cannot be identified manually. To compensate for this, high-density sEMG (HDsEMG) is used with more advanced signal separation techniques, in order to decompose the data into motor unit activity[15–18]. These decomposition techniques identify spike trains, which are the time instances of motor unit action potentials (MUAPs), from individual motor units. The MUAP is a compound signal of the synchronized single fibre action potentials of a motor unit firing. Thus, the contribution of each single fibre is not discernible with these techniques. Furthermore, the shape of individual MUAPs in a motor unit are not directly identified. Instead, each motor unit is represented by an average MUAP, generated using the identified spike train. The average contribution of all MUAPs from one motor unit to the recorded signal at each surface electrode is in this paper referred to as the surface MUAP distribution. Averaging the MUAP signals across each motor unit firing is referred to as spike-triggered averaging. The motor unit activity, however, is identified without positional information. Inferring motor unit positions from surface EMG therefore requires additional techniques.

Approaches to mapping muscle activity from sEMG have been proposed for many years using finite elements[19–21], which has been further used to study the motor unit distribution in stroke survivors[22]. A faster and simpler approach has also been proposed and iterated upon using an analytical volume conductor model, and a curve fit to the peak amplitudes of the surface MUAP distribution[23–28]. This curve fit approach estimates a motor unit's depth from the full width at half maximum (FWHM) of the surface potential peak amplitudes, perpendicular to an assumed muscle fibre direction. The FWHM, estimated with the spread of a Gaussian fit, has been shown to correlate with motor unit depth[23]. The motor unit depth and the point along the skin surface with the largest peak amplitude, in both the temporal and spatial domain, provide coordinates for each motor unit. Since MUAPs are compound signals from multiple single fibres, the estimated motor unit coordinates describe a centre point, with the largest peak amplitude, on an equivalent fibre that would generate the same potential distribution. The equivalent fibre's position is assumed to be a weighted sum of individual single fibre positions. However, distinctions are not made between different sets of weights or distributions of individual fibres, which is a limitation of the method. Furthermore, this curve fitting approach is done with a fit in one dimension[23–28], by placing the electrodes over the largest peak amplitude of the surface MUAP distribution perpendicular to the muscle fibre direction, which are both unknown prior to analysis of the signal. Thus, the coordinate along the fibre direction is unclear, and different fibre rotations from anatomical differences and muscle fibre pinnation may affect the depth estimate. Additionally, using a single linear array of electrodes makes the approach highly susceptible to noise at individual channels. HDsEMG may, however, solve these limitations with the additional information from a large number of channels.

The motor unit localization approach presented in this paper expands upon the original curve fit concept by using a two-dimensional elliptical Gaussian fit. This approach enables automatic localization of motor units with different surface amplitude peaks and fibre directions, as well as being robust to noise. In a pilot study, the presented method is first tested on a dataset of simultaneous intramuscular and surface EMG of the forearm, containing three intramuscular fine wire electrodes and an 8-by-8 surface electrode grid. Motor units are identified by decomposition of iEMG, with positions estimated from the synchronized HDsEMG data and compared to the positions of the fine wire electrodes, with depths measured using ultrasound. The presented method is then tested on a dataset consisting of only HDsEMG, using two adjacent 13-by-5 surface electrode grids. Motor units are identified by decomposition of HDsEMG, and the spatial distributions of motor units are qualitatively assessed for different efforts.

Methods

Data acquisition

Two separate tests of the method are presented with two participants. Simultaneous intramuscular and surface EMG was recorded with additional ultrasound images taken before the EMG recordings on the first participant, and only surface EMG was recorded on the second participant. Both participants were right-handed and neurologically intact. The participants provided informed consent, and the study was approved by the Regional Ethical Review Board in Lund, Sweden (DNR 2017-297). The motor unit localization method uses the shape of surface MUAP distributions across the skin to estimate motor unit positions. The identification of surface MUAP distributions is done differently for the two tests and thus separated in this section. The localization method is the same in both tests and thus presented in one section after the "Data acquisition" section.

Motor units from synchronized iEMG

For the first dataset, three intramuscular paired fine wire electrodes (0.051 mm in diameter stainless steel wires with 2 mm uninsulated ends, Chalgren, Gilroy, USA) were inserted into the right forearm of the participant with an insertion needle, targeting the following muscles: the extensor indicis proprius (EIP), extensor pollicis longus (EPL), and abductor pollicis longus (APL) (Fig. 1). At the time of insertion, the depths of the insertion needles were measured using an ultrasound machine (EPIQ 7, Phillips, The Netherlands with a linear transducer L18-5 at 9 MHz centre frequency). The insertion needles were measured because the fine wires electrodes were not visible on the ultrasound image. After the ultrasound measurements were performed, a HDsEMG electrode array, of 64 electrodes in an 8×8 differential configuration with 10 mm interelectrode distance (Model ELSCH064NM3, OT Bioelettronica, Torino, Italy), was placed on the skin on top of the intramuscular fine wire electrodes (Fig. 1). Differential signals were obtained by recording the difference between each electrode and

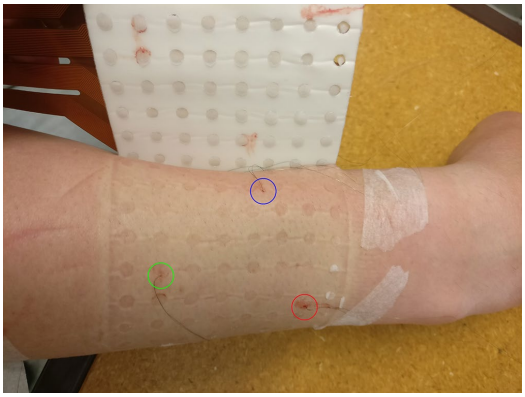

Figure 1. A post-measurement image showing the three fine wire electrodes inserted into the extensor indicis proprius (red circle), extensor pollicis longus (green circle), and abductor pollicis longus (blue circle) of the participant's posterior forearm. For illustrative purpose, the HDsEMG grid is elevated. During the recordings, this grid is placed on top of the forearm, covering the fine wire electrodes.

the following closest electrode in the grid in the proximal to distal direction. All EMG data were recorded at a sampling rate of 10,240 Hz, amplified 150 times, and analog bandpass filtered between 0.7 and 4400 Hz, with a 16-bit analog-to-digital converter (Quattrocento, OT Bioelettronica, Torino, Italy). The sampling rate and analog filtering was the same for iEMG and HDsEMG data as a result of recording simultaneously with the same system. However, this did not affect the data since further digital filtering would be applied to the HDsEMG data regardless. The efforts used for this recording were index finger flexion and extension, thumb flexion and extension, and thumb palmar adduction and abduction, corresponding to the muscles targeted with iEMG. The arm was placed in an isometric force rig[29] with 90-degree lateral rotation from the prone position, with visual force feedback displayed in a LabVIEW (National Instruments, Austin, Texas, USA) program as a guide for consistent finger muscle contractions. After determining the maximum voluntary contraction (MVC) force for each effort, the participant performed multiple isometric agonist–antagonist contractions by following a sinusoidal force curve (including both directions) with an amplitude of 20% MVC. See[29] for a detailed description. All forces were recorded concurrently with the EMG recordings, which enabled the selection of EMG data only when force was applied in the selected direction to minimize crosstalk from other muscles.

For this first test, motor unit spike trains were only identified from the iEMG data (fine wire electrodes), which had known positional references from the ultrasound measurements. Two-pass zero-phase filtering was performed on the iEMG data using a third order Butterworth notch filter with cutoff frequencies at 49 and 51 Hz, and bandpass filter with cutoff frequencies at 1 Hz and 2000 Hz. For the HDsEMG data, two-pass zero-phase filtering was performed using a third order Butterworth notch filter with cutoff frequencies at 49 and 51 Hz, and bandpass filter with cutoff frequencies at 5 Hz and 500 Hz. Motor unit spike trains were then identified from the filtered iEMG data by peak detection and high-dimensional density-based spatial clustering of peaks described in Ref.[18] with the DBSCAN algorithm[14]. The DBSCAN algorithm groups data points into clusters using a distance parameter and a minimum neighbours parameter. Data points with sufficient neighbours within the distance parameter are labelled as core points, and data points with too few neighbours but within range of a core point are labelled as edge points. Distinct groups of core points and edge points form separate clusters, and remaining data points not in range of any core points are labelled as outliers. As input to DBSCAN, a window of 100 samples (approximately 10 ms) was used as unique variables, generating a single high-dimensional data point, for each peak. The distance parameter, was set between 0.5 and 0.6 and the minimum neighbours parameter was set to 50. These parameters were chosen empirically, after manually optimizing the clustering for the smallest number of false positives. Spike trains were not identified for the HDsEMG data in this test. Instead, each spike train from the iEMG data was synchronized with the HDsEMG data, and spike-triggered averaging was used to calculate the surface MUAP distributions, later used for motor unit localization. The window size for spike-triggered averaging was 400 samples (approximately 40 ms).

Motor units from decomposition of HDsEMG

For the second dataset, two HDsEMG electrode arrays, both 64 electrodes in a 5×13 monopolar configuration with 8 mm interelectrode distance (Model ELSCH064NM2, OT Bioelettronica, Torino, Italy), were placed adjacently on the right forearm of the second participant, resulting in a 10×13 grid (Fig. 2). The efforts used for the second test were wrist extension, wrist extension with radial deviation, index finger extension, ring finger extension, little finger extension, thumb palmar abduction, and thumb palmar adduction. EMG data was recorded for 60 s for each effort at a sampling rate of 2048 Hz, amplified 150 times, and analog bandpass filtered between 0.7 and 900 Hz, with a 16-bit analog-to-digital converter (Quattrocento, OT Bioelettronica, Torino, Italy). The

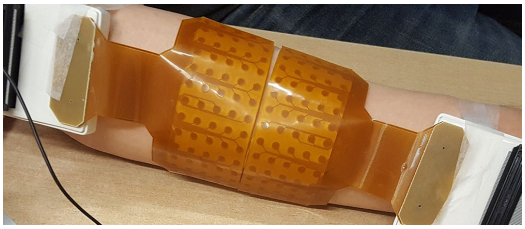

Figure 2. An image of two adjacent 13 × 5 electrode grids placed on the posterior side of the forearm.

forearm was in a prone position for all efforts except wrist extension with radial deviation, where the wrist was laterally rotated approximately 45° from the prone position, to isolate the extensor carpi radialis muscles. Isometric contractions were performed by applying a constant force to a vertically placed force gauge (Mark-10 model M5-20). Constant set force levels were used, at 1 N for finger and thumb contractions and 2 N for wrist contractions. At set force levels, the number of active motor units is assumed to be relatively consistent, which facilitates the comparison of the spatial distributions of motor unit activity between efforts. Using force levels at a percentage of MVC for each effort is commonly used to adjust for differences in muscle strengths. However, this test aims to distinguish the spatial distribution of motor unit activity between different wrist and finger contractions; and changing the force levels would introduce an additional factor to consider which affects the motor unit distribution. Thus, the force and number of motor units is kept as consistent as possible.

For this second test, motor units were identified by decomposition of the HDsEMG data, without known positional references. Two-pass zero-phase filtering was performed using a third order Butterworth notch filter with cutoff frequencies at 49 and 51 Hz, and bandpass filter with cutoff frequencies at 5 Hz and 500 Hz. The filtered HDsEMG data was decomposed with the iterative peel-off method described in Ref.[18]. This decomposition method estimates individual motor unit spike trains using the Fast Independent Component Analysis algorithm[30] while accounting for time structures by extending the dataset with delayed copies similar to other methods[15–17]. The spike-triggered average motor unit signal is removed from the HDsEMG dataset in each iteration[18], allowing iterative discovery of more motor units. Decomposition was run for 30 iterations with an extension factor of 6, each delayed by 2 samples, for each effort. Spike-triggered averaging then generated the surface MUAP distributions used for motor unit localization. Motor units were removed manually if their surface distributions were too medially or laterally positioned relative to the HDsEMG grid, since the surface fit applied in this method would not properly cover those areas. This positional requirement is a limitation of the current method to be considered.

Localization

The localization method presented in this section was applied principally in the same manner in both tests, with differing model parameters accounting for differences in forearm shape, electrode layout, and recording configuration. The positions of motor units were estimated using a Gaussian surface fit to the peak-to-peak amplitudes of the surface MUAP distribution (Fig. 3), for both differential signals (first test) and monopolar signals (second test). The surface MUAP amplitude is assumed to decay the fastest perpendicular to the muscle fibre direction from the electrode closest to the motor unit centre, and subsequently decays the slowest along the muscle fibre direction. As such, the surface MUAP distribution provides information on both the position and the fibre direction of each motor unit.

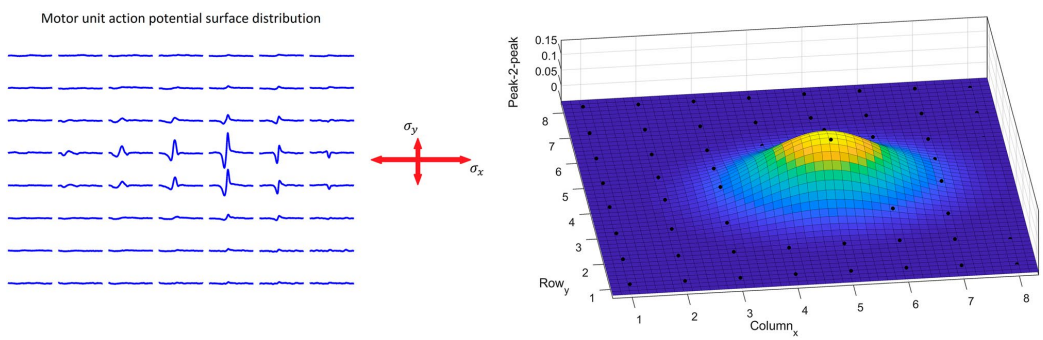

Figure 3. The localization method applies a general Gaussian surface fit to the peak-to-peak amplitudes of the surface MUAP distribution. The largest spread, σ_x, indicates the fibre direction, whilst σ_y indicates the spread perpendicular to the fibre direction, which relates to motor unit depth.

Principal component compression as noise reduction

As a pre-processing step, surface MUAP distributions were first smoothened by principal component compression. The estimated surface MUAP distributions occasionally contain residual noise, due to, e.g., errors in the original spike train, or from a low number of firings where spike-triggered averaging has not cancelled out all the noise. The idea of this step is that by choosing the amount of compression correctly, then mainly components for random noise are removed, while components for the surface MUAP amplitudes of interest remain[18]. In this paper, surface MUAP distributions were compressed down to a matrix of four samples per channel, by matrix multiplication with four eigenvectors of the covariance matrix corresponding to the four largest eigenvalues, and then resized with the transposed eigenvector matrix. The compression was important to ensure that noise at channels far from the motor unit would not dominate the lower amplitudes and subsequently impair the fitting process. Without compression, noise at these distant channels was found to often generate large errors for the surface fit, which would then converge poorly.

Gaussian surface fit

For a HDsEMG grid, each electrode's column and row define the variables x and y. However, the muscle fibres are not always aligned with the x and y axes of the electrode grid. In order to apply a Gaussian surface fit to the surface MUAP distribution, the potential offset can be accounted for by introducing a rotation angle. The generalized rotatable Gaussian function is derived by introducing a rotation matrix to the standard two-dimensional Gaussian function.

$$f(\hat{x},\hat{y}) = A \cdot \exp\left(-\left(\frac{(\hat{x}-\hat{x}_0)^2}{2\sigma_{\hat{x}}^2} + \frac{(\hat{y}-\hat{y}_0)^2}{2\sigma_{\hat{y}}^2}\right)\right), \tag{1}$$

$$\begin{bmatrix}\hat{x}\\ \hat{y}\end{bmatrix} = \begin{bmatrix}\cos\theta & -\sin\theta\\ \sin\theta & \cos\theta\end{bmatrix}\begin{bmatrix}x\\ y\end{bmatrix} = \begin{bmatrix}x\cos\theta - y\sin\theta\\ x\sin\theta + y\cos\theta\end{bmatrix}.$$

After simplification, resulting in

$$f(x,y) = A \cdot \exp\Big(-\Big(a(x-x_0)^2 + 2b(x-x_0)(y-y_0) + c(y-y_0)^2\Big)\Big), \tag{2}$$

$$a = \frac{\cos^2\theta}{2\sigma_{\hat{x}}^2} + \frac{\sin^2\theta}{2\sigma_{\hat{y}}^2},$$

$$b = -\frac{\sin 2\theta}{4\sigma_{\hat{x}}^2} + \frac{\sin 2\theta}{4\sigma_{\hat{y}}^2},$$

$$c = \frac{\sin^2\theta}{2\sigma_{\hat{x}}^2} + \frac{\cos^2\theta}{2\sigma_{\hat{y}}^2},$$

where A is the peak amplitude of the Gaussian function at the centre (x_0, y_0), with the spread (σ_x, σ_y) and rotation angle θ. These six coefficients are estimated by fitting the function to the peak-to-peak values of each electrode in the surface MUAP distribution, using least squares, with the curve fitting toolbox in MATLAB (MathWorks, Natick, Massachusetts, USA). Then, it is assumed that the largest spread of the distribution is along the fibre direction; and thus, the smallest σ defines the spread perpendicular to the fibre direction (Fig. 3). The spread perpendicular to the fibre direction and the rotation angle are then used to estimate the motor unit depth in a cylindrical volume conductor model.

Volume conductor model

The conductor model in this method is an analytical homogenous cylindrical single-layer model, which uses the Gaussian fit's amplitude centre, spread, and rotation to calculate the final motor unit position. Since the calculations are performed in the plane perpendicular to the fibre direction, the model is assumed to be isotropic. Although advanced multilayer conductor models have been developed[31,32], a single-layer model was used in this paper since additional layers were found to overcomplicate the method and generate too many unknown parameters. These choices are further explored in the discussion section.

Previous approaches have used a power function to model signal decay with increased distance[23], from the laws of electrostatics which assumes that the dynamics of the system are negligible. However, the MUAP signal is generated by the temporary displacement of ions and subsequent return flow to a neutral state, which is intuitively similar to the generation of waves. In this paper, signal strength, V, is instead modelled akin to attenuation of waves using Bouguer–Lambert–Beer's extinction law, where the amplitude decreases exponentially with distance, d, in an absorbing medium with a factor for attenuation strength, Q.

$$V = V_0 e^{-Qd}. \tag{3}$$

This model choice is justified both in terms of physical plausibility and ease of calculation. The exponential decay model assumes an internal starting amplitude, V_0, at the motor unit territory centre, where $d = 0$. A power function, such as d^{-Q}, grows infinitely for $d \to 0$, which makes it difficult to estimate an internal starting

amplitude. The exponential function provides similar decay properties to the power function, although it tends faster towards 0. Ultimately, both models are simplifications with different assumptions and could therefore both be viable. The attenuation strength is unknown, and the optimal value may differ between individuals, muscles, and recording configurations. A higher attenuation value ultimately produces deeper estimates of motor unit positions. However, a shift in attenuation strength offsets the estimates of all motor units and has only a minor impact on their relative position to other motor units. For the first test, Q was estimated post hoc, by calibrating for one of the three fine wire electrodes. The optimal value of Q was identified for motor units found in the iEMG signal in the APL muscle, producing a mean of $\mu_Q = 1.36$ with a standard deviation $\sigma_Q = 0.16$ from two motor units. Since the first dataset was recorded in a differential configuration, the same attenuation factor was not applicable to the second dataset recorded in a monopolar configuration. Due to the lack of ground truth, the attenuation factor for the second test was set to 1 for simplicity.

The ratio between the peak of the Gaussian distribution and the point at FWHM is, by definition, 2. From this, the depth of the motor unit, d, and radial distance to the surface position at half maximum surface potential, r_F, (Fig. 4) are related by

$$\frac{V_{max}}{V_{FWHM}} = \frac{V_0 e^{-Qd}}{V_0 e^{-Qr_F}} \Rightarrow \ln 2 = Q(r_F - d), \tag{4}$$

$$r_F = d + \ln 2/Q. \tag{5}$$

Roeleveld et al.[23] previously described the geometric relation between motor unit depth and radial distance. As a result of the cosine rule, a second expression for radial distance is generated, where the radial distance creates a triangle with the radius r, and $r - d$, with the opposing angle $\alpha = FWHM/2r$.

$$r_F{}^2 = r^2 + (r - d)^2 - 2r(r - d)\cos\alpha. \tag{6}$$

The FWHM relates to the spread of the Gaussian fit perpendicular to the fibre direction according to

$$FWHM = 2\sqrt{2\ln 2} \cdot \sigma. \tag{7}$$

After combining the two expressions for radial distance, the depth is directly calculated from

$$d = \frac{2r^2\cos\alpha - 2r^2 + (\ln 2/Q)^2}{2(r\cos\alpha - r - \ln 2/Q)}. \tag{8}$$

This, however, only applies to motor units where the fibre direction is aligned with the cylindrical model. For other fibre directions, the effective radius of the expression changes.

Effective radius

The radius of the cylinder was obtained by measuring the circumference of the forearm for both participants. The radius values were 48 mm for the first dataset, and 50 mm for the second dataset. For motor units with a rotation angle, θ, the radius value in Eqs. (6) and (8) increases, since the calculation is done perpendicular to the fibre direction in a cylindrical model. For example, in the extreme case with a fibre direction in the transverse plane of the cylinder, the depth is calculated with the surface amplitude distribution along the flat surface in the proximal to distal direction on the cylinder. Thus, the effective radius is the radius value used for calculation of motor unit depth, which increases with increased rotation angle. The measured radius, r, is related to the effective radius, r_{eff}, by making use of projections for two circle sectors, sharing the corner V_{max}. For a rotated fibre direction, imagine the circle sector spanning V_{max}, V_{FWHM}, and the centre point, with the two radii r_{eff} and the arc $FWHM/2$. The radius from the centre point to V_{FWHM} projects onto the other radius with the cosine of the angle given by the arc $FWHM/2$. This will be a common point, or depth, between the circle sectors, due to the cylindrical shape of the model. The second circle sector is perpendicular to the cylinder direction and makes use of the measured radius, r, and the corner V_{max}. For this second circle sector, the projection of the radii lands on the common point, or depth, when the arc is $FWHM/2 \cdot \cos\theta$. The distance between the common point and V_{max} in these two cases generate the equation

$$r - r\cos\alpha = r_{eff} - r_{eff}\cos\beta, \tag{9}$$

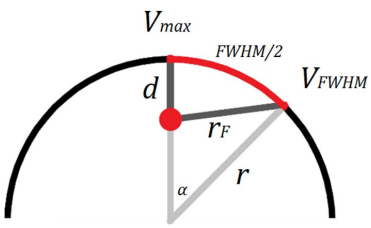

Figure 4. An illustration of the geometry and values used in the model to estimate motor unit depth.

$$\alpha = \frac{FWHM \cdot \cos\theta}{2r}, \beta = \frac{FWHM}{2r_{eff}}.$$

By approximation of the cosine function, we get a simplified equation for the effective radius.

$$\cos x \approx 1 - x^2/2, \tag{10}$$

$$\Rightarrow r - r\left(1 - \frac{FWHM^2\cos^2\theta}{8r^2}\right) = r_{eff} - r_{eff}\left(1 - \frac{FWHM^2}{8r_{eff}^2}\right), \tag{11}$$

$$r_{eff} = r/\cos^2\theta. \tag{12}$$

With the surface fit parameters, the estimated attenuation strength, and the effective radius value, the centre position of each motor unit is estimated. While the spread of the surface fit perpendicular to the fibre direction informs motor unit depth, the spread along the fibre direction could conceivably inform motor unit fibre length. However, this possibility is not explored in this paper. Instead, fibre lengths are plotted as half the spread along the fibre direction, for visualization purposes only.

Ethics approval and consent to participate

The study was approved by the Regional Ethical Review Board in Lund, Sweden (DNR 2017-297) and was conducted in accordance with the tenets of the Declaration of Helsinki. All participants were informed about the contents of the experiments, both verbally and in writing, and gave their informed and written consent.

Results

Motor units from synchronized iEMG

From the three intramuscular fine wire electrodes in the first participant, a total of 7 motor units were identified and temporally matched with the HDsEMG data, generating 7 surface MUAP distributions. From these surface MUAP distributions, the estimated depth of each motor unit is shown in Table 1 and grouped by muscle in a boxplot in Fig. 5. The depth of the needles inserting the intramuscular fine wire electrodes were 8.4, 15.8, and 9.1 mm for the extensor indicis proprius (EIP), extensor pollicis longus (EPL), and abductor pollicis longus (APL) respectively. The mean estimated depth for motor units from each wire was 8.7, 11.6, and 9.1 mm, with standard deviations 0.5, 0.1, and 1.3 mm, for the EIP, EPL, and APL, respectively. The resolution of these estimates is further addressed in the discussion section. Visualization of the motor unit positions in 3D is shown in Fig. 6, alongside a projection of the motor unit centres onto the transverse plane. The motor units are clearly localized to the insertion points on the skin surface (seen in Fig. 1). However, the difference in estimated motor unit depth between the muscles of the participant was not as large as the difference between the insertion depths of the fine wire electrodes measured by ultrasound. Thus, it is possible that the model underestimates differences in depth. It may also be the result of the displacement of muscles under tension, or a displacement of the fine wire electrodes after insertion. While these estimated differences were less than in the ultrasound reference, motor units from the EPL muscle still produced the deepest estimates (Fig. 5). For one-tailed two-sample t-tests, the mean motor unit depth of the EPL muscle was 2.8 mm greater than the EIP muscle with $p = 0.001$, and 2.5 mm greater than the APL muscle with $p = 0.018$. After Bonferroni correction for multiple comparisons is applied to these values, the results are significant at the $\alpha = 0.01$ and $\alpha = 0.05$ levels respectively. However, strong conclusions from statistical analysis should be avoided, due to the low number of motor units in the test which limits this study.

Motor units from decomposition of HDsEMG

From HDsEMG decomposition of the seven different efforts, a total of 79 motor units were identified. After discarding 14 motor units that were too far outside the bounds of the HDsEMG grids, the remaining 65 motor units were used for the localization method (Table 2). Visualization of the motor unit positions in 3D is shown in Fig. 7, alongside a projection of the motor unit centres onto the transverse plane. To aid analysis, the seven efforts were grouped into wrist efforts, finger efforts, and thumb efforts. For wrist extension there were two clear

Muscle	Motor unit depth (mm)	Insertion needle depth (mm)
EIP	9.1	8.4
	8.4	
EPL	11.5	15.8
	11.5	
	11.7	
APL	8.2	9.1
	10	

Table 1. The estimated depth of motor units from surface MUAP distributions, identified by temporally matching iEMG and HDsEMG data from one participant. The two motor units from the APL were used as calibration points for the attenuation factor of the model.

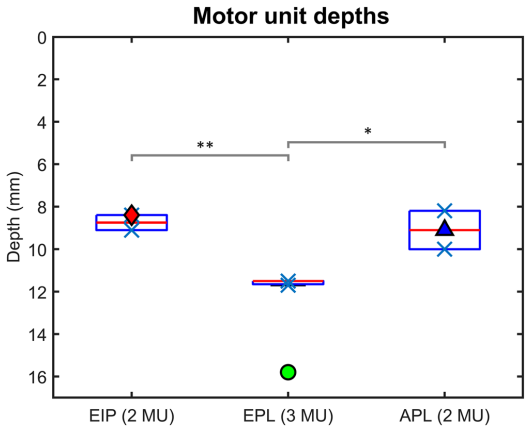

Figure 5. A boxplot of the estimated depths, grouped by muscle, from 7 surface MUAP distributions from one participant. The blue crosses indicate the estimated depth of each motor unit centre. The motor units were first identified with iEMG, then temporally matched with the HDsEMG data. The red, green, and blue shapes represent the depth of each fine wire insertion needle, measured by ultrasound. One and two asterisks indicate a significant difference at $\alpha = 0.05$ and $\alpha = 0.01$ respectively. The blue triangle overlaps with the red median line for motor units from the APL since the two motor units from this fine wire electrode were used to estimate the attenuation factor of the model.

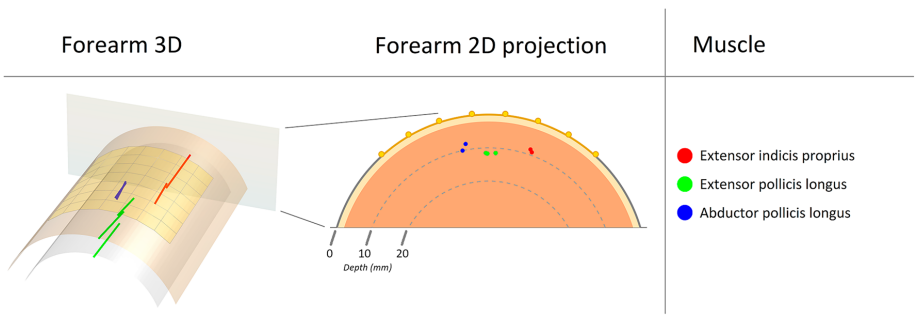

Figure 6. The left figure shows the visualization of 7 motor units in 3D in a cylindrical model. The top surface represents the skin and the electrode grid, and the underlying concentric layer indicate 10 mm depth. A projection onto the transverse plane is shown in the right figure where 10- and 20-mm depths are marked. The yellow layer illustrates subcutaneous fat; however, this distinction is not included in the model. The motor unit centres, indicated by coloured dots, were identified from iEMG and their positions estimated from synchronized HDsEMG data, for the extensor indicis proprius (red), extensor pollicis longus (green), and abductor pollicis longus (blue), in the right forearm of the participant.

Effort	Motor units	Force (N)
Wrist extension	15	2
Wrist extension with radial deviation	6	2
Index finger extension	9	1
Ring finger extension	7	1
Little finger extension	7	1
Thumb palmar abduction	11	− 1
Thumb palmar adduction	10	1

Table 2. The number of identified motor units and the vertical upward force applied to the force gauge for each of the 7 efforts.

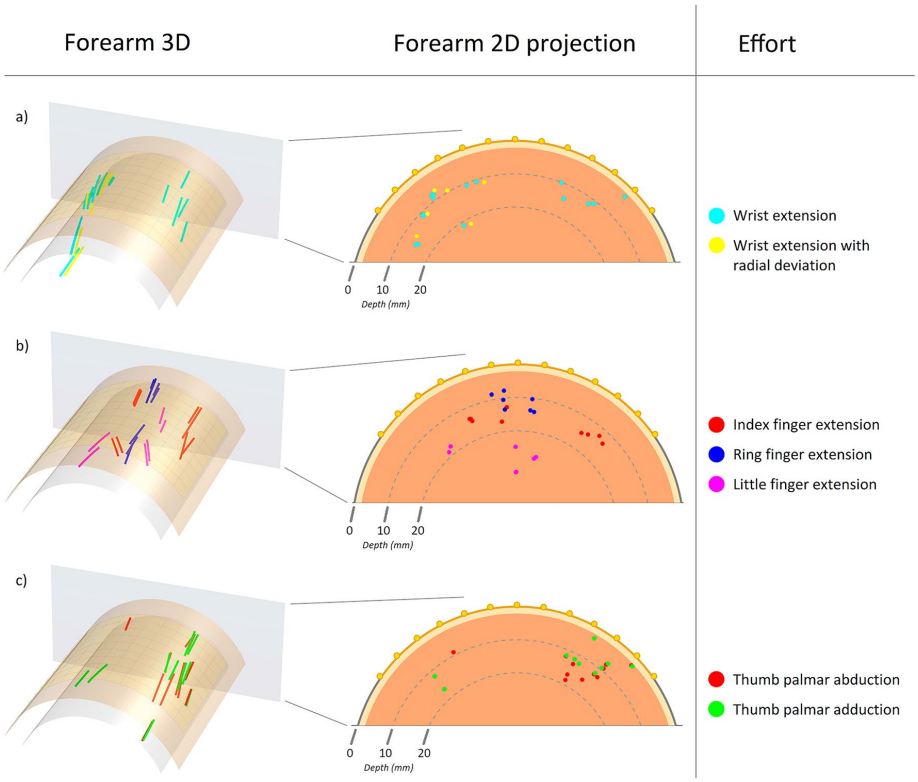

Figure 7. The figures in the left column show the visualization of motor units in 3D in a cylindrical model. The top surface represents the skin and the electrode grid, and the underlying layer indicate 10 mm depth. A projection onto the transverse plane is shown in the right column where 10- and 20-mm depths are marked. The yellow layer illustrates subcutaneous fat; however, this distinction is not included in the model. The motor unit centres, indicated by coloured dots, were identified by decomposition of HDsEMG for 7 separate efforts. The results are grouped into wrist extensions (**a**), finger extensions (**b**), and thumb efforts (**c**) to aid analysis.

areas of motor unit activity, at the radial and ulnar edges of the grid, which provides a preliminary suggestion that these are the areas of the extensor carpi radialis brevis or longus (ECRB and ECRL) and the extensor carpi ulnaris (ECU) respectively (Fig. 7a). When wrist extension was performed with radial deviation, the motor unit activity on the ulnar side disappeared, which suggests that an isolated contraction with the ECR muscles was successfully made. Additionally, the direction of these radial fibres aligns with the expected anatomy of the ECR muscles, as seen in the 3D plot. For finger extensions, the motor unit activity was mainly identified in between the previous estimates of the ECR muscles and the ECU muscle, suggesting this is the area of the extensor digitorum communis muscle (Fig. 7b). However, additional activity on the ulnar side can be seen for index finger extension, which overlaps with the previous estimate of the ECU muscle, which may indicate some amount of stabilizing synergistic contraction. The estimates for little finger extension are less convincing due to their pronounced depth. This depth could be the result of either displacement of the muscles under tension, synergistic contractions of the deeper abductor and extensor pollicis longus muscles (APL and EPL), or an error in the depth estimates specific to these motor units. For thumb efforts, the activity distributions were the least conclusive (Fig. 7c). The large amount of overlapping activity on the ulnar side for both thumb palmar abduction and adduction suggests that these are not motor units of the APL or EPL muscles but could instead be stabilizing contractions of the wrist. Further tests across the forearm are needed to identify the area of, e.g., abductor pollicis longus.

Discussion

In this study, a new automatic method was developed for non-invasive estimation of motor unit positions, consisting of principal component compression and a custom surface fit applied to peak-to-peak amplitudes of surface MUAP distributions, as well as a volume conductor model with exponential signal attenuation. Surface MUAP distributions have been thoroughly studied[23,24,28,33,34], demonstrating the relationship between motor unit depth and the FWHM of the amplitudes of the surface MUAP distribution. Thus, this paper focuses on providing

a method which improves upon previous methods[23–27]. The new method presented in this paper is automatic and carries a very low computational load, in contrast to, e.g., finite element methods[19–21]. This enables the estimation of a large number of motor units, required for properly mapping the spatial distribution of motor unit activity. However, it is limited to motor units within the confines of the HDsEMG grid. For end applications, it is furthermore important to consider the limitations of decomposition algorithms, and the number of motor units which can reliably be identified. The new method is flexible as it is applicable to different motor unit positions and fibre directions. This was exemplified by the wrist extensions in the second test (Fig. 7a), which demonstrated the methods ability to identify the slightly diagonal direction of the ECR muscles. In contrast, previous studies used linear arrays of electrodes or selected a single column of electrodes from a grid manually[22–27,33,35], which requires prior knowledge of motor unit positions and fibre directions for correct estimations.

A method was recently proposed with generalized electrode placements which identifies surface amplitude maps and the centre of gravity of surface MUAP distributions, using normalized peak-to-peak values, generated via spike-triggered averaging on a monopolar HDsEMG grid[36]. However, their method only identifies motor unit positions at the surface and does not include the depth of motor units. Still, this centre of gravity approach highlights the potential asymmetries in surface MUAP distributions when contrasted with the peak amplitude centre. The Gaussian fit is rigid in this regard, and accounting for such asymmetries is a potential next step in improving the method presented in this paper. Furthermore, asymmetries in the surface MUAP distribution could perhaps be used inform fibre rotation in the depth direction. Better models and estimates for fibre length should also be explored by making use of, e.g., the spread along the fibre direction.

The stability of motor unit estimates is improved by using a grid of electrodes, rather than a linear array. Due to the high number of electrodes, the method is less affected by individual poor channels, improving stability. Furthermore, principal component compression reduces possible residual noise after spike-triggered averaging. This ensures that the Gaussian fit is applied only to the surface MUAP signal, reducing the risk of converging on poor local minima determined by residual noise. In addition, the presented method includes a new correction for the effective radius of a cylindrical model for fibre directions at an angle. However, the extent to which this correction affects the results was not determined and should be studied further.

The placement of the HDsEMG grid is very important, as was seen in both tests. In the first test, the surface MUAP distributions of the EIP were close to the distal edge of the grid, which may impact the accuracy of the Gaussian fit. In the second test, it is possible that the APL and EPL muscles were too distal in relation to the grids to be easily detected, which could explain the resulting motor unit distributions (Fig. 7c). Future studies should ensure full coverage of the muscles by targeting muscles closer together or using a larger array.

Furthermore, the recording configuration affects the surface MUAP distribution and thus the estimated FWHM[23,33]. For differential recordings, the surface MUAP distribution sometimes contains a row of low amplitudes where the MUAP signal shifts from increasing to decreasing amplitude. This occurs when the peak amplitude of the motor unit signal lies in the middle between two electrodes. The electrodes are then affected equally by the MUAP, resulting in a low differential signal between them. This may negatively affect the Gaussian fit and increases the risk of converging on an erroneous local minimum. A monopolar configuration might therefore be more suitable for this method. Monopolar surface MUAP distributions generally provide larger FWHM values[23,33], which results in deeper motor unit estimates. Thus, a smaller attenuation factor may be used to compensate for this effect. Whether depth discrimination between motor units is affected should be studied further. Additionally, depth estimates could be affected by the size of the motor unit territories. A larger spread of neuromuscular junctions may result in a larger FWHM, which could be conflated with increased depth.

The estimation of the attenuation factor in the conductor model is one of the main limitations of the current method. In the first test, an attenuation factor was identified by calibrating for one of three fine wire electrodes. This value may not be generalizable to other muscle groups or individuals. Since the forearm contains many closely packed muscles, it presents a good test for localization and muscle discrimination. However, future studies should include a range of muscle groups and many subjects. Furthermore, the depth values in this paper are reported with 0.1 mm resolution. This choice was made due to the small differences in depth estimates for the motor units from the EPL muscle, resulting in a standard deviation of 0.1 mm. However, it is important to note that more data is required to properly determine the precision of the method. Additionally, while the positions of the insertion needles were precisely obtained from ultrasound images, it is not known to what extent the fine wire electrodes move after insertion. Using ultrasound with better resolution to identify the position of the fine wire electrodes after removing the insertion needle would greatly improve the reliability of iEMG as reference points. Conceivably, iEMG could be used once per patient in future applications to determine the attenuation factor, with subsequent recordings done with only HDsEMG. The use of iEMG, however, is preferably avoided due to patient discomfort.

The choice of conductor model, with an exponential attenuation instead of a power function, was briefly motivated in "Volume conductor model" section but should be explored further. The Bouger–Lambert–Beer's extinction law used in this study is an empirical law concerning the attenuation of light through a material. We model the MUAP as a voltage source, generating an electromagnetic wave, propagating through the tissue. However, since the fluctuations of the potential field from the flow of ions is relatively slow, the application of the extinction law may be limited. A power function derived from electrostatic laws could still be a better model for MUAP amplitudes, which is a potential limitation of this study. However, neither an exponential nor a power function is a complete description of the MUAP source, as cylindrical muscle fibres. Due to the high degree of simplification, validity is difficult to assess from a theoretical point. As such, we argue that performances should be assessed and compared for multiple models in an end application. While a power function may work well to describe potential amplitudes along the skin surface, it is difficult to generate estimates for an internal starting amplitude, since the distance in these functions cannot be set to zero, unlike in the exponential function. Such internal estimates were not done in this study. A future study could therefore explore this, by comparing the

internal estimate from surface EMG, V_0 in Eq. (3), with intramuscular EMG at a known depth. The thickness of the subcutaneous layer varies across muscle groups and should be studied to determine whether it affects the estimates enough to limit the utility of the method. Since the conductor model in this paper is only a single-layer model, the properties of the different layers are approximated to a single attenuation factor. More complex multilayered models[31,32] could hypothetically provide better depth discrimination between motor units across muscle groups, by making use of more parameters. However, it is also possible that shifting the attenuation factor in a single-layer model can sufficiently account for varying thicknesses of the subcutaneous layers, which should be explored. The advantage of the single-layer model is in the simplicity of implementation and would be the preferred choice if viable. Furthermore, the calculations assume that the muscle is isotropic in the cross-sectional plane. The isotropic assumption is only made in the plane perpendicular to the fibre direction, since the length of the surface MUAP distribution in the fibre direction is not used for depth estimation. It is possible that the conductivity along the fibre direction could influence the distribution width as well, however, this effect was not assessed and assumed to be negligible.

Conclusion

A new automatic method for position estimation of motor units has been presented, based on a rotatable Gaussian surface fit applied to surface MUAP distributions. The method is tested using simultaneous iEMG and HDsEMG as well as only HDsEMG. The method provided distinct areas of activity associated with different muscles and demonstrated the shifting spatial distribution of motor unit activity between different efforts. This information could be used to aid non-invasive assessments of individual muscles on a motor unit level.

Data availability

The datasets used and/or analysed during the current study are available from the corresponding author on reasonable request.

Received: 23 August 2023; Accepted: 12 February 2024
Published online: 15 February 2024

References

1. Richards, C. L., Malouin, F. & Nadeau, S. Stroke rehabilitation: Clinical picture, assessment, and therapeutic challenge. *Prog. Brain Res.* **218**, 253–280 (2015).
2. Wissel, J. *et al.* Management of spasticity associated pain with botulinum toxin A. *J. Pain Sympt. Manag.* **20**, 44–49 (2000).
3. Martinez-Valdes, E. *et al.* Tracking motor units longitudinally across experimental sessions with high-density surface electromyography. *J. Physiol.* **595**, 1479–1496 (2017).
4. Del Vecchio, A., Negro, F., Felici, F. & Farina, D. Associations between motor unit action potential parameters and surface EMG features. *J. Appl. Physiol.* **123**, 835–843 (2017).
5. Zwarts, M. J. & Stegeman, D. F. Multichannel surface EMG: Basic aspects and clinical utility. *Muscle Nerve* **28**, 1–17 (2003).
6. Merletti, R. & Farina, D. Analysis of intramuscular electromyogram signals. *Philos. Trans. R. Soc. A Math. Phys. Eng. Sci.* **367**, 357–368 (2009).
7. Rohlén, R., Stålberg, E., Stöverud, K.-H., Yu, J. & Grönlund, C. A method for identification of mechanical response of motor units in skeletal muscle voluntary contractions using ultrafast ultrasound imaging—Simulations and experimental tests. *IEEE Access* **8**, 50299–50311 (2020).
8. Waasdorp, R. *et al.* Combining ultrafast ultrasound and high-density EMG to assess local electromechanical muscle dynamics: A feasibility study. *IEEE Access* **9**, 45277–45288 (2021).
9. Carbonaro, M. *et al.* Physical and electrophysiological motor unit characteristics are revealed with simultaneous high-density electromyography and ultrafast ultrasound imaging. *Sci. Rep.* **12**, 1–14 (2022).
10. Lubel, E. *et al.* Kinematics of individual muscle units in natural contractions measured in vivo using ultrafast ultrasound. *J. Neural Eng.* **19**, 056005 (2022).
11. Rohlén, R., Stålberg, E. & Grönlund, C. Identification of single motor units in skeletal muscle under low force isometric voluntary contractions using ultrafast ultrasound. *Sci. Rep.* **10**, 1–11 (2020).
12. McGill, K. C., Lateva, Z. C. & Marateb, H. R. EMGLAB: An interactive EMG decomposition program. *J. Neurosci. Methods* **149**, 121–133 (2005).
13. Nikolic, M. & Krarup, C. EMGTools, an adaptive and versatile tool for detailed EMG analysis. *IEEE Trans. Biomed. Eng.* **58**, 2707–2718 (2010).
14. Ester, M., Kriegel, H.-P., Sander, J. & Xu, X. A density-based algorithm for discovering clusters in large spatial databases with noise. In *Proc. Second International Conference on Knowledge Discovery and Data Mining* 226–231.
15. Holobar, A. & Zazula, D. Multichannel blind source separation using convolution kernel compensation. *IEEE Trans. Signal Process.* **55**, 4487–4496 (2007).
16. Chen, M. & Zhou, P. A novel framework based on FastICA for high density surface EMG decomposition. *IEEE Trans. Neural Syst. Rehabil. Eng.* **24**, 117–127 (2015).
17. Negro, F., Muceli, S., Castronovo, A. M., Holobar, A. & Farina, D. Multi-channel intramuscular and surface EMG decomposition by convolutive blind source separation. *J. Neural Eng.* **13**, 026027 (2016).
18. Lundsberg, J., Björkman, A., Malesevic, N. & Antfolk, C. Compressed spike-triggered averaging in iterative decomposition of surface EMG. *Comput. Methods Progr. Biomed.* **228**, 107250 (2022).
19. Jesinger, R. A. & Stonick, V. L. Processing signals from surface electrode arrays for noninvasive 3D mapping of muscle activity. In *Proc. IEEE 6th Digital Signal Processing Workshop* 57–60 (IEEE).
20. Zhang, Y., Wang, D. & Timm, G. W. A three-dimensional muscle activity imaging technique for assessing pelvic muscle function. *Inverse Probl.* **26**, 115018 (2010).
21. Van Den Doel, K., Ascher, U. M. & Pai, D. K. Source localization in electromyography using the inverse potential problem. *Inverse Probl.* **27**, 025008 (2011).
22. Liu, Y. *et al.* Motor unit distribution and recruitment in spastic and non-spastic bilateral biceps brachii muscles of chronic stroke survivors. *J. Neural Eng.* **19**, 046047 (2022).
23. Roeleveld, K., Stegeman, D., Vingerhoets, H. & Oosterom, A. V. The motor unit potential distribution over the skin surface and its use in estimating the motor unit location. *Acta Physiol. Scand.* **161**, 465–472 (1997).

24. Roeleveld, K., Blok, J. H., Stegeman, D. F. & Van Oosterom, A. Volume conduction models for surface EMG; confrontation with measurements. *J. Electromyogr. Kinesiol.* **7**, 221–232 (1997).
25. He, J. & Luo, Z. A simulation study on the relation between the motor unit depth and action potential from multi-channel surface electromyography recordings. *J. Clin. Neurosci.* **54**, 146–151 (2018).
26. Lundsberg, J. H. *Motor Unit Localization Using High-Density Surface.* EMG Master's Thesis, Lund University (2019).
27. Xia, M., Ma, S., Chen, C., Sheng, X. & Zhu, X. Electrodes adaptive model in estimating the depth of motor unit: A motor unit action potential based approach. In *2021 43rd Annual International Conference of the IEEE Engineering in Medicine & Biology Society (EMBC)* 673–676 (IEEE).
28. Roeleveld, K., Stegeman, D. F., Falck, B. & Stålberg, E. V. Motor unit size estimation: Confrontation of surface EMG with macro EMG. *Electroencephalogr. Clin. Neurophysiol. Electromyogr. Motor Control* **105**, 181–188 (1997).
29. Malešević, N. *et al.* Instrumented platform for assessment of isometric hand muscles contractions. *Meas. Sci. Technol.* **30**, 065701 (2019).
30. Hyvärinen, A. & Oja, E. A fast fixed-point algorithm for independent component analysis. *Neural Comput.* **9**, 1483–1492 (1997).
31. Farina, D., Mesin, L., Martina, S. & Merletti, R. A surface EMG generation model with multilayer cylindrical description of the volume conductor. *IEEE Trans. Biomed. Eng.* **51**, 415–426 (2004).
32. Mesin, L. Simulation of surface EMG signals for a multilayer volume conductor with a superficial bone or blood vessel. *IEEE Trans. Biomed. Eng.* **55**, 1647–1657 (2008).
33. Rodriguez-Falces, J., Negro, F., Gonzalez-Izal, M. & Farina, D. Spatial distribution of surface action potentials generated by individual motor units in the human biceps brachii muscle. *J. Electromyogr. Kinesiol.* **23**, 766–777 (2013).
34. Roeleveld, K., Stegeman, D., Vingerhoets, H. & Oosterom, A. V. Motor unit potential contribution to surface electromyography. *Acta Physiol. Scand.* **160**, 175–183 (1997).
35. Vieira, T. M., Loram, I. D., Muceli, S., Merletti, R. & Farina, D. Postural activation of the human medial gastrocnemius muscle: Are the muscle units spatially localised? *J. Physiol.* **589**, 431–443 (2011).
36. Xia, M. *et al.* Extracting individual muscle drive and activity from high-density surface electromyography signals based on the center of gravity of motor unit. *IEEE Trans. Biomed. Eng.* **70**, 2852 (2023).

Author contributions

J.L. developed and implemented the method and drafted the paper. All authors contributed significantly to the analysis and interpretation of the data and revised the paper.

Funding

Open access funding provided by Lund University. This work was supported by the Promobilia Foundation, Stiftelsen för bistånd åt rörelsehindrade i Skåne, and the Swedish Research Council (DNR 2019-05601).

Competing interests

The authors declare no competing interests.

Additional information

Correspondence and requests for materials should be addressed to J.L. or C.A.

Reprints and permissions information is available at www.nature.com/reprints.

Publisher's note Springer Nature remains neutral with regard to jurisdictional claims in published maps and institutional affiliations.

Paper III

Muscle activity mapping by single peak localization from HDsEMG

Lundsberg, J., Björkman, A., Malesevic, N., & Antfolk, C.

Published in: Journal of Electromyography and Kinesiology, 81, 102976. (2025)

Journal of Electromyography and Kinesiology 81 (2025) 102976

Contents lists available at ScienceDirect

Journal of Electromyography and Kinesiology

journal homepage: www.elsevier.com/locate/jelekin

Muscle activity mapping by single peak localization from HDsEMG

Jonathan Lundsberg [a,*], Anders Björkman [b], Nebojsa Malesevic [a], Christian Antfolk [a]

[a] Department of Biomedical Engineering, Faculty of Engineering, Lund University, Lund, Sweden
[b] Department of Hand Surgery, Institute of Clinical Sciences, Sahlgrenska Academy, University of Gothenburg and Sahlgrenska University Hospital, Gothenburg, Sweden

ARTICLE INFO

Keywords:
High-density sEMG
Localization
Muscle modelling
EMG classification

ABSTRACT

Human-machine interfaces using electromyography (EMG) offer promising applications in control of prosthetic limbs, rehabilitation assessment, and assistive technologies. These applications rely on advanced algorithms that decode the activation patterns of muscles contractions. This paper presents a new approach to assess and decode muscle activity by localizing the origin of *individual* temporal peaks in high-density surface EMG recordings from the dorsal forearm during low force finger extensions. Localization was performed using a surface Gaussian fit applied in the spatial domain to the varying amplitudes across the channels of the electrode grids. Localized EMG peaks were used to estimate different muscle volumes for each finger, showing high consistency across 10 subjects. The results suggest that muscle regions generating each action are highly distinct and indicate potential structural differences of muscle fibres between digits. The estimated volumes were further used to classify *individual* EMG peaks into each corresponding action. The percentage of correctly classified peaks for each action across 10 participants were 79 ± 18, 84 ± 9, 76 ± 13, and 79 ± 9 percent for index, middle, ring, and little finger extension, respectively. The presented volume analysis provides a new approach to assessing the spatial activation patterns in compact muscle anatomies; and the single peak classification approach opens up possibilities for near-instantaneous identification of muscle activations.

1. Introduction

The human hand can perform a wide range of different movements and grips thanks to numerous extrinsic and intrinsic muscles acting on the fingers. Extrinsic muscles in the forearm have long tendons that pass multiple joints before inserting in the fingers while intrinsic muscles within the hand fine-tune finger movements. This complex muscle arrangement is controlled by numerous nerves using electrical impulses which are passed on to muscle fibres. Electrical impulses from contracting muscle fibres can be recorded and analysed using electromyography (EMG). Decoding EMG signals is essential for different human–machine interfaces (HMI), benefitting prosthetics (Farina, Jiang et al., 2014a; Marinelli et al., 2023; Parajuli et al., 2019), rehabilitation (Campanini et al., 2020; Fang et al., 2020), and assistive devices (Eddy et al., 2023; Labs et al., 2024). For real-time control of prosthetics and computer interfaces, quick and accurate muscle identification is crucial for intuitive user control (Farina, Jiang et al., 2014a). EMG controlled prosthetic devices have been in development for decades, but they still suffer from high rejection rates (Marinelli et al., 2023; Salminger et al., 2022). In post-stroke rehabilitation, understanding differences between healthy and pathological muscle activation patterns is key for assessment of motor function and guiding rehabilitation (Boukhennoufa et al., 2022; Langhorne et al., 2011). EMG-based HMIs also have broader applications, including spellers (Vasiljevas et al., 2014), game controllers (Zhang et al., 2009), and sign language recognition (Paudyal et al., 2016).

For HMI applications, surface EMG is an attractive choice in particular, since the recording is performed non-invasively on the skin surface. On the other hand, intramuscular EMG is an established technique used to assess neurological impairment (Merletti & Farina, 2009). Such invasive recordings, however, bring a risk of infection as well as discomfort for patients. In both cases, the recorded signal is made up of many motor unit action potentials (MUAPs). The motor unit, the smallest functional muscle component, includes a single motor neuron and all its innervated muscle fibres. Analysing motor unit firing patterns and the location of contracting muscle fibres has attracted a lot of attention (Del Vecchio et al., 2020; Del Vecchio et al., 2017; Farina, Merletti et al., 2014b). Surface EMG, however, has interpretative challenges due to overlapping MUAP waveforms. The increased distance to the muscle from the skin surface, compared to intramuscular EMG,

* Corresponding author.
E-mail address: jonathan.lundsberg@bme.lth.se (J. Lundsberg).

https://doi.org/10.1016/j.jelekin.2025.102976
Received 6 August 2024; Received in revised form 24 November 2024; Accepted 7 January 2025
Available online 9 January 2025

results in a less selective recording, with a bias towards detecting superficial motor units. Furthermore, electrode placement is crucial for high signal-to-noise ratios.

High-density surface EMG (HDsEMG) enables comprehensive muscle activity recordings with large grids of electrodes. Electrode grids cover a larger area than individual electrodes, thus, making optimal electrode placement easier. The numerous channels make blind source separation techniques effective for extracting motor unit signals, which have been extensively researched over the years (Chen et al., 2017; Chen & Zhou, 2015; Dai & Hu, 2019b; Holobar and Zazula, 2007a; Holobar and Zazula, 2007b; Lundsberg et al., 2022; Negro et al., 2016; Ning et al., 2014). Neural networks also show promise in EMG processing, particularly in feature extraction and gesture classification, but require extensive training data and often lack interpretability (Xiong et al., 2021). Typically, the blind source separation task for HDsEMG is approached using independent component analysis (Comon, 1994; Hyvärinen et al., 2001), with time-delayed extensions of data channels (Chen et al., 2017; Chen & Zhou, 2015; Holobar and Zazula, 2007a; Holobar and Zazula, 2007b; Lundsberg et al., 2022; Negro et al., 2016; Ning et al., 2014). These decomposition algorithms attempt to identify all firing instances of individual motor units. That is, MUAP timings are identified without morphological information of the waveform. The MUAP waveform is then obtained through spike-triggered averaging across all firings of the motor unit, rather than analysing the individual firing instances. Much research and analysis of muscle activation patterns rely on the improvement of decomposition algorithms. However, the performance of these algorithms in terms of true positive rate, i.e. the fraction of active motor units that are correctly identified, is limited or unclear (Farina et al., 2010), especially during dynamic contractions which are relevant in many applications. The number of motor units which can be identified with decomposition of HDsEMG varies greatly between muscles and data quality (Farina et al., 2010). Furthermore, decomposition can be slow, depending on, e.g., the number of channels and the extension factor, both of which increase the size of the matrix calculations (Chen & Zhou, 2015; Holobar and Zazula, 2007a; Holobar and Zazula, 2007b; Negro et al., 2016), and a great deal of manual effort is sometimes required to optimize decomposition results. Although, once identified, a demixing matrix can be used to decompose further HDsEMG data in real-time (Barsakcioglu & Farina, 2018; Glaser et al., 2013). Decomposition on its own enables analysis of the temporal activation patterns of motor units, whereas analysis of the spatial activation patterns requires additional algorithms.

The location of each motor unit from decomposition of HDsEMG can be derived from the MUAP waveform detected at multiple locations. The MUAP waveform varies in shape and amplitude across the channels of the high-density grid. This distribution of MUAP waveforms in relation to the motor unit position has been studied for a long time (Roeleveld et al., 1997a; Roeleveld et al., 1997b). For motor units located deeper below the skin, the amplitude distribution of the waveforms is more uniform than that of superficial motor units, since the relative distance to each electrode is more equal. The width of the MUAP amplitude distribution can therefore be used to estimate the motor unit depth (Roeleveld et al., 1997c; Roeleveld et al., 1997a; Roeleveld et al., 1997b). A major limitation in this approach is the statistical uncertainty that comes from analysing a relatively low number of motor units. Furthermore, real-time localization is difficult, since the MUAP waveforms are obtained by averaging over many firings. A different approach, complementary to motor unit analysis, could therefore be useful. Surface heat maps of macro-EMG features, such as root mean square (RMS) amplitude distributions, have been used to analyse muscle activation patterns on a more aggregate level (Dai & Hu, 2019a; Gallina & Botter, 2013; Hu et al., 2015). A more granular analysis, however, of localizing individual temporal peaks in the EMG signal is less explored. The large number of individual potential peaks in HDsEMG recordings could offer statistical robustness exceeding that of motor unit analysis. Additionally, robust classification of individual EMG peaks into different muscles could result in faster identification of muscle contractions and user intent, critical to intuitive and natural control in human–machine interfaces.

The aim of this study was to test a new method for assessing muscle function with high statistical robustness, to compliment motor unit analysis typically done on relatively few motor units. We applied a motor unit localization algorithm (Lundsberg et al., 2024) to individual motor unit firings, replacing averaged MUAP waveforms with single EMG peaks. For clarity, EMG peaks refer to local temporal peak amplitudes generated by MUAPs, which can include multiple overlapping motor unit firings. Despite high variance due to overlapping firings and noise, the large number of recorded action potentials offers sufficient statistical power to identify distinct muscle volumes. We identify volumes for the muscles responsible for finger extension and evaluate their separation visually and by volume cross-coverage, with the aim to enhance understanding of neuromuscular activation patterns in compact anatomies, such as the forearm. The identified volumes are used to classify individual EMG peaks, assessing performance by true and false positive rates, with the aim to enable near-instantaneous identification of muscle contractions. This initial study focuses on low force contractions, which are relevant to gesture identification and early rehabilitation assessments. For gesture identification, we see sign language recognition (Paudyal et al., 2016) and spellers (Vasiljevas et al., 2014) as key applications; these cases involve specific low forces, in contrast to applications involving force regression over a large range of forces. Similarly, low force contractions can be used as computer inputs (Labs et al., 2024; Zhang et al., 2009), simulating e.g., specific discrete keyboard inputs. For early rehabilitation assessments, where patients have lost most of their motor function and thus produce weaker EMG signals, there is potential to assess the amount of compensation from other muscles by mapping the spatial distribution all individual EMG peaks.

2. Method

2.1. Participants

Ten healthy volunteers, eight men and two women, aged 22 to 44 years participated in the study. Exclusion criteria were history of neurological disorders and history of severe trauma to the right arm or hand. All participants provided informed consent. The study was approved by the Regional Ethical Review Board in Lund, Sweden (DNR 2017–297).

2.2. Data acquisition

Two high-density electrode grids (64 gold-coated electrodes each, 5-by-13 in a monopolar configuration, 1 mm electrode diameter, 8 mm interelectrode distance, Model ELSCH064NM2, OT Bioelettronica, Torino, Italy) were placed adjacently on the dorsal side of the proximal right forearm, with missing electrodes in the proximal-radial and distal-ulnar corners (Fig. 1). HDsEMG was sampled with a 16-bit analog-to-digital converter (input referred noise $< 4\ \mu V_{RMS}$, common-mode rejection ratio > 95 dB at 50 Hz, Quattrocento, OT Bioelettronica, Torino, Italy) at a sampling rate of 2048 Hz, amplified 150 times and analog bandpass filtered (0.7–900 Hz). The signals were displayed in OT Biolab + v1.5.9 (OT Bioelettronica, Torino, Italy). The EMG data was further digitally filtered off-line with two-pass zero-phase filtering using a third order Butterworth notch filter (49–51 Hz) and a third order Butterworth bandpass filter (5–500 Hz), in MATLAB R2022b (MathWorks, Natick, Massachusetts, USA).

With the forearm prone, participants performed low-force isometric contractions, one finger at a time, upwards against a force gauge (Model M5-20, Mark-10, Copiague, NY, USA) which provided visual feedback by displaying the force in real-time. Index, middle, ring, and little finger extensions were individually maintained at 1 N for 60 s each. Using force

Fig. 1. The placement of the high-density electrode grids on the dorsal side of the proximal half of the right forearm, and the index finger position pushing upwards against the force gauge.

levels at a percentage of maximum voluntary contractions (MVC) could also have been used to adjust for differences in muscle strength between actions and individuals. However, differences in MVCs between individual finger extensors or participants may be affected by synergistic muscle contractions such as the extensor carpi muscles, resulting in a large range of force levels. The motivation for using the same force level for all actions was to remove the force level as a potential confounding factor and to highlight the differences in active regions between finger extensors when producing the same force. Participants were first familiarized with the setup and the correct force level. Poor quality channels were manually excluded by visually inspecting the recordings and removing those with flat signals or exceptionally high root-mean-square (RMS) amplitude at rest which exceeded that of EMG signals during muscle contractions. The same channels were then excluded for each recording from the participant.

2.3. Action potential localization

The localization algorithm used in this paper was previously developed for localization of motor units obtained through decomposition (Lundsberg et al., 2024). In the previous implementation, estimates of the muscle fibre direction and 3D-coordinates of motor unit centre positions were obtained from the amplitude distribution of the average MUAP waveform. In this study, the need for decomposition is circumvented by replacing the average MUAP waveform, typically obtained through spike-triggered averaging, with the extracted waveforms of individual EMG peaks. Estimates for the muscle fibre direction and 3D-coordinates are then obtained for the individual EMG peaks, in the same manner as in (Lundsberg et al., 2024).

Individual EMG peaks were identified on the channel with the highest RMS amplitude using a custom peak detection algorithm written in MATLAB R2022b (MathWorks, Natick, Massachusetts, USA). The channel selection for peak detection is further addressed in the discussion. For each sample of the selected channel, the time instance was identified as a peak if that sample had the highest amplitude in a 31-sample window (15 samples before and after), approximately 15.1 ms, and was above a $50\mu V$ threshold. Thus, peaks within 15 samples of a larger peak were automatically ignored. The window size was empirically chosen to avoid detecting the same MUAP more than once, due to the multiple phases of the MUAP waveform. The threshold was chosen to exceed that of base-line noise. The peak detection parameters were then applied uniformly to all recordings. It is important to note that there is ambiguity at higher forces regarding whether peaks represent a single or multiple motor unit action potentials; the implications of which are addressed in the discussion.

For each identified peak, a 31-sample window, approximately 15.1 ms, was extracted synchronously from all channels (Fig. 2) and used for single peak localization. The window size was chosen to be the same as during peak detection for simplicity and was not studied extensively. For each channel, the peak-to-peak amplitude within the window was identified, and each channel was mapped to its spatial location on the HDsEMG grid on the skin surface. A generalized two-dimensional Gaussian surface fit was applied in the spatial domain to the identified amplitudes across all channels, explained in detail here (Lundsberg et al., 2024). The Gaussian fit's width informed the estimated depth in a volume conductor model, explained in detail here (Lundsberg et al., 2024), and the centre of the fit determined the estimation of the position along the skin surface. The rotation of the fit determined the estimation of the muscle fibre direction, with the assumption that the spread of the two-dimensional Gaussian fit is largest along the fibre direction (Lundsberg et al., 2024). Despite high variance for the localization of individual EMG peaks, due to noise and MUAP overlap, the vast number of localized EMG peaks allows for highly robust modelling of active regions. Different volume conductor models were not investigated which may result in differences for localization in absolute values. However, this study focused on localization in relative terms, in order to assess differences between different actions.

2.4. Muscle modelling

2.4.1. Modelling and evaluation split

The identified peaks from each 60 s recording were split into a modelling batch and a validation batch. Approximately half of the peaks in each recording were randomly selected and used to create a volume representing the corresponding muscle. The remaining peaks were used for evaluation with true and false positive rates, described in section 2.5. To test the stability of volume estimation, this modelling and validation split was repeated 10 times for each 60 s recording.

2.4.2. Ellipsoid volume estimation

Muscle volumes were modelled as ellipsoids from the distribution of the localized EMG peaks (Fig. 2). The ellipsoid function was chosen for its simple expression, where the radii in each dimension determines the shape.

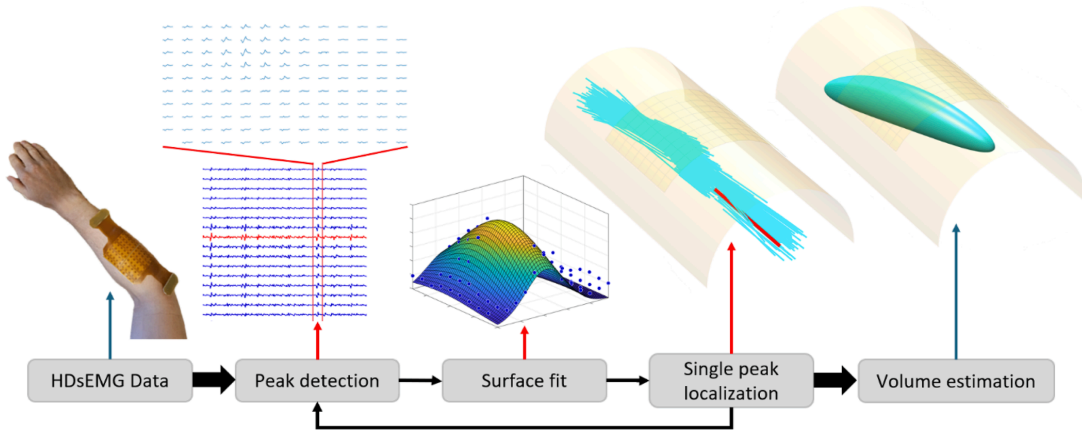

Fig. 2. Overview of the muscle region modelling approach. HDsEMG data is recorded by two adjacent 5x13 grids with 128 monopolar channels. Peak detection is performed on the highest RMS channel, and a window of samples across all channels is extracted for each peak. A surface Gaussian fit is applied in the spatial domain to the peak-to-peak amplitudes of all channels. Individual EMG peaks are localized using the surface fit parameters. Ellipsoid volumes are estimated from the mean and standard deviations of the localized EMG peak positions.

$$\frac{x^2}{r_x^2}+\frac{y^2}{r_y^2}+\frac{z^2}{r_z^2}=1 \tag{1}$$

The radii, r, in each dimension were set by the three-dimensional spread of localized EMG peaks in the depth direction, z, along the fibre direction, y, and perpendicular to the fibre and depth direction, x. Note that these ellipsoid volumes are a functional representation of the origin of each muscle's EMG activity, in contrast to anatomical representations of muscle fibres. To exclude localized peaks from distant co-activated muscles and noise points in the modelling step, density-based spatial clustering using the DBSCAN algorithm (Ester et al., 1996) was applied to localized peaks in the medial-to-lateral axis, with the distance parameter set to 2 cm and minimum neighbours set to half the total number of peaks. This clustering step was not deemed necessary along the depth axis since, anatomically, the deep muscles of the dorsal compartment of the forearm are abductor pollicis longus and extensor pollicis longus, which were not expected to co-contract with the extensor digitorum communis and extensor digiti minimi muscles. The clustering parameters were chosen empirically to create a lenient selection and only exclude distant peaks but were not studied extensively. From this selection of localized EMG peaks, the mean position, μ, and two standard deviations in each direction, 2σ, determined the ellipsoid position and shape.

$$\frac{(x-\mu_x)^2}{(2\sigma_x)^2}+\frac{\left(y-\mu_y\right)^2}{(2\sigma_y)^2}+\frac{(z-\mu_z)^2}{(2\sigma_z)^2}=1 \tag{2}$$

The rotation of the fibre direction, θ, was accounted for by first applying the inverse rotation matrix around the depth axis (Eq. (3)), given by the mean fibre rotation angle (Eq. (4).

$$\begin{bmatrix}x\\y\\z\end{bmatrix}=R_z^{-1}\begin{bmatrix}\hat{x}\\\hat{y}\\\hat{z}\end{bmatrix} \tag{3}$$

$$R_z=\begin{bmatrix}\cos\theta & -\sin\theta & 0\\ \sin\theta & \cos\theta & 0\\ 0 & 0 & 1\end{bmatrix} \tag{4}$$

This transformation was identified for each unique volume. Fibre rotations around other axes were not considered since this information was not generated by the localization algorithm.

2.5. Coverage & classification

2.5.1. Volume coverage

The ellipsoid function (Eq. (2) can be seen as an isosurface function with an isovalue of 1. For a given position, $f(x,y,z)$, the function value is less than one inside the ellipsoid and greater than one outside the ellipsoid. The unique offset position, μ, ellipsoid shape, σ, and rotation matrix, R_z, for each volume, results in different isosurface function values for each volume. The volume coverage of localized peaks for each ellipsoid was evaluated for the corresponding action (true positive rate), and the volume cross coverage for other actions (false positive rates). For each ellipsoid volume, the isosurface function (Eq. (1) was evaluated for the position of every localized peak. True and false positive rates were calculated by counting the number of localized peaks within each volume, for each action. Thus, the false positive rates provide some indication to the amount of overlap between volumes. Whereas the true positive rates are limited by the selection criteria localized peaks during the modelling step, e.g., defining the ellipsoid shapes with two standard deviations in each direction.

2.5.2. Single peak classification

The ellipsoid volumes were used to classify localized peaks by comparing the isovalues between volumes. For a given position, $f(x,y,z)$, the function value (using Eq. (1) increases with increased distance from the volume centre, modified by the shape of the volume. Thus, each localized EMG peak was assigned to the volume resulting in the lowest function value. A more typical distance measure may have been the Euclidian distance to each volume centre. However, Euclidian distance would heavily favour smaller volumes. Thus, better classification performance can be achieved using the ellipsoid isosurface function values. This comparison is included in the Supplementary S3.

2.5.3. Majority vote classification

In contrast to single peak classification, multiple peaks can be used to improve classification of muscle activity, resulting in a time-accuracy trade-off. To determine this trade-off, a simple majority vote classification was implemented, which greatly increased performance compared to single peak classification. For each peak, the subsequent 1, 3, 5, …, 15

peaks in the validation batch were included in the voting procedure.

3. Results

3.1. Volume coverage

Localization of all EMG peaks on the dorsal side of the forearm, and corresponding ellipsoid volumes resulting from extensions of different fingers are shown in Fig. 3 for one of the participants (all participants are shown in Supplementary S2). In this 3D plot, the relative regions of each activation can be evaluated and understood visually. The extensor digitorum communis (EDC) is the common extensor muscle for all the four digits, yet the separation of the ellipsoid volumes is very clear and is consistent across participants. In all participants, the region estimated from middle finger extension (green), was located proximally compared to the other regions. The regions estimated from index (red), ring (cyan), and little (purple) finger extension, showed a distinct anatomical arrangement from radial to ulnar, which corresponds well with how the fingers are located. The only exceptions were for two participants, where activity was identified on the ulnar side during index extension (Supplementary S2), which could be explained by co-activation of the extensor carpi ulnaris muscle. The consistent separation between each finger seen in both plots (Fig. 3) suggests that the organization within the EDC muscle is highly distinct. Furthermore, a higher degree of estimated rotation is consistently observed for index extension, which may indicate structural differences between the subregions of the muscle.

For a quantitative analysis, the volume coverage of peaks in Table 1 shows the cross-subject mean and standard deviation for the percentage of localized peaks covered by each volume for each action (individual tables for each participant are shown in Supplementary S1). From each 60 s recording, an average of approximately 1300 individual EMG peaks were classified (half of the total), with an equivalent number of peaks used to create each volume. The amount of overlap between volumes can be evaluated by the false positive rates (off-diagonal elements), in contrast to the true positive rates (diagonal elements). The greatest overlap was seen between ring and little finger extension. However, the greatest variability came from the index volume.

3.2. Classification

The classification of peaks in Table 1 shows the cross-subject mean and standard deviation for the true positive rates (diagonal elements) and false positive rates (off-diagonal elements), in the single peak classification task (individual tables for each participant are shown in Supplementary S1). The mean true positive rates for index, middle, ring, and little finger extension were 79 ± 18, 84 ± 9, 76 ± 13, and 79 ± 9 percent, respectively.

Fig. 4 shows the muscle classification task by majority voting, for each participant and each action, as well as the cross-subject mean. Note that the mean for single peak voting in Fig. 4 is equivalent to the true positive rate reported in Table 1. For index classification, the mean is drastically reduced by two participants (participant 2 and 4) with poor performance, caused by poor underlying data, which can be seen in the individual results in Supplementary S1. For participants with high single peak true positive rates, the performance increase quickly plateaued for very few peaks, which signifies the importance of high-quality data. The average frequency of localized EMG peaks was 44.2 peaks per second. Thus, 3-peak voting was equivalent to 68 ms and 5-peak voting to 113 ms, on average.

4. Discussion

Here we present a new method to map muscle volumes and classify single EMG peaks from HDsEMG recordings. The new method manages to consistently generate unique muscle volumes from HDsEMG during isolated finger extensions. The visual analysis suggests that extension of individual fingers is mainly generated by highly distinct subregions of the EDC. It is particularly easy to separate middle finger extension from other finger extensions, since the muscle activity is generated at the proximal end of the EDC. Furthermore, we show that classification of individual EMG peaks is possible with high accuracy, which can enable near-instantaneous classification of muscle activity.

The results of the visual analysis provide a more detailed estimate of the organizational structure of muscles responsible for finger extensions at low forces, compared to previous RMS based studies (Gallina & Botter, 2013). Additionally, with this method we see that localized EMG peaks from index finger extension had a higher degree of rotation of the fibre direction, compared to other actions. This could be an indication of differences in the underlying anatomical structure, for example due to fibre pinnation. Alternatively, it could also be the result of synergistic activity between the EDC and extensor indicis proprius or muscles responsible for wrist extension, such as extensor carpi radialis longus and brevis. This additional rotation may, however, be sensitive to the location of the high-density grids. Future studies should therefore assess the entire length of the forearm.

The presented method provides a consistent, simple, and intuitive way to investigate neuromuscular activity, which does not require specialized knowledge to use and can be easily automated. In contrast, the recurring limitation of motor unit analysis through decomposition is the uncertainty in the fraction of motor units that are identified, and the manual work and expertise required to ensure accurate decomposition

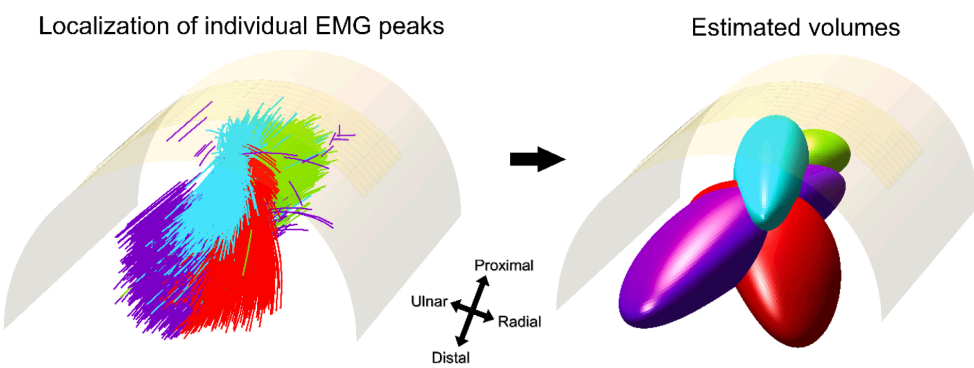

Fig. 3. 3D-plot of localized EMG peaks (left) and the corresponding generated ellipsoid volumes (right), for index (red), middle (green), ring (cyan), and little (purple) finger extension.

Table 1
Cross-subject mean and standard deviations of true and false positive rates (diagonal and off-diagonal elements respectively), with regards to volume coverage and classification of individual EMG peaks. Peak count refers to the number of EMG peaks in the validation batch, approximately half of all peaks. Vol 1, 2, 3, and 4 refer to the volumes generated from index, middle, ring, and little finger extension, respectively.

		Volume coverage of peaks (%)				Classification of peaks (%)			
Finger	Peak count	Vol 1	Vol 2	Vol 3	Vol 4	Vol 1	Vol 2	Vol 3	Vol 4
Index	1038 ± 325	70 ± 14	5 ± 10	13 ± 14	7 ± 9	79 ± 18	2 ± 4	9 ± 9	9 ± 13
Middle	1462 ± 165	6 ± 10	77 ± 5	15 ± 15	4 ± 6	5 ± 6	84 ± 9	8 ± 6	3 ± 4
Ring	1540 ± 122	19 ± 24	16 ± 18	73 ± 6	20 ± 17	9 ± 12	8 ± 5	76 ± 13	8 ± 6
Little	1266 ± 251	19 ± 26	2 ± 5	24 ± 26	76 ± 4	10 ± 10	1 ± 1	10 ± 10	79 ± 9

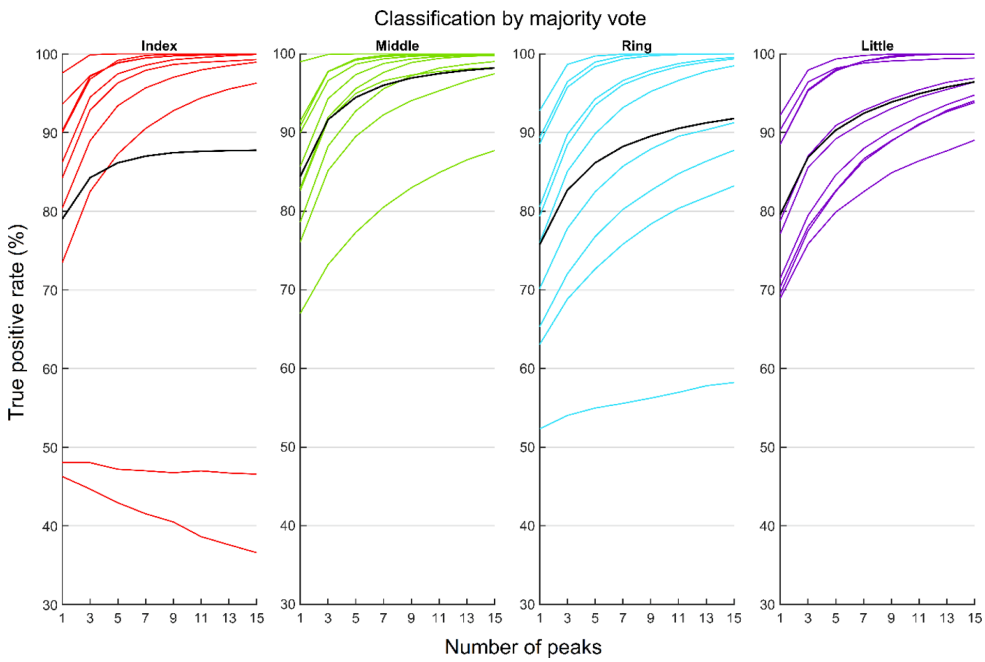

Fig. 4. Muscle classification by majority vote for each participant for index (red lines), middle (green lines), ring (cyan lines), and little (purple lines) finger extension and the cross-subject means (black lines) for each action. Note that the mean majority vote with a single peak is equivalent to the classification in Table 1. The lowest true positive rate for all actions came from the same participant. For index extension, one participant did not achieve an isolated contraction, resulting in a low true positive rate as well. With an average of 44.2 peaks per second, 3-peak voting was equivalent to 68 ms and 5-peak voting to 113 ms.

(Farina et al., 2010). Furthermore, the modelling of muscle volumes requires very little data compared to neural network approaches (Xiong et al., 2021). The new method, however, does not provide the same neurological analysis of motor unit firing rates gained through decomposition. Additionally, since the ellipsoid volumes are functional representations of EMG activity, the accuracy is difficult to assess in

anatomical terms. Instead, the utility of the method, as presented in this paper, lies in identifying and quantifying differences between actions. A future application of the presented method could be to assess the degree of isolated muscle control, or the effort generated by individual muscles. Patients with lost motor function and reduced EMG activity, e.g. after stroke, and their therapists', could potentially gain valuable feedback on the underlying individual muscle activity and points of weakness, which in turn could inform future rehabilitation exercises.

The classification results in this study showcases the importance of good underlying data. The mean performance is drastically reduced by two participants as seen in Fig. 4. For participant 2, performing index finger extension resulted in two distinct regions of localized EMG peaks (Supplementary Fig. S2). The smaller group of localized peaks were excluded from the volume estimation by the clustering step with the DBSCAN algorithm. This reduced the risk of overestimating the volume, but also resulted in a true positive rate of 48 % (Supplementary Table S2), compared to the 79 % cross-subject average (Table 1) and the 98 % highest (Supplementary Table S6), for this action. This case indicates that isolated contractions may sometimes be difficult to achieve, which is an important aspect to consider for this modelling method. For participant 4, the estimated volumes overlapped to a much a higher degree than other participants, as revealed by the 3D-plot (Supplementary Fig. S4) and cross coverage values (Supplementary Table S4). This resulted in very poor classification performance across the board at 46, 67, 52, and 69 % for index, middle, ring, and little finger extension, respectively. For other participants, however, where single peak classification resulted in above 90 % true positive rates, the potential for a near instantaneous HMI is promising. Majority voting with 3 or 5 peaks could be a very potent muscle classification approach. On average, 5 peaks were equivalent to a 113 ms time window. Thus, a classification protocol is theoretically possible with a very low latency which maintains high robustness.

The main limitation of the study concerning the classification task is that each action was isometric and recorded separately. The method should be tested for classification of dynamic contractions and the transition between different actions, which would address robustness to the shifting position of muscle bodies in relation to the estimated volumes. Additionally, classification should be tested on data with multiple muscles activated at once, to address whether simultaneous activity from multiple separate muscles interferes with classification performance. Furthermore, this study focused on low force contractions, which could be a limitation for some applications. While prosthetic control typically relies on continuous control and different contraction forces, generic HMIs, however, may rely more on discrete events as inputs (Eddy et al., 2023). For discrete inputs, fast and subtle low effort contractions would be more desirable, to minimize fatigue. For example, in virtual and augmented reality applications, we hypothesize that this will enable the creation of an 'intimate' HMI, as user will not need to exert high force, and latency will be low.

EMG peaks were selected by peak detection on the highest RMS channel, which may be a limitation for real-time applications. However, in our experience we found minimal performance differences between selecting the highest RMS channel and any central channel on the grid for peak detection. This consistency between channels can be explained by the window size of 15 ms that was extracted for each EMG peak. In most cases this window would include the same peak-to-peak amplitude values regardless of which channel was used for peak detection. In this study, there could be a potential bias in localization due to a selection of firings from a specific type of motor unit. The low force contractions used may exclude many large motor units and the amplitude threshold for peak-detection may exclude very small motor units. Whether the spatial distribution of the remaining motor unit firings is representative of all firings is unknown. Furthermore, whether identified EMG peaks are the result of individual or multiple motor unit firings should be discussed, especially for higher force levels. When smaller motor unit firings overlap with larger firings, they are potentially lost when extracting the peak-to-peak amplitude. A different measure, such as the energy at each channel, could be more suitable. With an energy measure, overlapping firings would all contribute to a compounded location estimate. Such a compounded estimate, however, might have additional limitations if multiple muscles are active at once.

The approach presented in this paper provides a new mode of analysis which may complement motor unit analysis done through decomposition approaches. A combination of the two approaches should be explored by, for example, localizing motor units from decomposition alongside volumes generated by the presented approach. In this manner, motor unit analysis could be done with the information of muscle structures and functional organization generated by the new approach. Additionally, a comparison between localized volumes and localized motor units should be done to assess, and account for, potential discrepancies.

5. Declarations

5.1. Ethics approval and consent to participate

The study was approved by the Regional Ethical Review Board in Lund, Sweden (DNR 2017–297) and was conducted in accordance with the tenets of the Declaration of Helsinki. All participants were informed about the contents of the experiments, both verbally and in writing, and gave their informed and written consent.

Author contributions

JL conceived of and implemented the method and drafted the paper. All authors contributed significantly to the analysis and interpretation of the data. All authors contributed significantly to revising the paper.

CRediT authorship contribution statement

Jonathan Lundsberg: Writing – review & editing, Writing – original draft, Visualization, Validation, Methodology, Investigation, Funding acquisition, Formal analysis, Data curation, Conceptualization. **Anders Björkman:** Writing – review & editing, Supervision, Formal analysis. **Nebojsa Malesevic:** Writing – review & editing, Supervision, Funding acquisition, Formal analysis. **Christian Antfolk:** Writing – review & editing, Supervision, Funding acquisition, Formal analysis.

Funding

This work was supported by the Promobilia Foundation, Stiftelsen för bistånd åt rörelsehindrade i Skåne, and the Swedish Research Council (DNR 2019–05601).

Declaration of competing interest

The authors declare that they have no known competing financial interests or personal relationships that could have appeared to influence the work reported in this paper.

Appendix A. Supplementary data

Supplementary data to this article can be found online at https://doi.org/10.1016/j.jelekin.2025.102976.

References

Barsakcioglu, D.Y., Farina, D., 2018. A real-time surface EMG decomposition system for non-invasive human-machine interfaces. 2018 IEEE Biomedical Circuits and Systems Conference (BioCAS).

Boukhennoufa, I., Zhai, X., Utti, V., Jackson, J., McDonald-Maier, K.D., 2022. Wearable sensors and machine learning in post-stroke rehabilitation assessment: A systematic review. Biomed. Signal Process. Control 71, 103197.

Campanini, I., Disselhorst-Klug, C., Rymer, W.Z., Merletti, R., 2020. Surface EMG in clinical assessment and neurorehabilitation: barriers limiting its use. Front. Neurol. 11, 556522.
Chen, M., Zhang, X., Chen, X., Zhou, P., 2017. Automatic implementation of progressive FastICA peel-off for high density surface EMG decomposition. IEEE Trans. Neural Syst. Rehabil. Eng. 26 (1), 144–152.
Chen, M., Zhou, P., 2015. A novel framework based on FastICA for high density surface EMG decomposition. IEEE Trans. Neural Syst. Rehabil. Eng. 24 (1), 117–127.
Comon, P., 1994. Independent component analysis, a new concept? Signal Process. 36 (3), 287–314.
Dai, C., Hu, X., 2019a. Extracting and classifying spatial muscle activation patterns in forearm flexor muscles using high-density electromyogram recordings. Int. J. Neural Syst. 29 (01), 1850025.
Dai, C., Hu, X., 2019b. Independent component analysis based algorithms for high-density electromyogram decomposition: Systematic evaluation through simulation. Comput. Biol. Med. 109, 171–181.
Del Vecchio, A., Negro, F., Felici, F., Farina, D., 2017. Associations between motor unit action potential parameters and surface EMG features. J. Appl. Physiol. 123 (4), 835–843.
Del Vecchio, A., Holobar, A., Falla, D., Felici, F., Enoka, R., Farina, D., 2020. Tutorial: Analysis of motor unit discharge characteristics from high-density surface EMG signals. J. Electromyogr. Kinesiol. 53, 102426.
Eddy, E., Scheme, E.J., Bateman, S., 2023. A framework and call to action for the future development of emg-based input in hci. Proceedings of the 2023 CHI Conference on Human Factors in Computing Systems.
Ester, M., Kriegel, H.-P., Sander, J., Xu, X., 1996. A density-based algorithm for discovering clusters in large spatial databases with noise. Proceedings of the Second International Conference on Knowledge Discovery and Data Mining.
Fang, C., He, B., Wang, Y., Cao, J., Gao, S., 2020. EMG-centered multisensory based technologies for pattern recognition in rehabilitation: state of the art and challenges. Biosensors 10 (8), 85.
Farina, D., Holobar, A., Merletti, R., Enoka, R.M., 2010. Decoding the neural drive to muscles from the surface electromyogram. Clin. Neurophysiol. 121 (10), 1616–1623.
Farina, D., Jiang, N., Rehbaum, H., Holobar, A., Graimann, B., Dietl, H., Aszmann, O.C., 2014a. The extraction of neural information from the surface EMG for the control of upper-limb prostheses: emerging avenues and challenges. IEEE Trans. Neural Syst. Rehabil. Eng. 22 (4), 797–809.
Farina, D., Merletti, R., Enoka, R.M., 2014b. The extraction of neural strategies from the surface EMG: an update. J. Appl. Physiol. 117 (11), 1215–1230.
Gallina, A., Botter, A., 2013. Spatial localization of electromyographic amplitude distributions associated to the activation of dorsal forearm muscles. Front. Physiol. 4, 67953.
Glaser, V., Holobar, A., Zazula, D., 2013. Real-time motor unit identification from high-density surface EMG. IEEE Trans. Neural Syst. Rehabil. Eng. 21 (6), 949–958.
Holobar, A., Zazula, D., 2007a. Gradient convolution kernel compensation applied to surface electromyograms. International Conference on Independent Component Analysis and Signal Separation.
Holobar, A., Zazula, D., 2007b. Multichannel blind source separation using convolution kernel compensation. IEEE Trans. Signal Process. 55 (9), 4487–4496.
Hu, X., Suresh, N.L., Xue, C., Rymer, W.Z., 2015. Extracting extensor digitorum communis activation patterns using high-density surface electromyography. Front. Physiol. 6, 152915.
Hyvärinen, A., Karhunen, J., Oja, E., 2001. Independent Component Analysis. Wiley. https://books.google.se/books?id=9TQNEAAAQBAJ.
Labs, C.-l. a. R., Sussillo, D., Kaifosh, P., & Reardon, T. (2024). A generic noninvasive neuromotor interface for human-computer interaction. bioRxiv, 2024.2002.2023.581779.
Langhorne, P., Bernhardt, J., Kwakkel, G., 2011. Stroke rehabilitation. Lancet 377 (9778), 1693–1702.
Lundsberg, J., Björkman, A., Malesevic, N., Antfolk, C., 2022. Compressed spike-triggered averaging in iterative decomposition of surface EMG. Computer Methods and Programs in Biomedicine.
Lundsberg, J., Björkman, A., Malesevic, N., Antfolk, C., 2024. Inferring position of motor units from high-density surface EMG. Sci. Rep. 14 (1), 3858.
Marinelli, A., Boccardo, N., Tessari, F., Di Domenico, D., Caserta, G., Canepa, M., Gini, G., Barresi, G., Laffranchi, M., De Michieli, L., 2023. Active upper limb prostheses: A review on current state and upcoming breakthroughs. Prog. Biomed. Eng. 5 (1), 012001.
Merletti, R., Farina, D., 2009. Analysis of intramuscular electromyogram signals. Philos. Trans. R. Soc. A Math. Phys. Eng. Sci. 367 (1887), 357–368.
Negro, F., Muceli, S., Castronovo, A.M., Holobar, A., Farina, D., 2016. Multi-channel intramuscular and surface EMG decomposition by convolutive blind source separation. J. Neural Eng. 13 (2), 026027.
Ning, Y., Zhu, X., Zhu, S., Zhang, Y., 2014. Surface EMG decomposition based on K-means clustering and convolution kernel compensation. IEEE J. Biomed. Health Inform. 19 (2), 471–477.
Parajuli, N., Sreenivasan, N., Bifulco, P., Cesarelli, M., Savino, S., Niola, V., Esposito, D., Hamilton, T.J., Naik, G.R., Gunawardana, U., 2019. Real-time EMG based pattern recognition control for hand prostheses: A review on existing methods, challenges and future implementation. Sensors 19 (20), 4596.
Paudyal, P., Banerjee, A., Gupta, S.K., 2016. Sceptre: a pervasive, non-invasive, and programmable gesture recognition technology. Proceedings of the 21st International Conference on Intelligent User Interfaces.
Roeleveld, K., Blok, J.H., Stegeman, D.F., Van Oosterom, A., 1997a. Volume conduction models for surface EMG; confrontation with measurements. J. Electromyogr. Kinesiol. 7 (4), 221–232.
Roeleveld, K., Stegeman, D., Vingerhoets, H., Oosterom, A.V., 1997b. Motor unit potential contribution to surface electromyography. Acta Physiol. Scand. 160 (2), 175–183.
Roeleveld, K., Stegeman, D., Vingerhoets, H., Oosterom, A.V., 1997c. The motor unit potential distribution over the skin surface and its use in estimating the motor unit location. Acta Physiol. Scand. 161 (4), 465–472.
Salminger, S., Stino, H., Pichler, L.H., Gstoettner, C., Sturma, A., Mayer, J.A., Szivak, M., Aszmann, O.C., 2022. Current rates of prosthetic usage in upper-limb amputees–have innovations had an impact on device acceptance? Disabil. Rehabil. 44 (14), 3708–3713.
Vasiljevas, M., Turčinas, R., Damaševičius, R., 2014. Development of EMG-based speller. Proceedings of the XV International Conference on Human Computer Interaction.
Xiong, D., Zhang, D., Zhao, X., Zhao, Y., 2021. Deep learning for EMG-based human-machine interaction: A review. IEEE/CAA J. Autom. Sin. 8 (3), 512–533.
Zhang, X., Chen, X., Wang, W.-H., Yang, J.-H., Lantz, V., Wang, K.-Q., 2009. Hand gesture recognition and virtual game control based on 3D accelerometer and EMG sensors. Proceedings of the 14th International Conference on Intelligent User Interfaces.

Paper IV

Generalizable gesture classification of HDsEMG using volume representations of muscles averaged across multiple individuals

Lundsberg, J., Björkman, A., Malesevic, N., & Antfolk, C

Manuscript

Title: Generalizable gesture classification of HDsEMG using volume representations of muscles averaged across multiple individuals

Jonathan Lundsberg[1], Anders Björkman[2,3], Nebojsa Malesevic[1], Christian Antfolk[1]

1) Department of Biomedical Engineering, Faculty of Engineering, Lund University, Lund, Sweden
2) Institute of Clinical Sciences, Sahlgrenska Academy, University of Gothenburg, Sweden
3) Department of Hand Surgery, Sahlgrenska University Hospital, Mölndal, Sweden

Corresponding author: Jonathan Lundsberg (jonathan.lundsberg@bme.lth.se)

Keywords: High-density sEMG, localization, muscle modelling, EMG classification

Abstract:

Human hands can perform far more gestures than the number of muscles controlling them, as most gestures result from coordinated combinations of muscle activations and relaxations. This complexity poses a key challenge for human-machine interfaces performing gesture classification based on electromyography (EMG). Rather than identifying all conceivable gestures, it may be simpler to instead identify the activity of the individual muscles which generate a variety of complicated gestures.

Here we suggest a three-dimensional model with volume representations of individual digit extensor muscles, averaged across multiple individuals, and evaluate its application and performance in hand gesture classification. Time-domain peaks in high-density surface EMG data from different hand gestures were extracted and localized within the model, from which a gesture classification scheme was generated for both single and multi-label cases. The model was created and tested on a publicly available dataset with 19 participants, leveraging a leave-one-out approach to assess inter-subject generalizability, and multi-label data to assess generalizability to gestures not included in the creation of the model. Furthermore, multi-label metrics were calculated, resulting in a median Hamming loss of 21.4 (IQR 18.7-25.3), Precision of 79.1 (IQR 72.6-87.7), Recall of 60.1 (IQR 53.1-62.8) and F1-score of 68.4 (IQR 63.1-72.6) percent. A model generated with this approach could be used for gesture classification by anyone, without individual modelling data, with the potential to generalize to any number of gestures.

1. Introduction

The human hand can perform a large number of actions despite being controlled by a limited number of intrinsic and extrinsic muscles. While the anatomy of forearm and hand muscles is well understood, the permutations of muscle combinations that generate grasps, gestures, and actions are vast, which poses a challenge for the development of advanced human-machine interfaces (HMIs). HMIs based on electromyography (EMG) decode descending neural activity from neurophysiological signals generated by muscles (1-3). These signals are processed by various algorithms to interpret user intent, enabling control of computer interfaces or devices such as prosthetic limbs.

There are broadly two categories of control algorithms for HMIs based on either discrete categorisation (classification) of, e.g., hand gestures (4, 5) or continuous estimation (regression) of, e.g., muscle force (6). Advanced gesture classification algorithms commonly involve learning features unique to each gesture from training data. However, unravelling EMG signals for all possible hand gestures requires a prohibitive amount of training data and a large number of gesture classes, when applying a direct one-to-one approach. Identifying the contractions of all individual muscles, rather than all conceivable gestures, may result in simpler processing of EMG signals. Such an approach is therefore worth exploring, although it necessitates understanding and more effectively utilizing the underlying anatomical and physiological knowledge of muscles.

A motor unit is a collection of muscle fibres that discharge action potentials in unison along with a motor neuron controlling them. The simultaneous discharge from muscle fibres of the same motor unit generates a compound signal referred to as the motor unit action potential (MUAP). This compound signal amplifies the output of individual motor neurons, providing a direct link to the nervous system and the smallest discrete units of voluntary muscle control. The recorded EMG signal can be seen as a weighted sum of MUAPs, that varies depending on the position of the electrodes and the type of EMG.

EMG can be recorded intramuscularly (iEMG) or from the skin surface (sEMG). While iEMG can provide clear MUAP recordings, and is therefore used clinically to diagnose neurological disorders (7), its invasiveness limits its use in HMIs. Since needle or wire electrodes record only a few spatially local motor units each (7, 8), a comprehensive muscle-controlled interface would require many needles or wires, leading to significant discomfort for users. Non-invasive sEMG is a much more attractive alternative for generalized or widespread HMIs. However, sEMG suffers from reduced interpretability since the recording is less selective compared to iEMG (7, 8). The recording contains an unknown number of active motor units with superimposed MUAPs, making it more difficult to decode into user intent. The signal interpretability of sEMG is further exacerbated by low-pass filtering effects of the tissue which increases both the overlap and homogeneity of MUAP waveforms (7, 9). On the other hand, the simplicity of sEMG recordings have enabled high-density sEMG (HDsEMG), using large grids of electrodes, to become commonplace in research settings (9, 10). High-density electrode grids generate additional spatial information on MUAPs by recording them from many different positions and angles (11). Although this additional spatial information is important, a

large number of EMG channels also complicate the decoding task; HDsEMG contains too much information, which may or may not be relevant for a given task. Thus, effective processing algorithms are essential to simplify the data and extract meaningful features for robust signal interpretation.

Feature extraction techniques for EMG signals are commonly divided into time-domain, frequency-domain, and time-frequency-domain features (12-14). Time-domain features are directly computed from signal amplitudes, such as root mean square (RMS), zero crossings, slope sign changes, or waveform length, which makes them computationally efficient and easy to implement. Frequency-domain features, such as mean or median frequency, and time-frequency-domain features, such as a wavelet transform or short-time Fourier transform, are computationally more complex than time-domain features but have been used to study, e.g., muscle fatigue (15, 16). Common classification approaches for extracted features include linear discriminant analysis (17) and support vector machines (18), which are robust and simple to use compared to more advanced neural network approaches (19). Neural networks are promising due to their ability to capture non-linear relationships, which may be present when multiple muscles contract; however, they are severely limited by slow and complicated training, requiring large amounts of training data. Neural networks also lack in explainability, which is important for understanding why estimation errors occur and can limit analysis and model improvements. Notably, these established approaches do not explicitly incorporate anatomical or physiological knowledge, such as muscle structure, spatial position or motor unit features.

In contrast to the previously mentioned global EMG features, more recent developments in HDsEMG processing have enabled the study of motor unit characteristics (20, 21), using decomposition algorithms often based on independent component analysis (22-26). These algorithms make use of known motor unit physiology, i.e. the statistical sparsity of motor unit discharges, to identify their firing patterns, which can then be used to estimate muscle force (20, 27-29), thus directly decoding user intent from the output of the nervous system. However, current decomposition algorithms identify only a fraction of active motor units, whose total number is unknown (27). Motor unit characteristics therefore lack robustness as features in control algorithms.

We recently proposed a new method which was used to model extensor muscles as ellipsoid volumes from HDsEMG recordings of the forearm during extensions of individual fingers (30). The spatial information of HDsEMG was utilized to localize individual time-domain peaks in the recording. The three-dimensional distributions of localized peaks were then used to generate the shapes of the ellipsoid volumes. In that study, we found that these muscle representations could be used to determine which muscle volume new peaks belonged to and thus identify muscle activity. However, the study was limited to one dataset with 10 participants performing single digit movements. Furthermore, volume modelling and the assessment of new peaks was performed on the same subject and the same session. As such, the generalizability of this modelling approach remains untested. Generalizability can broadly be broken down into multiple categories, depending on the type of training data required to create a model or, e.g., train a neural network. Cross-session generalizability requires that the algorithm works on data

from a new session, with training data from a separate recording; the method needs to adapt to potential variations in electrode placement and data quality. Cross-subject generalizability requires that the algorithm works for completely new subjects not included in the training data; this remains a difficult task with methods typically requiring some amount of individualization or calibration. A final category is generalizability to entirely new gestures not included in the training set, which is rarely explored at all. However, we hypothesize that representative volume modelling of individual muscles in the forearm can generalize to more complex gestures consisting of multiple contracting muscles, removing the need for training data from all conceivable gestures. A control scheme based on this model would be highly intuitive, explainable, and generalizable, and therefore worth exploring.

In this paper, we assess gesture classification using representative volume modelling, focusing on its generalizability across subjects and its ability to recognize entirely new gestures not included in the modelling phase. We apply the method described in (30) to a publicly available HDsEMG dataset (31) to create volume representations of individual digit extensor muscles and generate a three-dimensional average human model of the involved extensor muscles in the forearm. A classification scheme is proposed for single and multi-digit contractions based on localization of time-domain extracted EMG peaks within the model. True and false positive classification rates are analysed in single and multi-label cases to assess the method for generalizability across subjects and completely new gestures.

2. Method

2.1. Dataset

In this study, the publicly available HDsEMG dataset "Hyser" (31) was used. This dataset was chosen for its large coverage of the forearm with monopolar recordings, and the inclusion of single digit gestures. The dataset consists of 256 channels of monopolar HDsEMG, using two adjacent 8-by-8 electrode grids along the anterior side of the forearm as well as the posterior side of the forearm, recording from 20 subjects performing 34 separate gestures. For single digit gestures, only extensions of the thumb and fingers were recorded. Thus, for the purposes of volume modelling of individual muscle regions described in this paper, only the grids on the posterior side were used, primarily covering the extensor digitorum communis (EDC) and extensor pollicis longus (EPL). Additionally, one of the subjects (subject 4) had no recording for one of the single digit gestures and was therefore also excluded. Furthermore, wrist gestures were excluded in order to simplify the model and enable a comparison to our previous study (30). This resulted in a data subset of 128 channels from 19 subjects performing 11 gestures.

Five single-digit gestures including thumb (D1), index finger (D2), middle finger (D3), ring finger (D4), and little finger (D5) extension, were used for modelling muscle volumes and single label classification. Two double-digit gestures (extension of D1-D2, extension of D2-D3), three triple-digit gestures (extension of D1-D2-D3, extension of D2-D3-D4, extension of D3-D4-D5), and one four-digit gesture (extension of D2-D3-D4-D5) were used for multilabel classification assessment; multi-digit gestures were not included in any modelling step and only used for multi-label assessment, to test for generalizability to completely new gestures.

2.2. Average volume modelling

We used a previously developed method (30) to generate representative ellipsoid volumes of forearm extensor muscles by localizing numerous time-domain peaks in HDsEMG data. The three-dimensional distributions of localized peaks, for each action, shaped the ellipsoid for each volume representation. These volumes were then used to classify peaks from a different subject, as well as completely new gestures, summarized in Figure 1.

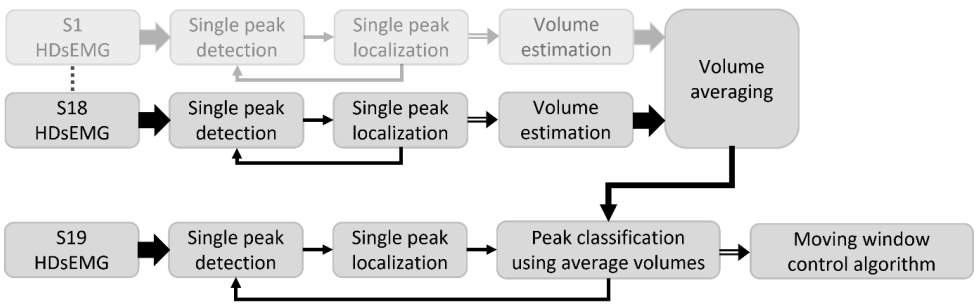

Figure 1. The block diagram illustrates the volume modelling (top row) and the gesture classification (bottom row). For volume modelling, time-domain EMG peaks were first detected and localized individually; the distributions of the localized peaks informed the shapes of representative ellipsoid volumes, which were then averaged across 18 of the 19 subjects. For

gesture classification, localized EMG peaks, from the subject excluded during modelling, were classified using their position in relation to the average volumes. Gestures were then classified with a moving window which accounts for multiple subsequent peaks.

The localization step was first described for estimation of motor unit positions here (32), and later applied to individual EMG peaks for volume estimation here (30). In this method, individual EMG peaks were first identified with peak-detection on a single channel. Centred around each identified peak, a time window of 31 samples (15 samples before and 15 samples after the identified peak) was then extracted across all channels. The spatial surface distribution of the EMG peak was plotted using the row and column position for each electrode (as x and y coordinates) and the energy (calculated as the sum of all squares) within the time window at each channel (as z coordinates). A surface Gaussian function was then fitted to these values, which had parameters for maximum peak amplitude and position (Gaussian function centre), as well as distribution width, length, and rotation. The width and rotation of the Gaussian fit informed an estimate of the depth and fibre direction of the MUAP source. In the original method (30), the Gaussian fit was applied to the peak-to-peak amplitude at each channel, instead of calculating the energy as was done in this work. Compared to using the peak-to-peak values, the signal energy is theoretically less dependent on individual samples, since it is calculated on the full extracted window, and was therefore chosen to improve the stability of position estimates.

In the volume estimation step, five muscle volume representations were estimated, corresponding to the activity during extension of each individual digit, using data from the single digit gestures. For each of the five gestures, the spatial distribution of localized EMG peaks were used to generate the shape of each representative ellipsoid volume; a detailed description of the volume generation can be found here (30). The mean estimated position and fibre direction was first calculated. Then, the standard deviations were calculated along the fibre direction, perpendicular to the fibre direction, and for the depth. The average volumes used for gesture classification, were generated from the average mean and standard deviations across participants for each volume. Since generalizability to completely new individuals was a focus of this work, the averaging was done in a leave-one-out manner, meaning that for each participant a new set of average volumes to be used for classification were calculated from the remaining 18 participants (Figure 2).

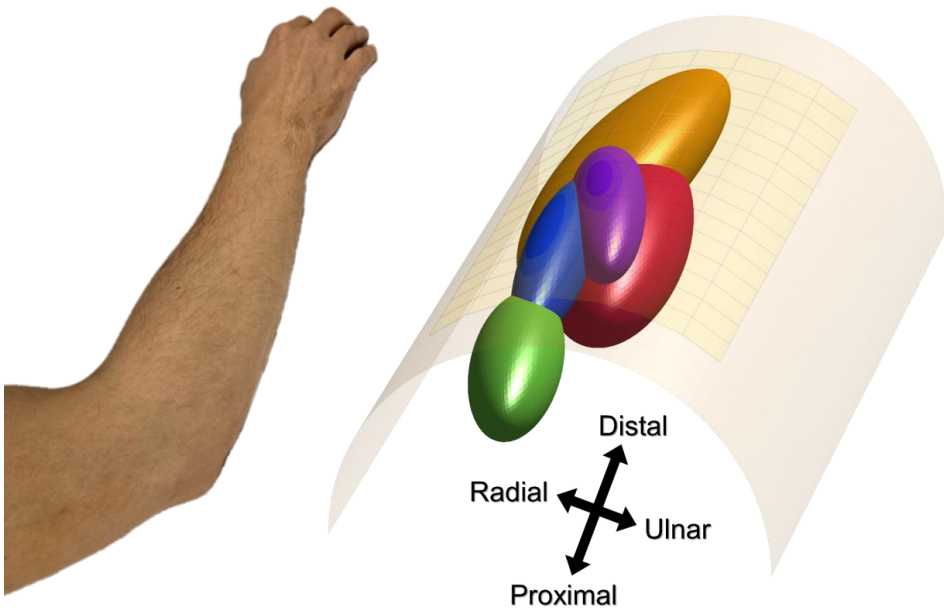

Figure 2. The cylinder model (right) with a set of volume representations, averaged across 18 of the 19 subjects, for extension of the thumb (red), index finger (orange), middle finger (green), ring finger (blue), and little finger (purple). Each volume is defined by an ellipsoid function with the shape determined by the mean spread of localized EMG peaks from the corresponding action. The forearm (left) illustrates the orientation of the model.

2.3. Classification procedure

2.3.1. Ellipsoid based spatial classification

Once the volume models were established, they were used as a reference for classifying new EMG peaks. Ellipsoid based spatial classification was performed in the same manner as in (30). Each volume is represented by an iso-surface, a mathematical function which defines a boundary in three-dimensional space using x, y, and z coordinates (Figure 2). Inserting a specific coordinate into the iso-surface function returns a value which increases with increased distance to the volume centre, modified by the shape of the volume. The estimated position of each EMG peak was inserted into the function representing each volume, returning a set of iso-function values. The EMG peak was classified as belonging to the volume generating the lowest iso-function value. However, different placements of the electrode grids could lead to large offsets between the volumes and the EMG peaks being assessed. Therefore, the volumes were first centred by estimating an offset position which was subtracted for all volumes. The centring offset was calculated from one second of EMG data during ring finger extension. This action was chosen because ring finger extension was found to generate activity in the centre of all volumes with great consistency; the same tendency was also found in (30).

2.3.2. Moving windowing classification

Gesture classification performance was assessed by imitating real-time conditions with a moving window (250 ms window size, 100 ms stride, Figure 3) by segmenting the EMG data. In the single-label classification test, EMG peaks within each window were classified individually, and the class with the most peaks was labelled as active. For the multi-label classification test, EMG peaks within each window were again classified individually, and any class with three or more assigned peaks was labelled active. This threshold number of peaks was selected post-hoc via a grid search of the threshold number and the moving window size, optimizing for the lowest Hamming loss.

Figure 3. The moving window classification procedure is illustrated on the same EMG channel (light blue lines) overlapped with the 250 ms moving window (red line), for three different segments with a 100 ms stride. The horizontal dashed lines represent the five classes. The coloured dots denote the identified peaks on the line of their assigned class. Using single label majority voting, all cases in this example were classified as thumb extension (red). In the multi-label case, with a minimum threshold of 3 peaks, the last window was classified as both thumb (red) and index (orange) extension.

2.4. Evaluation methods

2.4.1. True and false positive rates

For both single label and multi-label gesture classification, performance was evaluated using a table of true positive rates (TPR) and false positive rates (FPR), which refers to the percentage of correctly labelled segments and the percentage of incorrectly labelled segments, for each gesture. In the single label task, each of the five single-digit gestures had one corresponding volume and four non-corresponding volumes, which generated one TPR value and four FPR values per gesture. In the multi-label task, all 11 gestures were included and the number of corresponding volumes changed depending on the gesture. This allowed for a more thorough examination of individual gestures, the distribution of classification errors, and potential limits in the multi-label classification task.

From anatomical knowledge of the forearm, the extensor pollicis longus (EPL) is located beneath the extensor digitorum communis (EDC), extensor digiti minimi (EDM), and extensor indicis proprius (EIP) muscles. Thus, it is expected that the volume representing the EPL would interfere the most with gesture classification performance. To assess this impact on performance, modelling and single label classification was additionally done after excluding thumb extension, generating one TPR value and three FPR values per gesture.

2.4.2. Generic performance metrics

For a wholistic assessment of gesture classification performance, generic metrics were calculated for the multi-label case. The number of true positives, false positives, true negatives, and false negatives, denoted by tp, fp, tn, and fn respectively, were calculated for each label separately and added together, as in (4).

Hamming loss is defined as the ratio of false estimated labels to the total number of labels in the dataset. Thus, a lower Hamming loss corresponds to better performance.

$$Hamming\ loss = \frac{fp + fn}{tp + tn + fp + fn}$$

Precision is defined as the ratio of true positives to the total number of positive estimated labels. This metric is favoured by ‘cautious’ or ‘strict’ classification algorithms, which have a high threshold for generating a positive label, resulting in a minimal number of false positives.

$$Precision = \frac{tp}{tp + fp}$$

Recall (i.e., true positive rate or sensitivity) is defined as the ratio of true positive estimated labels to the total number of ground truth positive labels. Recall is favoured by ‘heedless’ or ‘lenient’ classification algorithms, which have a low threshold for generating a positive label, thus identifying most positive labels while disregarding the number of false positives.

$$Recall = \frac{tp}{tp + fn}$$

Precision and recall tend to be inversely related, in the sense that optimizing for the performance of one is often to the detriment of the other. The F1-score provides a compromise between precision and recall.

$$F_1 score = 2 \cdot \frac{Precision \cdot Recall}{Precision + Recall}$$

3. Results

3.1. Single label gesture classification

3.1.1. True and false positive rates

Single label TPR and FPR for gesture classification with five classes are summarized in Table 1. The values show the cross-subject means and standard deviations after calculating individual performances in a leave-one-out manner, where the assessed individual is not included in the generation of the model. Note that for the single label classification task, the sum of each row is 100%. The TPRs (diagonal grey elements) were highest for ring finger extension with a cross-subject mean of 95.1%, which was expected since one second of this gesture was also used for centring the volume models. The TPRs were the lowest for little finger extension with a cross-subject mean of 61.9%, largely due to misclassification as thumb extension as seen in the bottom row in Table 1, where off-diagonal elements show FPRs for each volume. Similarly, a large degree of misclassification occurs between thumb and index finger extensions, which indicates that the thumb extension interferes the most with classification performance. Table 2 shows the true and false positive rates after removing the thumb extension gesture from the set.

	True and false positive rates (%)				
Action	Vol 1	Vol 2	Vol 3	Vol 4	Vol 5
Thumb	76.9 ± 29.9	21 ± 30.2	0.3 ± 1.1	0 ± 0	1.4 ± 4.2
Index	24.1 ± 34	64.1 ± 39.8	6.1 ± 22.2	5.6 ± 18.1	0.2 ± 0.8
Middle	2 ± 8.6	0 ± 0	80.5 ± 35.1	12.2 ± 28.9	5.3 ± 22.9
Ring	0.9 ± 3.1	1.7 ± 6.6	2.2 ± 4	95.1 ± 12.6	0.2 ± 0.6
Little	20.8 ± 29	12.8 ± 31	1.4 ± 4.4	3 ± 10.7	61.9 ± 39.3

Table 1. Cross-subject mean and standard deviation for true positive rates (diagonal elements) and false positive rates (off-diagonal elements) for 250 ms windowed moving mode.

	True and false positive rates (%)				
Action	~~Vol 1~~	Vol 2	Vol 3	Vol 4	Vol 5
~~Thumb~~	-	-	-	-	-
Index	-	86.2 ± 30.2	6.2 ± 22.1	6.1 ± 20.2	1.4 ± 5.1
Middle	-	0 ± 0	82.4 ± 35.4	12.4 ± 29.4	5.3 ± 22.9
Ring	-	2.2 ± 8.8	2.5 ± 4.6	95 ± 12.4	0.3 ± 1
Little	-	17.6 ± 36.8	1.2 ± 4.2	3.3 ± 10.2	77.9 ± 37.4

Table 2. True positive rates (diagonal elements) and false positive rates (off-diagonal elements) for 250 ms windowed moving mode after excluding thumb extension.

3.2. Multi-label gesture classification

3.2.1. True and false positive rates

Multi-label true and false positive rates for gesture classification with 11 classes are summarized in Table 3. The values show the cross-subject means and standard deviations in a leave-one-out manner, similar to the single label test. In contrast to the single-label test, multiple labels could be positive for each segment, and the sum of each row is no longer 100%. This is exemplified by comparing little finger extension in Table 1 and Table 3, where a substantial increase in both TPR and FPR is seen for the multi-label task.

Note here that assessments of the bottom six multi-digit gestures were performed on participants not included in the modelling step and, more importantly, were completely new gestures; modelling only made use of data from single-digit extensions. Although the TPRs (grey elements) vary greatly, the highest TPR is much greater than the FPR. For each gesture, even the lowest TPR is greater than the highest FPR in most cases, revealing clearly distinct distributions between actions.

	True and false positive rates (%)				
Action	Vol 1	Vol 2	Vol 3	Vol 4	Vol 5
D1	75.5 ± 27.1	29.6 ± 36.1	1.2 ± 3	0 ± 0	6.6 ± 19.5
D2	29.8 ± 34.7	74.8 ± 34.2	10.5 ± 26.8	12 ± 28.8	2.1 ± 7.8
D3	6.7 ± 21.1	1.1 ± 3.8	90.7 ± 25.5	22.2 ± 39.4	5.3 ± 22.9
D4	6.1 ± 13.9	7.4 ± 18.1	16.3 ± 16.1	97.3 ± 7.6	2.4 ± 6.1
D5	38.5 ± 38.1	21.7 ± 35.5	3 ± 8.5	8.1 ± 19.1	77.5 ± 34.5
D1, D2	69.6 ± 30.9	52.8 ± 40	6.7 ± 22.2	1.4 ± 3.8	3.7 ± 13.9
D2, D3	8.4 ± 20.6	19.8 ± 25.9	82.2 ± 29	34.5 ± 37.4	3.7 ± 16.3
D1, D2, D3	33.3 ± 31.4	25.4 ± 28.8	74.8 ± 36	6.6 ± 17.6	2.4 ± 5.2
D2, D3, D4	12.6 ± 25.9	13.9 ± 28.4	73.3 ± 32.3	76.6 ± 29.4	10.4 ± 27.1
D3, D4, D5	18 ± 24.4	19.2 ± 34	51.6 ± 32.2	79.9 ± 28.3	19.7 ± 30.2
D2, D3, D4, D5	19 ± 20.5	26 ± 33	66.7 ± 32.7	77.9 ± 24.8	11 ± 26.2

Table 3. True positive rates (grey elements) and false positive rates (white elements) for 11 gestures in the multi-label gesture classification task, with a moving window of 250 ms and a minimum threshold of 3.

3.3.2. Multi-label performance metrics

The generic performance metrics are summarized in a violin plot (Figure 4). The results show a cross-subject mean Hamming loss of 23.7, Precision of 77.8, Recall of 57.8, and F1-score of 66.0 %; with a standard deviation Hamming loss of 7.0, Precision of 12.9, Recall of 9.3, and F1-score of 9.9 %; a median Hamming loss of 21.4, Precision of 79.1, Recall of 60.1, and F1-score of 68.4 %; with interquartile range Hamming loss of 18.7-25.3, Precision of 72.6-87.7, Recall of 53.1-62.8, and F1-score of 63.1-72.6 %. The better median performance compared to mean performance suggests that the distribution of performances is skewed by low performance outliers. Precision performance is comparatively much higher than recall performance, which indicates that the method is ‘strict’. The lower recall performance indicates

difficulties in correctly identifying all positive labels at the same time, and that a larger window or lower threshold can result in a more balanced performance.

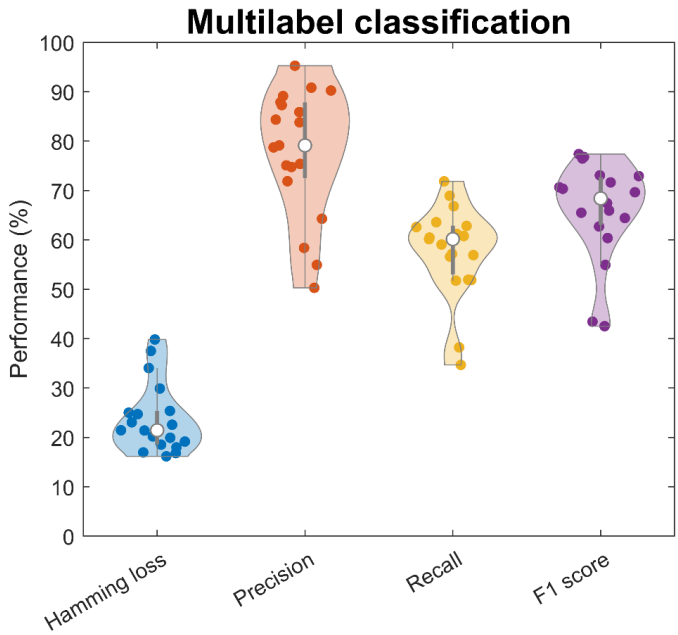

Figure 4. A violin plot showing performance metrics for multi-label gesture classification. Coloured dots represent individual subject performances; white dots indicate the mean. Shaded regions illustrate the approximate data distribution, with visible skew due to a few low-performing outliers.

4. Discussion

This study presents a novel approach to finger gesture classification based on representative muscle volume modelling, emphasizing generalizability. By functional modelling of the active regions in the forearm during extension of individual digits, averaged across multiple subjects, representative volumes were generated for the corresponding muscles. Using these representative volumes, we demonstrated the feasibility of a real-time classification algorithm that generalizes across users and even to new gestures. By leveraging a leave-one-out approach to modelling and testing, the study showed that functional volume representations of muscles generalize across most individuals, which makes this modelling approach suitable for widespread applications. The presented method is an initial step towards the creation of comprehensive three-dimensional models, usable by anyone for gesture classification without additional training or modelling data.

The study also demonstrated a limited degree of generalizability to completely new gestures, as seen in Table 3. Notably, EMG data from multi-digit gestures was never included in the functional modelling of muscle volumes. The multi-digit gestures were instead classified using volumes generated by single-digit gestures from other participants only. Table 3 demonstrates that the EMG data from each multi-digit gesture was predominantly classified as belonging to the volumes corresponding to the active digits (grey elements). The limitation of this generalizability was seen in the overall recall rate, summarized in the violin plot (Figure 4). The limited recall rate suggests that there were difficulties in identifying multiple muscles at once. The moving window classification used in the multi-label test required three or more EMG peaks to be classified to a volume to label it as positive. This may severely limit performance for gestures with many simultaneously active muscles, since each EMG peak was assigned to only one volume. In these cases, a longer time window or lower thresholds might be required when identifying, e.g., four simultaneously active digits. Another explanation for the limited recall performance might be that the shape or structure of the muscles were significantly different when multiple digits contracted simultaneously compared to individual digit contractions.

The method for generating volume representations of muscles (30) was previously only demonstrated on single-digit gestures with inter-session modelling on a dataset tailored to generate optimal volumes using stable isolated isometric contractions. This study further validated the method by successfully applying it to a generic publicly available HDsEMG dataset (31). This indicates that the method is easily applied to other HDsEMG datasets; however, it should be applied to a wider range of datasets to gauge any potential limitations.

Another finding of this study was the amount of overlap in the single-digit test between thumb extension and both index and little finger extension, while thumb extension showed almost no overlap with middle and ring finger extension. This provides further insights into the functional anatomy of the dorsal compartment of the forearm; however, further studies are required to fully explain this discrepancy. It is worth noting that while the EDC is a fused muscle extending all fingers, previous studies (as well as this study) demonstrated a specific segmentation of the EDC where middle finger (EDC-3) extension was mainly generated by EMG activity at the

proximal end of the EDC muscle (30, 33-35). In contrast, the EDC segments responsible for index finger (EDC-2) extension and little finger (EDC-5) extension seem to be located at the distal end. However, it is important to note that extension of the index and little finger are both controlled by two muscles, EDC-2 and EIP; EDC-5 and EDM respectively. It is unclear to what extent this affects the generated volume representations and thus the gesture classification performance; a more comprehensive model could include multiple volumes for these actions. Thus, the results indicate that the EPL is mainly located beneath EDC-2 or EIP, and EDC-5 or EDM, which is also seen in Figure 2. While the volume representing the EPL was deeper than the other volumes, as expected anatomically, the current method may have potentially underestimated the differences in depth, leading to an increased overlap between volumes. In the localization step, increasing the separability of estimated positions along the depth axis is a potential avenue for improvement.

Another limitation of the current method was the lack of a 'rest' or 'other' class. The current method assigned each EMG peak to one of the volumes in the model. Thus, co-contraction from, e.g., wrist muscles could have been falsely classified as one of the digit extensors. A possible solution could be to identify some maximum distance threshold for ellipsoid classification. EMG peaks localized too far away from any of the volumes in the model would then be excluded.

While the focus of this paper was real-time gesture classification, other promising applications exist as well. Most notably, the method can be used to estimate the distribution of EMG activity between muscles, which could be of great value in rehabilitation assessments. For example, during rehabilitation exercises, the distribution of EMG activity could provide a measure for muscle compensation from co-contracting muscles. Feedback on the degree to which intended and unintended muscles are being used could inform therapists and patients of the quality of current exercises. Such quantitative assessment tools are in high demand, since rehabilitation therapists often rely on their own past professional experience to make assessments (36).

5. References

1. Zheng M, Crouch MS, Eggleston MS. Surface electromyography as a natural human–machine interface: a review. IEEE Sensors Journal. 2022;22(10):9198-214.
2. Guo L, Lu Z, Yao L. Human-machine interaction sensing technology based on hand gesture recognition: A review. IEEE Transactions on Human-Machine Systems. 2021;51(4):300-9.
3. Zongxing L, Baizheng H, Yingjie C, Bingxing C, Ligang Y, Haibin H, et al. Human–machine interaction technology for simultaneous gesture recognition and force assessment: A review. IEEE Sensors Journal. 2023;23(22):26981-96.
4. Olsson AE, Sager P, Andersson E, Björkman A, Malešević N, Antfolk C. Extraction of multi-labelled movement information from the raw HD-sEMG image with time-domain depth. Scientific reports. 2019;9(1):7244.
5. Ahsan MR, Ibrahimy MI, Khalifa OO. EMG signal classification for human computer interaction: a review. European Journal of Scientific Research. 2009;33(3):480-501.
6. Olsson AE, Malešević N, Björkman A, Antfolk C. End-to-end estimation of hand-and wrist forces from raw intramuscular emg signals using lstm networks. Frontiers in Neuroscience. 2021;15:777329.
7. Merletti R, Farina D. Analysis of intramuscular electromyogram signals. Philosophical Transactions of the Royal Society A: Mathematical, Physical and Engineering Sciences. 2009;367(1887):357-68.
8. Karacan I, Türker KS. A comparison of electromyography techniques: surface versus intramuscular recording. European Journal of Applied Physiology. 2024:1-17.
9. Merletti R, Muceli S. Tutorial. Surface EMG detection in space and time: Best practices. Journal of Electromyography and Kinesiology. 2019;49:102363.
10. Del Vecchio A, Holobar A, Falla D, Felici F, Enoka R, Farina D. Tutorial: Analysis of motor unit discharge characteristics from high-density surface EMG signals. Journal of Electromyography and Kinesiology. 2020;53:102426.
11. Zwarts MJ, Stegeman DF. Multichannel surface EMG: basic aspects and clinical utility. Muscle & Nerve: Official Journal of the American Association of Electrodiagnostic Medicine. 2003;28(1):1-17.
12. Khan SM, Khan AA, Farooq O. Selection of features and classifiers for EMG-EEG-based upper limb assistive devices—A review. IEEE reviews in biomedical engineering. 2019;13:248-60.
13. Farina D, Merletti R, Enoka RM. The extraction of neural strategies from the surface EMG. Journal of applied physiology. 2004;96(4):1486-95.
14. Inam S, Al Harmain S, Shafique S, Afzal M, Rabail A, Amin F, et al., editors. A brief review of strategies used for EMG signal classification. 2021 international conference on artificial intelligence (ICAI); 2021: IEEE.
15. Venugopal G, Navaneethakrishna M, Ramakrishnan S. Extraction and analysis of multiple time window features associated with muscle fatigue conditions using sEMG signals. Expert Systems with Applications. 2014;41(6):2652-9.
16. Cifrek M, Medved V, Tonković S, Ostojić S. Surface EMG based muscle fatigue evaluation in biomechanics. Clinical Biomechanics. 2009;24(4):327-40.

17. Zhang H, Zhao Y, Yao F, Xu L, Shang P, Li G, editors. An adaptation strategy of using LDA classifier for EMG pattern recognition. 2013 35th annual international conference of the IEEE engineering in medicine and biology society (EMBC); 2013: IEEE.

18. Toledo-Pérez DC, Rodríguez-Reséndiz J, Gómez-Loenzo RA, Jauregui-Correa J. Support vector machine-based EMG signal classification techniques: A review. Applied Sciences. 2019;9(20):4402.

19. Xiong D, Zhang D, Zhao X, Zhao Y. Deep learning for EMG-based human-machine interaction: A review. IEEE/CAA Journal of Automatica Sinica. 2021;8(3):512-33.

20. Zhang X, Zhu G, Chen M, Chen X, Chen X, Zhou P. Muscle Force Estimation Based on Neural Drive Information From Individual Motor Units. IEEE Transactions on Neural Systems and Rehabilitation Engineering. 2020;28(12):3148-57.

21. Farina D, Merletti R, Enoka RM. The Extraction Of Neural Strategies From The Surface Emg: 2004-2024. Journal of Applied Physiology. 2024.

22. Hyvärinen A, Karhunen J, Oja E. Independent Component Analysis: Wiley; 2001.

23. Chen M, Zhou P. A novel framework based on FastICA for high density surface EMG decomposition. IEEE Transactions on Neural Systems and Rehabilitation Engineering. 2015;24(1):117-27.

24. Negro F, Muceli S, Castronovo AM, Holobar A, Farina D. Multi-channel intramuscular and surface EMG decomposition by convolutive blind source separation. Journal of Neural Engineering. 2016;13(2):026027.

25. Holobar A, Zazula D. Multichannel blind source separation using convolution kernel compensation. IEEE Transactions on Signal Processing. 2007;55(9):4487-96.

26. Lundsberg J, Björkman A, Malesevic N, Antfolk C. Compressed spike-triggered averaging in iterative decomposition of surface EMG. Computer Methods and Programs in Biomedicine. 2022:107250.

27. Farina D, Holobar A, Merletti R, Enoka RM. Decoding the neural drive to muscles from the surface electromyogram. Clinical neurophysiology. 2010;121(10):1616-23.

28. Farina D, Jiang N, Rehbaum H, Holobar A, Graimann B, Dietl H, et al. The extraction of neural information from the surface EMG for the control of upper-limb prostheses: emerging avenues and challenges. IEEE Transactions on Neural Systems and Rehabilitation Engineering. 2014;22(4):797-809.

29. Kapelner T, Vujaklija I, Jiang N, Negro F, Aszmann OC, Principe J, et al. Predicting wrist kinematics from motor unit discharge timings for the control of active prostheses. Journal of Neuroengineering and Rehabilitation. 2019;16(1):1-11.

30. Lundsberg J, Björkman A, Malesevic N, Antfolk C. Muscle activity mapping by single peak localization from HDsEMG. Journal of Electromyography and Kinesiology. 2025:102976.

31. Jiang X, Liu X, Fan J, Ye X, Dai C, Clancy EA, et al. Open access dataset, toolbox and benchmark processing results of high-density surface electromyogram recordings. IEEE Transactions on Neural Systems and Rehabilitation Engineering. 2021;29:1035-46.

32. Lundsberg J, Björkman A, Malesevic N, Antfolk C. Inferring position of motor units from high-density surface EMG. Scientific Reports. 2024;14(1):3858.

33. Gallina A, Botter A. Spatial localization of electromyographic amplitude distributions associated to the activation of dorsal forearm muscles. Frontiers in Physiology. 2013;4:67953.

34. Leijnse JN, Campbell-Kyureghyan NH, Spektor D, Quesada PM. Assessment of individual finger muscle activity in the extensor digitorum communis by surface EMG. Journal of Neurophysiology. 2008;100(6):3225-35.

35. Leijnse J, Carter S, Gupta A, McCabe S. Anatomic basis for individuated surface EMG and homogeneous electrostimulation with neuroprostheses of the extensor digitorum communis. Journal of Neurophysiology. 2008;100(1):64-75.

36. Campanini I, Disselhorst-Klug C, Rymer WZ, Merletti R. Surface EMG in clinical assessment and neurorehabilitation: barriers limiting its use. Frontiers in Neurology. 2020;11:556522.